Multiphase flow in porous media: the impact of capillarity and wettability from field-scale to pore-scale

by

Benzhong Zhao

B.ASc., University of Waterloo (2009)
S.M., Massachusetts Institute of Technology (2012)

Submitted to the Department of Civil and Environmental Engineering
in partial fulfillment of the requirements for the degree of

Doctor of Philosophy in Civil and Environmental Engineering

at the

MASSACHUSETTS INSTITUTE OF TECHNOLOGY

February 2017

Signature redacted

Author .....
Department of Civil and Environmental Engineering
January 16, 2017

Signature redacted

Certified by .....
Ruben Juanes
Associate Professor of Civil and Environmental Engineering
Thesis Supervisor

Signature redacted

Accepted by .....
Jesse Kroll
Associate Professor of Civil and Environmental Engineering
Chair, Graduate Program Committee

Multiphase flow in porous media: the impact of capillarity and wettability from field-scale to pore-scale

by

Benzhong Zhao

Submitted to the Department of Civil and Environmental Engineering
on January 16, 2017, in partial fulfillment of the
requirements for the degree of
Doctor of Philosophy in Civil and Environmental Engineering

Abstract

Multiphase flow in the context of this Thesis refers to the simultaneous flow of immiscible fluids. It differs significantly from single-phase flow due to the existence of fluid-fluid interfaces, which are subject to capillary forces. Multiphase flow in porous media is important in many natural and industrial processes, including geologic carbon dioxide (CO_2) sequestration, enhanced oil recovery, and water infiltration into soil. Despite its importance, much of our current description of multiphase flow in porous media is based on semi-empirical extensions of single-phase flow theories, which miss key physical mechanisms that are unique to multiphase systems. One challenging aspect of solving this problem is visualization—flow typically occurs inside opaque media and hence eludes direct observation. Another challenging aspect of multiphase flow in porous media is that it encompasses a wide spectrum of length scales—while capillary force is active at the pore-scale (on the order of microns), it can have a significant impact at the field-scale (on the order of kilometers).

In this Thesis, we employ novel laboratory experiments and mathematical modeling to study multiphase flow in porous media across scales. The field-scale portion of this Thesis focuses on gravity-driven flows in the subsurface, with an emphasis on application to geological CO_2 storage. We find that capillary forces can slow and stop the migration of a CO_2 plume. The meso-scale portion of this Thesis demonstrates the powerful control of wettability on multiphase flow in porous media, which is manifested in the markedly different invasion protocols that emerge when one fluid displaces another in a patterned microfluidic cell. The pore-scale portion of this Thesis focuses on the impact of wettability on fluid-fluid displacement inside a capillary tube. We show that the contact line movement is strongly affected by wettability, even in regimes where viscous forces dominate capillary forces.

Thesis Supervisor: Ruben Juanes
Title: Associate Professor of Civil and Environmental Engineering

Acknowledgments

There are many people who have contributed, knowingly or unknowingly, towards the completion of this thesis. The importance of their support cannot be overstated here. First of all, I would like to take this opportunity to thank my advisor, Professor Ruben Juanes, for his support, advice, the patience he has shown me and, most of all, his friendship. I have learnt a great deal from Ruben's candor and generosity, which helped shape not only my view on academics but on life in general. In addition, I would like to thank my other thesis committee members, Professor Bradford Hager and Professor Charles Harvey, for their time and guidance.

I am indebted to Christopher MacMinn and Michael Szulczewski for their patient explanation of many basic principles and concepts at the beginning of my PhD career. I have especially enjoyed research collaboration with Chris over the years and I hope to continue our collaboration in the future. I am very fortunate to have been a member of the Juanes Research Group, which is a collective of talented undergraduate and graduate students, as well as postdoctoral researchers. I thank the undergraduate students of the group—Di Jin, Catherine Cheng, and Michelle Dutt—for their help in the laboratory. I thank my fellow graduate students of the group for their infectious enthusiasm in science and for the memories we created outside of the office. I am particularly grateful to have shared this special journey with Benjamin Scandella and Xiaojing (Ruby) Fu, who have become my closest friends. I thank the postdoctoral researchers of the group—Luis Cueto-Felgueroso, Juan Hidalgo, Pietro de Anna, Mathias Trojer, Marie Julie Dalbe, and Zhibing Yang—for generously sharing their knowledge and experience.

I started my PhD at the Parsons Laboratory for Environmental Science and Engineering, which is a truly interdisciplinary place that houses researchers from a broad range of backgrounds. Special thanks to my microbiologist cubicle-mates—Allison Perrotta and Katya Frois-Moniz—for their good humor and for sharing with me the fascinating world of bacteria and viruses. I have made many good friends at the Parsons Lab: Kyle Peet, Kelly Daumit, Daniel Prendergast, Noriko Endo, and Kyle

Delwiche. I thank each of you for helping me celebrate the good times and support me through the more challenging times. I must also thank the administrative staff at the Civil and Environmental Engineering Department—Patricia Glidden, Kris Kipp, Kiley Clapper, James Long, and Roberta Pizzinato—for their assistance.

I was very fortunate to have been involved in the MIT Cycling Club and the MIT Triathlon Club in my spare time. The workouts and long rides have always invigorated me to get back to research with a fresh mind. The club members constantly amazed me with their athleticism and, more importantly, their commitment to achieve work-life balance. I will strive to do the same for the rest of my career.

In addition, I must acknowledge the contributions from my friends and extended family outside of MIT. I would like to express my gratitude towards Warren Wyckoff, who rented a minivan and drove me and my belongings from Toronto to Boston a little over 6 years ago so that I could start my studies on time. Special thanks goes to my cousin Yipin (Cheryl) Zhao, who started her undergraduate studies in California in the same year that I started graduate school. She has been my family in the United States over these years. I am grateful to have celebrated many birthdays and holidays with her away from home.

Finally, I would like to thank my parents for their love and support. Although they couldn't always appreciate the highs and lows of life as a graduate student, they have always encouraged me to work towards my goals. I wish to apologize for my continuous absence from home, and express my gratitude towards their annual trip across the Pacific to visit, which has always lifted my spirits over the holidays.

Reflect upon your present blessings, of which every man has plenty; not on your past misfortunes, of which all men have some.

Charles Dickens

Contents

List of Figures

An experiment is a question which science poses to Nature, and a measurement is the recording of Nature's answer.

Max Planck

Chapter 1

Introduction

Multiphase flow in the context of this Thesis refers to the simultaneous flow of immiscible fluids. It differs significantly from single-phase flow due to the existence of fluid-fluid interfaces, which are subject to capillary forces. Multiphase flow in porous media is important in many natural and industrial processes, including geologic carbon dioxide (CO_2) sequestration, enhanced oil recovery, and water infiltration into soil. Despite its importance, much of our current description of multiphase flow in porous media is based on semi-empirical extensions of single-phase flow theories, which miss key physical mechanisms that are unique to multiphase systems. One challenging aspect of solving this problem is visualization—the flow behavior of interest typically occurs inside opaque media and hence elude direct observation. Another challenging aspect of multiphase flow in porous media is that it encompasses a wide spectrum of length scales—while capillary force is active at the pore-scale (on the order of microns), it can have a significant impact at the field-scale (on the order of kilometers). In this Thesis, we employ novel laboratory experiments and mathematical modeling to study multiphase flow in porous media across scales.

The field-scale portion of this Thesis (Chapter 2) focuses on gravity-driven flows in the subsurface, with an emphasis on application to geological CO_2 storage, where supercritical CO_2 is captured from the flue gas of power plants and injected underground into deep geological formations. Geological CO_2 storage is widely regarded as a promising tool for reducing anthropogenic CO_2 emissions into the at-

mosphere [5; 63; 86; 102; 108], which is critical in humanity's effort to combat climate change. Given the large scale of CO_2 storage required to significantly reduce CO_2 emissions, it is critical that we understand the fate of the stored CO_2, so that we can design effective injection and monitoring strategies to minimize leakage risks. After injection, the CO_2 spreads and migrates as a buoyant gravity current relative to the denser, ambient groundwater. Although the CO_2 and the groundwater are immiscible, the impact of capillarity on CO_2 spreading and migration is poorly understood. We show via table-top experiments that capillary pressure hysteresis pins a portion of the fluid-fluid interface. The horizontal extent of the pinned portion of the interface grows over time and this is ultimately responsible for limiting the migration of the current to a finite distance. We develop a mathematical model that captures the evolution of the CO_2 current and predicts the maximum migration distance.

The meso-scale portion of this Thesis (Chapter 3) focuses on the impact of wettability on multiphase flow in porous media. Wettability is a measure of a fluid's affinity to a solid surface in the presence of another fluid. It has been known for decades that wettability can have a strong impact on the flow [15; 28; 61], but the microscale physics and macroscopic consequences remained poorly understood. Here, we study the impact of wettability on viscously unfavorable fluid-fluid displacement in disordered media by means of high-resolution imaging in microfluidic flow cells patterned with vertical posts. By systematically varying the wettability of the flow cell over a wide range of contact angles, we find that increasing the substrates affinity to the invading fluid results in more efficient displacement of the defending fluid up to a critical wetting transition, beyond which the trend is reversed. These results demonstrate the powerful control of wettability on multiphase flow in porous media, and show that they rely on the inherent 3D nature of interfacial flows.

The pore-scale portion of this Thesis (Chapter 4) focuses on the impact of wettability on fluid-fluid displacement inside a capillary tube. Fluid-fluid displacement in capillary tubes is a classical problem in fluid mechanics [16; 45; 109; 118], and it serves as a simple, but important analogue to multiphase flow in porous media. Despite many experimental and modeling studies of this problem, several key phe-

nomena remain poorly understood. Here we study this problem experimentally in capillary tubes of two distinct wetting conditions. We visualize the dynamics of the fluid-fluid interface in high-resolution for both viscously favorable and viscously unfavorable displacement under a wide range of capillary numbers (Ca). In viscously favorable displacement, the interface bends further into the less viscous fluid with increasing Ca under both wetting conditions. While the interface always remains as a spherical cap in viscously favorable displacement, this is only true in viscously unfavorable displacement at small Ca. At large Ca, the invading less-viscous fluid forms a finger that advances along the center of the tube, leaving behind the contact line and a macroscopic film of the more-viscous fluid on the tube wall. We find that both the critical Ca at which film formation occurs and the speed of the contact line is strongly controlled by the wettability of the tube.

The last chapter of this Thesis (Chapter 5) discusses the outstanding questions in multiphase flow in porous media, and how the findings presented in this Thesis can be expanded and further explored in future work.

Chapter 2

Capillary pinning and blunting of immiscible gravity currents in porous media

2.1 Summary

In this Chapter, we study the lifetime of an immiscible gravity current in porous media. Gravity currents in the subsurface have attracted recent interest in the context of geological carbon dioxide (CO_2) storage, where supercritical CO_2 is captured from the flue gas of power plants and injected underground into deep saline aquifers. After injection, the CO_2 will spread and migrate as a buoyant gravity current relative to the denser, ambient brine. Although the CO_2 and the brine are immiscible, the impact of capillarity on CO_2 spreading and migration is poorly understood. We previously studied the early-time evolution of an immiscible gravity current, showing that capillary pressure hysteresis pins a portion of the macroscopic fluid-fluid interface and that this can eventually stop the flow. Here, we examine the full lifetime of such a gravity current. Using table-top experiments in packings of glass beads, we show that the horizontal extent of the pinned region grows with time, and that this is ultimately responsible for limiting the migration of the current to a finite distance. We also find

that capillarity blunts the leading edge of the current, which contributes to further limiting the migration distance. Using experiments in etched micromodels, we show that the thickness of the blunted nose is controlled by the distribution of pore-throat sizes and the strength of capillarity relative to buoyancy. We develop a theoretical model that captures the evolution of immiscible gravity currents and predicts the maximum migration distance. By applying this model to representative aquifers, we show that capillary pinning and blunting can exert an important control on gravity currents in the context of geological CO_2 storage. These results are published in *Water Resources Research* [125] and *Energy Procedia* [126].

2.2 Introduction

Gravity currents refer to the predominantly horizontal gravity-driven flow of two fluids with different densities. Gravity currents are prevalent in nature and they occur in the atmosphere, the ocean, and the subsurface [50]. Gravity currents in porous media have been well studied in the past in the context of miscible fluids [6; 8; 51]. Results from these studies have become important predictors for a wide range of processes such as seawater intrusions into freshwater aquifers [37; 65] and drilling-fluid migration into surrounding reservoirs [32]. More recently, the study of gravity currents in porous media has provided new insights into the storage of carbon dioxide (CO_2) in deep geological reservoirs such as saline aquifers [12; 44; 57; 75; 84]. Because CO_2 is less dense than the ambient brine in those reservoirs, the CO_2 will migrate upward due to buoyancy and spread along the top boundary of the aquifer as a gravity current.

While capillarity is absent in miscible gravity currents, it plays an important role in gravity currents with immiscible fluids. Immiscible gravity currents are relevant in processes such as the migration of dense nonaqueous phase liquid (DNAPL) contamination in groundwater aquifers [34; 53; 90], as well as CO_2 storage in deep saline aquifers [39; 43; 74; 75]. A well-studied effect of capillarity in immiscible gravity currents is residual trapping, where tiny blobs of non-wetting fluid become surrounded by

wetting fluid and become immobilized in the pore-space [43; 57; 58; 74]. In addition to residual trapping, capillary forces create a partially saturated layer between the buoyant fluid and the ambient fluid: the capillary fringe. Continuum-scale models predict that capillary effects result in a thick non-wetting current with a blunt nose [40; 64; 85].

Zhao et al. [128] performed the first laboratory experiments of immiscible gravity-exchange flow of two immiscible fluids in porous media. Focusing on the early-time evolution of the macroscopic interface between the fluids, they observed a phenomenon they coined capillary pinning, where a portion of the macroscopic fluid-fluid interface remains stationary (Fig. 2-1a-b). They identified pore-scale capillary pressure hysteresis between drainage and imbibition as the mechanistic cause of the pinned interface. While Zhao et al. [128] described the early-time evolution of immiscible gravity currents (*i.e.* exchange flow), the late-time behavior of immiscible gravity currents has not been studied experimentally.

Here, we study the entire evolution of immiscible gravity currents via release of a finite volume of buoyant non-wetting fluid into a dense wetting fluid in a vertically confined aquifer. In this case, the imbibition front (the portion of the interface where the wetting fluid is advancing) interacts with the left boundary early and begins to rise (Fig. 2-1c). The upward motion of the imbibition front causes an increasing portion of the drainage front (the portion of the interface where the wetting fluid is retreating) to be pinned. Eventually, the entire drainage front is pinned and the non-wetting current is arrested at a finite distance (Fig. 2-1d). We study this system experimentally using analog fluids in flow cells packed with glass beads, as well as in micromodels etched with small cross-stream posts. In contrast to previous studies on immiscible gravity currents, which incorporate capillarity at the continuum scale through a capillary pressure–saturation curve, our experiments are aimed at understanding the physical mechanisms acting at the pore-scale. We show how pore-scale mechanisms alter the behavior of immiscible gravity currents at the macroscopic scale. We extend the classical model of gravity currents in porous media [44; 51] to include capillary pinning and nose blunting, and demonstrate how both mechanisms limit the spreading of a

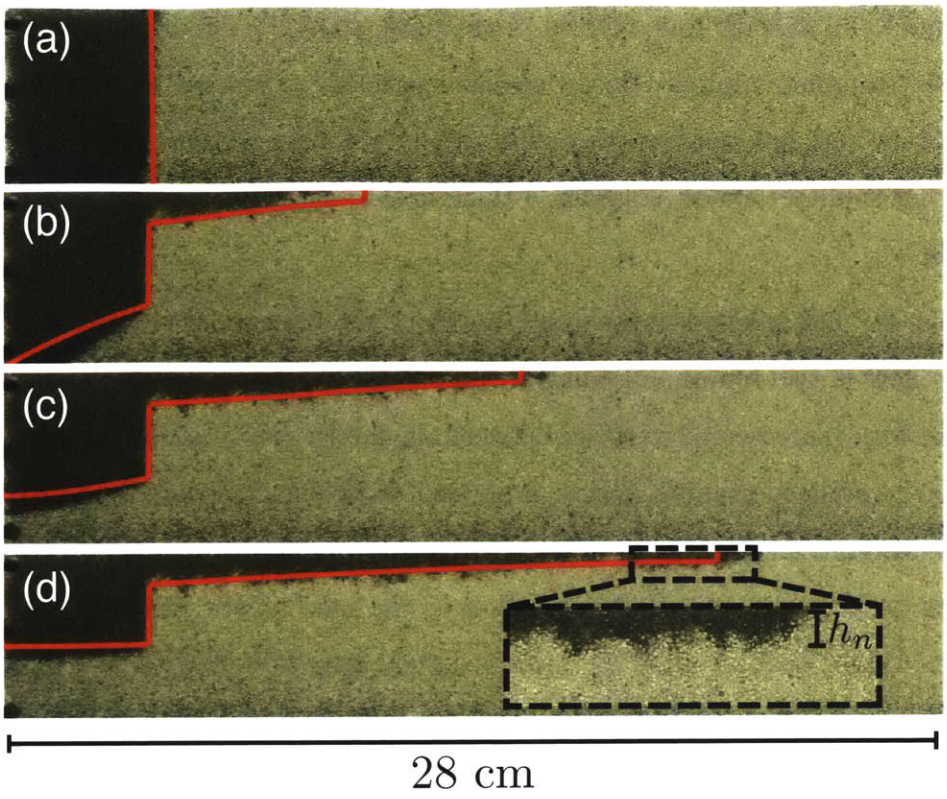

Figure 2-1: Gravity driven flow of a buoyant, nonwetting fluid (air) over a dense, wetting fluid (propylene glycol) in a packing of glass beads. (a-b) Starting with a vertical interface between the fluids, the flow first undergoes a lock-exchange process. (c-d) The process models a finite-release problem after the dense fluid reaches the left boundary. In contrast to the finite release of a miscible current that spreads indefinitely, spreading of an immiscible current stops at a finite distance. Dashed black box highlights the blunt nose of the current, which has thickness h_n (see Section 2.4.2). Red lines represent predictions from our macroscopic sharp-interface model (see Section 2.5).

non-wetting current.

2.3 Laboratory Experiments in Porous Media

In this section we present our observations from laboratory experiments in porous media. In the next section, we connect these macroscopic observations with pore-scale mechanisms. We consider the instantaneous release of a finite volume of buoyant nonwetting fluid into a horizontal aquifer filled with a relatively dense wetting fluid. We conduct these experiments in a rectangular, quasi-two-dimensional flow cell packed

Table 2.1: Properties of the three ambient fluids used in the experiments.

Ambient fluid	ρ [kg/m^3]	μ [Pa $\cdot$ s]	γ [N/m]
Silicone oil	960	0.048	0.020
Propylene-glycol	1040	0.046	0.036
Glycerol-water mixture	1200	0.047	0.065

Table 2.2: Properties of the three bead packs used in the experiments.

Bead size	d [cm]	ϕ [-]	k [cm^2]
$0.08 - 0.12$ cm	0.1	0.407	0.9×10^{-5}
$0.1 - 0.15$ cm	0.125	0.412	1.3×10^{-5}
$0.15 - 0.2$ cm	0.175	0.437	4.5×10^{-5}

with approximately mono-disperse spherical glass beads, following the same procedure described in Zhao et al. [128]. The cell is 5.2 cm tall and 56 cm long, with a thickness of 1 cm. We use air as the buoyant non-wetting fluid, paired with one of three dense wetting fluids (Table 2.1). We report the measured porosity and effective permeability of the bead packs in Table 2.2. We release the same volume of air in every experiment, fixing the width of the initial release, $l = 4.9$ cm (Fig. 2-2).

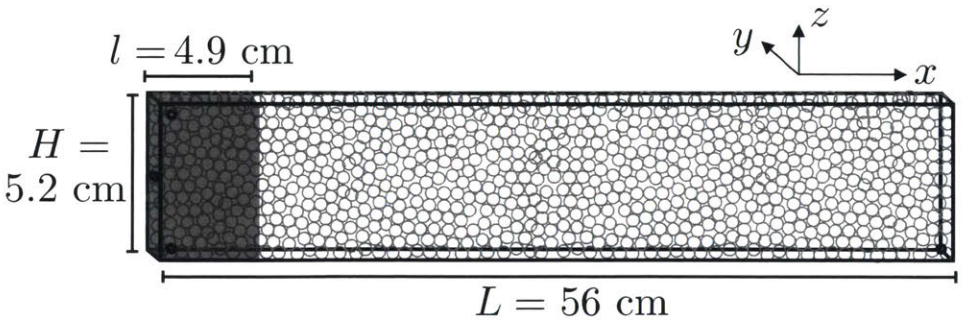

Figure 2-2: Schematic of the laboratory experiments in porous media. We conduct experiments in quasi-two-dimensional flow cells packed with glass beads with an initial release of a rectangular volume of buoyant, non-wetting fluid (gray) into a dense, wetting fluid (white).

2.3.1 Capillary Pinning and De-pinning

Starting from the initial condition of a vertical interface separating the buoyant, non-wetting fluid and the dense, wetting fluid, the two fluids first undergo a gravity-exchange flow. During this early period, we observe that a portion of the initial interface is pinned and does not experience any macroscopic motion (Fig. 2-1a-b). The pinning of the initial interface during the exchange flow was described by Zhao et al. [128]. Here, we study the flow behavior after the end of the exchange flow, at which point the wetting fluid reaches the left boundary of the flow cell and the imbibition front starts to rise (Fig. 2-1c-d). The rise of the imbibition front is accompanied by de-pinning at the bottom of the vertical pinned interface. As the imbibition front rises, an increasing portion of the drainage front is pinned. Eventually, the spreading of the gravity current stops when the entire drainage front is pinned. This is in stark contrast with miscible gravity currents, which spread indefinitely [44; 51].

2.3.2 Nose Blunting

In miscible gravity currents between a buoyant, less viscous fluid and a dense, more viscous fluid, the buoyant fluid spreads out as a thin tongue, with nose thickness on the scale of one grain diameter [72]. In immiscible gravity currents, in contrast, we observe a blunted nose at the front of the buoyant, non-wetting current, as well as a thick current profile (Fig. 2-1d).

2.4 Micromodel Experiments and Pore-scale Mechanisms

In this section, we connect the macroscopic observations from the previous section with their pore-scale origins.

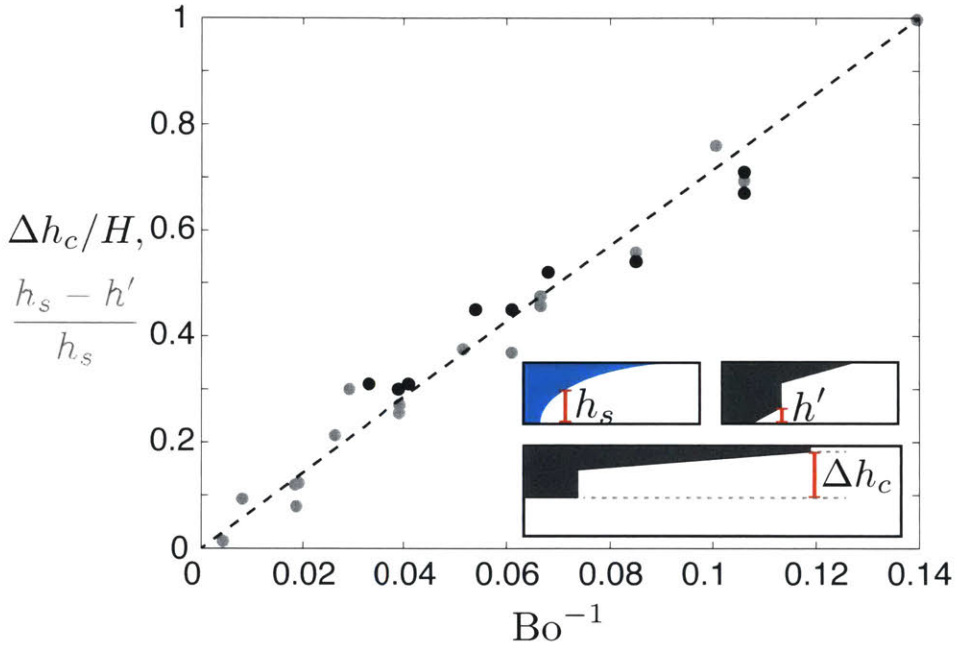

Figure 2-3: Scaling of the pinned interface height and the nose thickness. (a) In contrast to miscible gravity currents, which spread indefinitely, immiscible gravity currents stop at a finite distance. We measure the height difference between the highest point and the lowest point of the nonwetting current, Δh_c, (inset) after the current stops and find that it scales linearly with the strength of capillary relative to gravity, as measured by Bo^{-1}, normalized by the height of the cell H (black circles). The slope of this linear scaling matches that of the capillary height reported in Zhao et al. [128] (gray circles), defined as the normalized difference between the lower hinge height h' and the height of the miscible tilting point, h_s (inset).

2.4.1 Capillary Pinning and De-pinning

Zhao et al. [128] studied the early stage (exchange flow) of immiscible gravity currents in porous media and found that the strength of capillary pinning, as measured by the length of the pinned portion of the interface, is a function of the relative importance between capillarity and gravity, as described by the inverse of the Bond number,

$$\mathrm{Bo}^{-1} = \frac{\gamma/d}{\Delta\rho g H}, \tag{2.1}$$

where γ is the interfacial tension between the fluids, d is the characteristic grain size of the bead pack, $\Delta\rho$ is the density difference between the fluids, g is the gravitational constant, and H is the height of the flow cell (Fig. 2-3a).

To understand the mechanistic cause of the pinned interface, we conduct experiments with air and silicone oil in micromodels made of thin acrylic plates etched with cylindrical posts on a rectangular lattice (Fig. 2-4). The micromodels serve as a porous medium analog in the sense of introducing microstructure, while permitting clear visualization of the flow at the pore level. In particular, the pore-level fluid-fluid interface is a direct indication of the magnitude of capillary pressures locally. The capillary pressure at each pore throat is given by the Laplace pressure $P_c = \gamma\left(R_1^{-1} + R_2^{-1}\right)$, where R_1 is the radius of curvature of the fluid-fluid interface in the plane orthogonal to the axes of the cylindrical posts and R_2 is the radius of curvature of the fluid-fluid interface in the quasi-two-dimensional plane. The transition of the pore-scale radius of curvature along the pinned vertical interface clearly indicate the presence of capillary pressure hysteresis between drainage and imbibition (Fig. 2-4a). Along the vertical pinned interface, the capillary pressure decreases with depth from the drainage capillary pressure P_c^{dr} to the imbibition capillary pressure P_c^{imb}. This decrease in capillary pressure, $\Delta P_c = P_c^{\mathrm{dr}} - P_c^{\mathrm{imb}} > 0$, is offset by the increase in hydrostatic pressure along the vertical, pinned interface. The balance between these two changes in pressure implies that the height of the pinned interface is given by $\Delta h_c = \Delta P_c/\Delta\rho g$. Since P_c^{dr}, $P_c^{\mathrm{imb}} \sim \gamma/d$, $\Delta h_c/H$ scales linearly with $\mathrm{Bo}^{-1} = (\gamma/d)/(\Delta\rho g H)$ (Fig. 2-3a).

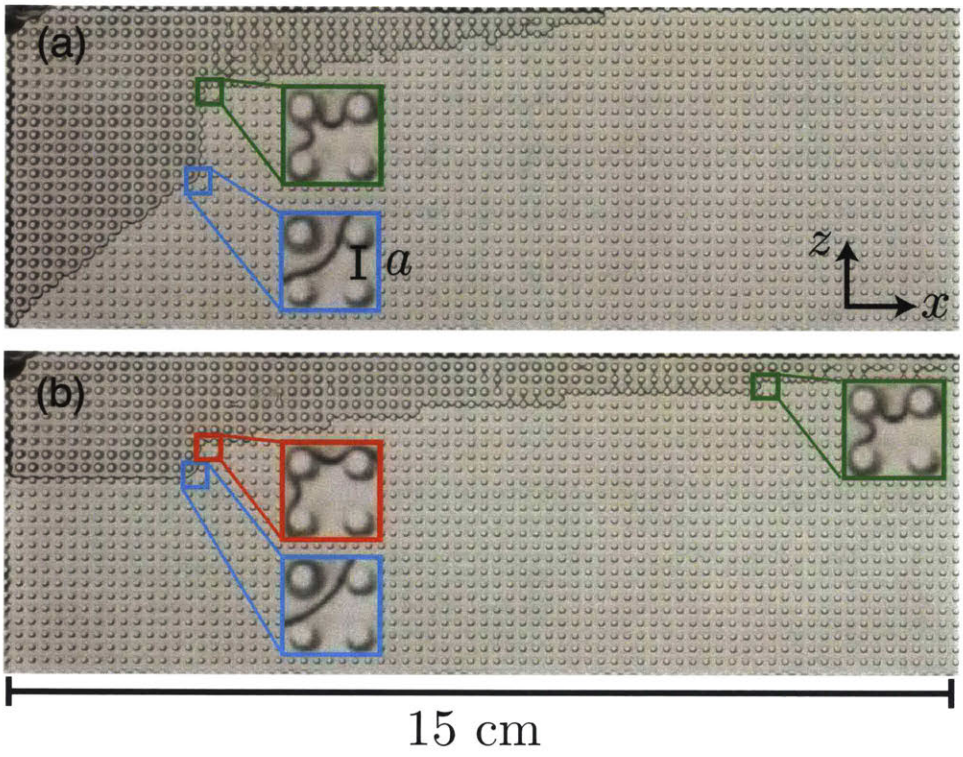

Figure 2-4: Visualization and physical mechanism of capillary pinning. (a) Snapshot of the exchange flow phase of an immiscible gravity current between air and silicone oil in a micromodel with uniform pore throat size ($a = 1$ mm). Capillary pressure hysteresis between drainage (green) and imbibition (blue) is visible via the increase in the radius of curvature of the pore-scale fluid-fluid interface along the vertical interface. The portion of the interface between drainage and imbibition is pinned and does not move during the exchange flow. (b) Snapshot of the finite-release phase of the same gravity current. During the finite-release phase, the imbibition front rises, which leads to a reduced vertical interface. The radius of curvature of the fluid-fluid interface at the top of the vertical interface has increased, indicating that it is now pinned (red). The reduction in the vertical pinned interface is offset by the extension of the pinned interface to the right, pinning increasingly larger portion of the drainage front. The current stops when the entire drainage front is pinned.

After the dense wetting current reaches the left boundary of the flow cell, the bottom of the vertical pinned interface starts to de-pin and becomes part of the imbibition front. This results in a reduced vertically pinned interface. Since the amount of capillary pressure hysteresis in the system remains the same, the hydrostatic pressure increase along the now reduced vertical pinned interface only accounts for part of the entry-pressure difference between drainage and imbibition. At the pore scale, this is reflected by the larger radius of curvature at the top of the vertical pinned interface compared to that at the end of the exchange flow stage (Fig. 2-4b). To balance capillary pressure hysteresis, the pinned interface moves upwards and extends into the drainage front. The de-pinning of the previously pinned interface and the pinning of the previously draining interface are synchronized with each other such that the height difference between the top and the bottom of the pinned interface is always the same, Δh_c. Eventually, the current stops when the entire drainage front becomes pinned.

2.4.2 Nose Blunting

We measure the thickness of the leading edge, or "nose", of the nonwetting current in the porous media experiments, h_n, and find that for a given bead pack, h_n increases with Bo^{-1}. To expand on this observation, we conduct experiments in the micromodel used in Zhao et al. [128]. The micromodel consists of evenly spaced, uniformly sized cylindrical posts such that the pore throat size is the same everywhere. We will refer to this micromodel as the "uniform micromodel". We conduct gravity current experiments under a wide range of Bo^{-1} by tilting the micromodel about the x axis, thus changing the effective strength of gravity in the $y-z$ plane. We do not observe nose blunting in the uniform micromodel even when the effective gravity is low compared to capillarity (*i.e.* large Bo^{-1}) (Fig. 2-5a).

The absence of nose blunting in the uniform micromodel suggests that Bo^{-1} alone is not sufficient to explain nose blunting and that some additional parameter, possibly the pore geometry, is also important. To test this hypothesis, we perform the

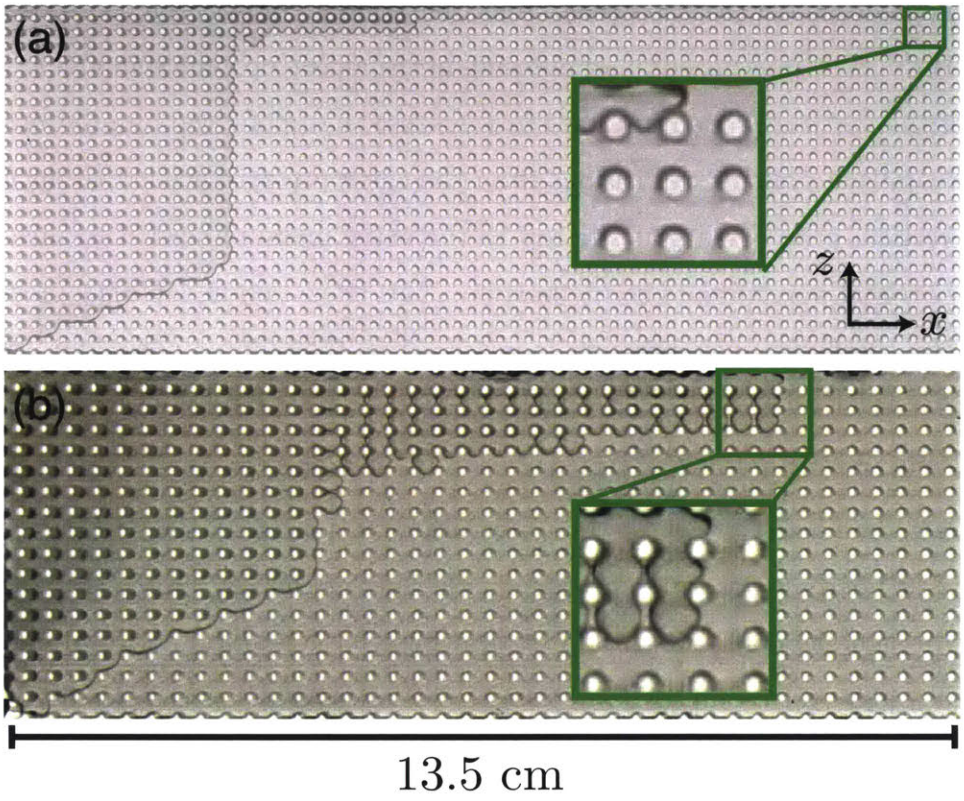

Figure 2-5: Visualization and mechanistic origin of nose blunting. (a) Snapshot of an immiscible gravity current between air and silicone oil in a micromodel with uniform pore throat size ($a = 1$ mm). A significant portion of the initial interface is pinned, indicating strong capillarity with respect to gravity. Yet the nose of the non-wetting current spreads only along the top row of the micromodel. (b) Snapshot of an immiscible gravity current experiment between air and silicone oil in a micromodel with anisotropic pore throat size distribution. The pore throats parallel to the x-axis are 2 mm wide, while the pore throats parallel to the z-axis are 1.5 mm wide. The anisotropic pore throat size distribution creates anisotropy in the capillary entry pressure. Along the nose, the capillary pressure transitions hydrostatically from the larger capillary entry pressure required for air to drain forward, to the smaller capillary entry pressure required for air to drain downward. This is reflected by the change in radius of curvature of the pore-scale fluid-fluid interface along the nose.

same experiments in a micromodel with anisotropic pore throat sizes such that the horizontal pore throats are larger than those in the vertical direction. We will refer to this micromodel as the "anisotropic micromodel". We observe nose blunting in the anisotropic micromodel (Fig. 2-5b) and find that the nose thickness increases with increasing Bo^{-1}. The presence of nose blunting in the anisotropic micromodel is similar to that of the vertical pinned interface in the sense that along the blunted nose, the drainage capillary pressure transitions from the entry pressure needed to invade the smaller, vertical pore throats at the top to the entry pressure needed to invade the larger, horizontal pore throats at the bottom. This transition in capillary pressure is balanced by the hydrostatic pressure increase across the blunted nose, and is visible via the change in the radius of curvature of the pore-scale fluid-fluid interface along the nose (Fig. 2-5b).

To draw the connection with the observations in porous media, we perform experiments in micromodels with disorder in the microstructure (Fig. 2-6). Here, we randomly assign the pore throat radii by drawing from a uniform distribution with a range of $a \in [0.25, 0.75]$ mm. We will refer to this micromodel as the "random micromodel". In this system, even though the pore throat sizes are random and anisotropy is absent, we still observe a blunted nose that thickens with increasing Bo^{-1}. In addition, the disorder in the pore throat sizes leads to a rough drainage front (Fig. 2-6), which is also observed in the porous media experiments.

We now derive a quasi-static, invasion percolation type model [22; 66; 122] to numerically simulate the drainage sequence in the random micromodel. In order for a fluid-fluid interface at a given pore throat to advance to the adjacent pore, the air pressure must be greater than the sum of the local drainage capillary entry pressure and the hydrostatic pressure in the liquid $P_a > P_{c,e}^{\mathrm{dr}} + P_l$. Since the contact angle between silicone oil and air on an acrylic substrate is zero, the drainage capillary entry pressure is $P_{c,e}^{\mathrm{dr}} \approx 2\gamma\left(a^{-1} + d^{-1}\right)$, where a is the width of the throat between neighboring posts and d is the height of the posts [67]. We assume that the air pressure is the same everywhere and that the oil pressure is hydrostatic. At each step, we calculate $P_{c,e}^{\mathrm{dr}} + P_l$ at every fluid-fluid interface and advance the interface

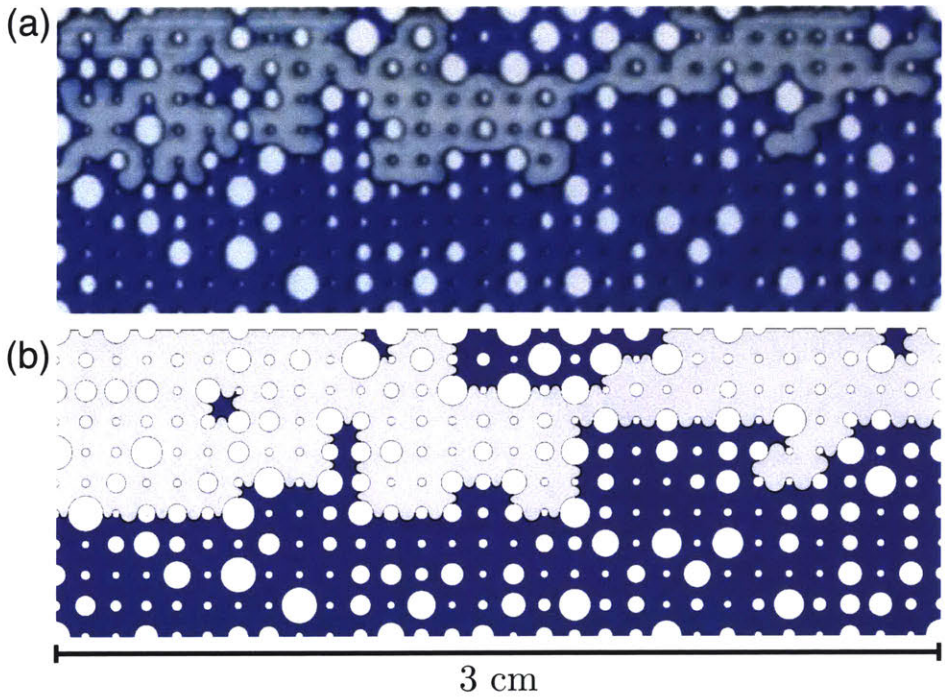

Figure 2-6: Thickness and roughness of the nose of a gravity current. (a) The nose of an immiscible gravity current experiment of air spreading over silicone oil in a thin acrylic cell with round posts etched on a rectangular grid. The pore throat sizes are randomized and follow a uniform distribution within the range of $a \in [0.25, 0.75]$ mm. (b) We simulate the drainage process of the micro-model experiment using the quasi-static model. The quasi-static model is able to accurately capture the drainage process of the gravity current at late times, when viscous effects are negligible ($\mathrm{Ca} = 0.0024$). Here, the differences in capillary pressures at the drainage front is balanced by gravity, resulting in a characteristic thickness of the non-wetting current, even though the interface between the fluids is rough.

with the smallest $P_{c,e}^{\mathrm{dr}} + P_l$ to the neighboring pore.

We find that our simple model is able to accurately capture the drainage sequence in the random micromodel experiments at late times, when viscous effects are small (Fig. 2-6). The relative importance between capillary forces and viscous forces is described by the capillary number Ca= $\mu U/\gamma$, where μ is the viscosity of the dense, more viscous fluid, and we use the rate of nose advancement as the characteristic velocity U. As the viscous effects become small, drainage of the nonwetting phase is completely controlled by capillarity and gravity. This regime is characterized by previous studies as gravity-capillary equilibrium [40; 41; 64; 85; 124; 130]. Since the quasi-static model only takes into account of the local capillary entry pressure and the hydrostatic pressure, its ability to predict the drainage sequence shows that nose blunting is strongly influenced by the spatial distribution of pore throat sizes and hence, different capillary entry pressuresec: forward drainage of the nonwetting fluid is temporarily stalled at narrow pore throats, as downward drainage through wider pore throats becomes more favorable. We find that the anisotropy of the pore space has negligible effects on the imbibition front. This is because the imbibition front advances through cooperative invasion of multiple pores simultaneously, whereas the drainage front relies on subsequent invasion of individual pores [22].

Since nose blunting is caused by the spatial distribution of capillary entry pressures, we can define a characteristic maximum capillary entry pressure $P_{c,e}^{\max}$, and a characteristic minimum capillary entry pressure $P_{c,e}^{\min}$. The difference between the two characteristic capillary entry pressures is balanced by the increase in hydrostatic pressure along the nose of the current and the nose thickness is given by

$$h_n = \frac{P_{c,e}^{\max} - P_{c,e}^{\min}}{\Delta\rho g} + h_o, \tag{2.2}$$

where h_o is some base nose thickness, which is on the order of a single bead. We scale h_n and h_o by the cell height such that $h_n' = h_n/H, h_o' = h_o/H$, and $P_{c,e}^{\max}$ and $P_{c,e}^{\min}$ by the Laplace pressure such that $P_{c,\max}^{\mathrm{dr}'} = P_{c,e}^{\max}/(\gamma d^{-1}), P_{c,\min}^{\mathrm{dr}'} = P_{c,e}^{\min}/(\gamma d^{-1})$. We

obtain

$$h'_n = \frac{\gamma/d}{\Delta\rho g H}(P_{c,\max}^{\mathrm{dr}'} - P_{c,\min}^{\mathrm{dr}'}) + \frac{h_o}{H}. \tag{2.3}$$

The first term on the right hand side of Eq. (2.3) is equal to $\mathrm{Bo}^{-1}\zeta$, where we define $\zeta = P_{c,\max}^{\mathrm{dr}'} - P_{c,\min}^{\mathrm{dr}'}$, which measures the amount of disorder in the pore throat size distribution. A larger value of ζ corresponds to a wider pore throat size distribution, and hence, a more blunted nose for a given Bo^{-1}. For aquifers where $H \gg d$, h_o becomes negligible and the dimensionless nose height h'_n is given by

$$h'_n \approx \mathrm{Bo}^{-1}\zeta. \tag{2.4}$$

2.5 Macroscopic Sharp-Interface Model

We propose a macroscopic model that predicts the evolution, and eventually the stopping of immiscible finite release gravity currents. We base our model on the classical sharp-interface model [44; 51; 124], which assumes hydrostatic pressure distribution everywhere. The classical formulation describing miscible gravity currents [51] is a partial differential equation for the height of the fluid-fluid interface, and is given by

$$\frac{\partial h}{\partial t} - \kappa\frac{\partial}{\partial x}\left[(1-f)h\frac{\partial h}{\partial x}\right] = 0, \tag{2.5}$$

where $h(x,t)$ is the height of the fluid-fluid interface measured from the bottom of the aquifer, $\kappa = \Delta\rho g k/(\mu\phi)$ is the characteristic buoyancy velocity, and $f(h)$ is the so-called fractional flow function and is given by

$$f = \frac{h}{h + \mathcal{M}(H-h)}, \tag{2.6}$$

with $\mathcal{M}$ being the viscosity ratio between the fluids.

The classical formulation can be extended to include capillary effects based on the concept of macroscopic capillarity [40; 41; 85], where one assumes that capillary pressure is a function of the non-wetting phase saturation [70]. To relate fluid satu-

ration to capillary pressure, they use empirical models for capillary pressure curves such as the Brooks-Corey model [17] and the van Genuchten model [114]. They further assume gravity-capillary equilibrium ($\partial P_c/\partial z = \Delta\rho g$) to relate fluid saturation and height of the fluid-fluid interface. The gravity-capillary equilibrium assumption predicts a capillary fringe, or transition zone, where the non-wetting phase saturation varies considerably with respect to depth. The resulting formulation is a vertically-integrated model for the interface height that reduces to the classical sharp-interface model for single phase gravity current in the absence of capillarity. This type of model shows that the existence of a capillary fringe could significantly impact the migration of two-phase gravity currents, and it predicts that capillary effects create a thick current as well as a rounder nose profile [40; 41; 85]. These models, however, assume that capillary pressure is a unique function of the non-wetting phase saturation only, and therefore do not capture the hysteretic nature of capillary pressure. As a result, they do not reproduce interface pinning and finite spreading of two-phase gravity currents.

Capillary pressure hysteresis has been recently incorporated in vertically integrated models of two-phase flow in porous media [30; 128]. Doster et al. [30] study the impact of capillary pressure hysteresis and residual trapping on the constitutive parameter functions of the vertically integrated models. Zhao et al. [128] study two-phase exchange flow in horizontal porous layers. They incorporate capillary pressure hysteresis to the classical sharp-interface model by introducing a capillary term in the flux function that captures capillary pinning. The resulting model reproduces the pinned interface as well as the early-time spreading dynamics. Here, we extend this model to an inclined aquifer and we include blunting at the nose of the current as well as progressive pinning of the drainage front, which is ultimately responsible for stopping the migration of the gravity current.

2.5.1 Mathematical Model

We consider an immiscible gravity current between a buoyant non-wetting fluid with density ρ and a dense wetting fluid with density $\rho+\Delta\rho$ in an inclined porous medium of thickness H and slope θ (Fig. 2-7). We assume that the porous medium is homo-

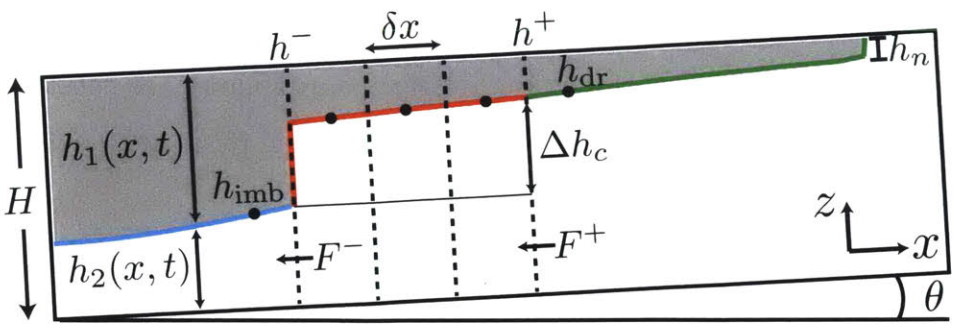

Figure 2-7: Macroscopic sharp interface model for immiscible gravity currents that includes capillary pinning and blunting. After the dense, wetting fluid hits the left boundary, the imbibition front (blue line) starts to move up, causing the active drainage front (green line) to become progressively pinned. As a result, the length of the pinned interface (red line) grows with time, such that the height difference between the imbibition front and drainage front is always Δh_c. The buoyant current stops spreading when the entire drainage front becomes pinned. The model also enforces the leading edge of the buoyant current to fill downwards to the characteristic nose height h_n before advancing forward. We solve the model numerically using a finite volume scheme. This figure illustrates how we incorporate the pinned interface into our numerical scheme as explained in Section 2.9, with solid circles being cell centers and dashed line being cell interfaces.

geneous and isotropic with permeability k and porosity ϕ, and that the boundaries of the flow domain are impermeable. Since we assume that the two fluids are separated by a sharp interface, the thickness of the fluid layers must sum to the thickness of the porous layer everywhere, $h_1 + h_2 = H$. By assuming hydrostatic pressure in both fluids, we can express the pressure distribution in the layer as

$$P = \begin{cases} P_I - \rho g \cos\theta (z - h_2) & \text{for } z > h_2 \\ P_I - P_c + (\rho + \Delta\rho) g \cos\theta (h_2 - z) & \text{for } z \leq h_2 \end{cases} \tag{2.7}$$

where P_I is the unknown pressure at the interface and g is the gravitational acceleration. By definition, the pressure difference across the interface between the non-wetting fluid and the wetting fluid is the capillary pressure P_c.

The volumetric flux per unit width of fluid phase i along the slope is given by Darcy's law $q_i = -k\lambda_i(\partial P/\partial x - \rho_i g \sin\theta)$, where $\lambda_i = k_{ri}/\mu_i$ and ρ_i are the mobility and density of the fluid phase, and k_{ri} is the relative permeability to that phase. Since

we assume the two fluid phases to be completely segregated and the fluid saturation to be homogeneous within each layer, the relative permeabilities are constant. The flow rate is given by the product of the thickness of the fluid phase and its volumetric flux, $Q_i = h_i q_i$,

$$Q_1 = -h_1 k \lambda_1 \left[\frac{\partial P_I}{\partial x} - \rho g \left(\cos\theta \frac{\partial h_1}{\partial x} - \sin\theta \right) \right], \tag{2.8a}$$

$$Q_2 = -h_2 k \lambda_2 \left[\frac{\partial P_I}{\partial x} - \frac{\partial P_c}{\partial x} - (\rho + \Delta\rho) g \left(\cos\theta \frac{\partial h_2}{\partial x} - \sin\theta \right) \right]. \tag{2.8b}$$

We solve for $\partial P_I / \partial x$ by imposing global volume conservation $Q_1 + Q_2 = 0$. We then substitute $\partial P_I / \partial x$ into Eq. (2.8) and, enforcing the identity $h_1 + h_2 \equiv H$, we can express the flow rates in terms of only h_2, which also represents the height of the interface:

$$Q_2 = \frac{\Delta\rho g k}{\mu_2} (1 - f) h_2 \left(\cos\theta \frac{\partial h_2}{\partial x} + \sin\theta - \frac{\partial P_c / \Delta\rho g}{\partial x} \right), \tag{2.9a}$$

$$f = \frac{h_2}{h_2 + \mathcal{M}(H - h_2)}, \tag{2.9b}$$

where f is the fractional flow function and $\mathcal{M} = \lambda_1 / \lambda_2$ is the mobility ratio. To obtain an equation for the evolution of the interface, we consider the conservation of volume of the dense fluid over region Δx and time Δt. The change in volume of the dense fluid is given by

$$\Delta V_2 = \Delta h_2 \Delta x (1 - S_{wc}) \phi = (Q_2|_{x+\Delta x} - Q_2|_x) \Delta t, \tag{2.10}$$

where S_{wc} is the connate water saturation, which accounts for the fact that the non-wetting current does not displace all the wetting fluid on the drainage front. Inserting Eq. (2.9) into Eq. (2.10) and taking limits for small Δx and Δt, we obtain the partial differential equation for the evolution of the interface height $h \equiv h_2$:

$$\frac{\partial h}{\partial t} - \kappa \frac{\partial}{\partial x} \left[\frac{(1 - f)}{(1 - S_{wc})} h \left(\frac{\partial h}{\partial x} + \tan\theta - \frac{\partial h_c}{\partial x} \right) \right] = 0, \tag{2.11}$$

where we define $\kappa = \Delta\rho g \cos\theta k / (\mu_2 \phi)$ as the characteristic buoyancy velocity and $h_c = P_c/(\Delta\rho g \cos\theta)$ as the characteristic height of capillary pressure hysteresis.

It remains to write the capillary pressure, P_c, in terms of the evolution of the interface. Along the imbibition front, we take the capillary pressure to be constant and equal to a characteristic imbibition capillary pressure, P_c^{imb}. Along the drainage front (except for the nose region, which we handle separately), we take the capillary pressure to be constant and equal to a characteristic drainage capillary pressure, P_c^{dr}. Along the pinned interface, which connects the imbibition front to the drainage front, the capillary pressure transitions accordingly from its imbibition value to its drainage value. The transition in capillary pressure is offset by the change in hydrostatic pressure along the pinned interface, with a corresponding difference in interface height of $\Delta h_c = (P_c^{\text{dr}} - P_c^{\text{imb}})/\Delta\rho g \cos\theta$ between the two ends of the pinned interface. We assume a similar transition at the nose, which we define as the region where the current is thinner than the nose height ($H - h < h_n$), and within which the capillary pressure transitions from $P_{c,e}^{\min}$ to $P_{c,e}^{\max}$ with a corresponding change in thickness $h_n - h_0$ (see Section 2.4.2). We then have that $\partial h_c/\partial x = 0$ along the imbibition drainage front and along the drainage front, whereas $\partial h_c/\partial x = \partial h/\partial x$ along the pinned interface and at the nose.

We write the model in dimensionless form by scaling h, Δh_c and x by the characteristic length H and t by the characteristic time $T = H/\kappa$, to obtain a partial differential equation describing the dimensionless interface height with respect to dimensionless time

$$\frac{\partial h}{\partial t} - \frac{\partial}{\partial x}\left[\frac{(1-f)}{(1-S_{wc})} h \left(\frac{\partial h}{\partial x} + \tan\theta - \frac{\partial h_c}{\partial x}\right)\right] = 0, \tag{2.12}$$

where we substitute each variable in Eq. (2.11) with its dimensionless counterpart.

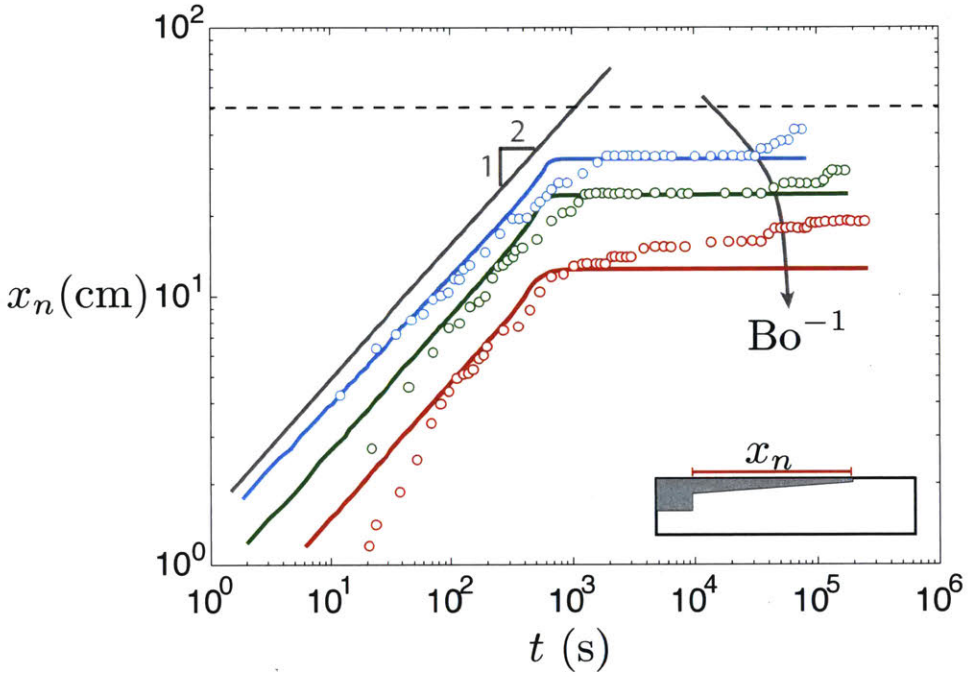

Figure 2-8: Spreading dynamics of immiscible gravity currents in horizontal porous layers. Time evolution of the nose positions of air spreading over silicone oil (blue circles; $\mathrm{Bo}^{-1} = 0.033$), propylene glycol (green circles; $\mathrm{Bo}^{-1} = 0.054$), a glycerol-water mixture (red circles; $\mathrm{Bo}^{-1} = 0.085$) show immiscible gravity currents initially follow the same $x_n \sim t^{\frac{1}{2}}$ scaling as their miscible counterparts. The stopping distance of the buoyant current as well as its rate of advancement decreases with increasing Bo^{-1}. The gray dashed line represents the right boundary of the flow cell. The solid lines represent the simulated nose positions from the sharp-interface model. The apparent long-timescale adjustments of the nose positions after complete pinning of the gravity current are related to throat-widening due to the slow gravity drainage of the wetting films coating the glass beads in the drained region, which effectively decreases the value of Δh_c.

2.6 Spreading Dynamics

Hesse et al. [44] developed early- and late-time similarity solutions for the spreading of a miscible gravity current in a horizontal porous layer. They found that the tip of the buoyant current (the nose position) propagates as $x_n \sim t^{\frac{1}{2}}$ during early times, when the released fluid fills the entire height of the aquifer, and later as $x_n \sim t^{\frac{1}{3}}$, when the height of the released fluid is much smaller than the thickness of the aquifer. They found that the time it takes for the late-time scaling of the nose position to become valid (the transition time) is a function of the mobility ratio $\mathcal{M}$, such that the transition time is longer with higher $\mathcal{M}$.

The nose positions measured from our experiments initially follow the same $x_n \sim t^{\frac{1}{2}}$ scaling as the early-time behavior of their miscible counterpart [44] (Fig. 2-8). The $x_n \sim t^{\frac{1}{3}}$ scaling is absent because of the large mobility ratios in our experiments ($\mathcal{M} \sim 2500$) and the relatively large value of Bo^{-1}, such that current migration is stopped before the transition from early-time scaling ($x_n \sim t^{\frac{1}{2}}$) to late-time scaling ($x_n \sim t^{\frac{1}{3}}$) is reached. Using our macroscopic sharp-interface model, we find that the $x_n \sim t^{\frac{1}{3}}$ spreading regime does exist in immiscible gravity currents, but only for those at small Bo^{-1} and small $\mathcal{M}$, after a sufficiently long time. For immiscible gravity currents at high Bo^{-1}, the initial vertical interface never gets completely de-pinned and, hence, the buoyant current never gets truly thin compared to the height of the aquifer—as a result, it never enters the $x_n \sim t^{\frac{1}{3}}$ spreading regime.

Although capillarity does not change the scaling of the nose positions with respect to time, it does cause a reduction in the rate of propagation of the gravity current: the speed of propagation decreases with higher Bo^{-1} (Fig. 2-8).

The most striking feature in the spreading dynamics of an immiscible gravity current is that the current stops at a finite distance, as opposed to a miscible current, which in the sharp-interface limit continues to spread forever. The mechanistic cause of the finite migration distance is capillary pressure hysteresis: the current stops when the height difference between the imbibition front and the drainage front reaches $\Delta h_c = \Delta P_c / \Delta \rho g$. As a result, the stopping distance x_f is a monotonically decreasing

function of Bo^{-1}. The relationship between x_f and Bo^{-1}, however, is markedly non-linear. At sufficiently low Bo^{-1}, the entire initial vertical interface de-pins and the imbibition front expands laterally outward. This allows the wetting fluid to displace a much larger volume of the non-wetting fluid that would otherwise be "trapped" by the vertical pinned interface at higher Bo^{-1}. As a result, x_f increases significantly at low Bo^{-1} such that it approaches infinity when capillarity is negligible (Fig. 2-9). In addition to Bo^{-1}, x_f is also a function of the pore throat size distribution of the porous medium, as characterized by the "pore-scale disorder" parameter ζ (Section 2.4.2). Higher ζ represents a wider pore throat size distribution, which causes more vertical drainage as the non-wetting fluid spreads outward. The increase in vertical extent of the non-wetting current reduces its lateral extent, leading to a shorter stopping distance (Fig. 2-9).

2.7 Application to Carbon Sequestration

Geologic CO_2 sequestration relies on trapping mechanisms to securely store the injected CO_2. These mechanisms include residual trapping, where tiny blobs of CO_2 are immobilized by capillary forces [54; 58], and solubility trapping, where CO_2 dissolves into the ambient groundwater [54]. Recent studies have shown that convective dissolution, where free phase CO_2 is carried away from the buoyant CO_2 current, can greatly enhance the rate of solubility trapping [71; 96; 119]. As a result, convective dissolution will eventually arrest the migration of the buoyant CO_2 current [39; 72; 73; 75].

We now apply our model to demonstrate the implications of capillary pinning and blunting in the context of geologic CO_2 sequestration. Specifically, we compare the trapping efficiency of capillary pinning and blunting with the combined effect of residual trapping and convective dissolution. MacMinn et al. [75] developed a sharp-interface model for the up-dip migration of a buoyant plume, under the influence of

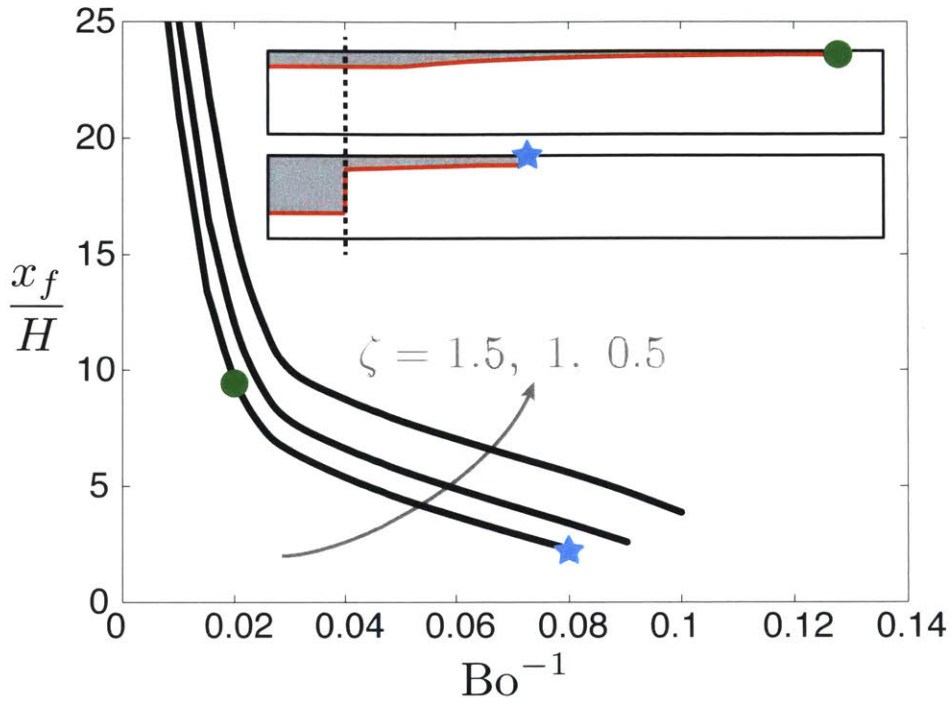

Figure 2-9: Stopping distance of an immiscible gravity current. The stopping distance is controlled by both capillary pinning and nose blunting. While both processes depend on Bo^{-1}, nose blunting is also strongly influenced by the pore geometry. Here, we plot the dimensionless stopping distance x_f/H as a function of Bo^{-1}, of a square-shaped release of non-wetting fluid. The stopping distances are obtained from our macroscopic sharp-interface model, for $\mathcal{M} = 2500$ and three different ζ values. As expected, the stopping distance approaches infinity as capillarity becomes negligible and it tends to zero as capillarity is increased to the limit of complete pinning. The "kink" in the curves above occurs at sufficiently small Bo^{-1} such that the initial vertical interface completely de-pins and the imbibition front is able to expand outward before the current stops. The final state of the current at large and small Bo^{-1} is illustrated in the figure inset. The vertical dashed line in the inset shows the initial width of the non-wetting fluid.

residual trapping and convective dissolution:

$$\widetilde{\mathcal{R}}\frac{\partial \eta}{\partial \tau} + \frac{\partial}{\partial \zeta}\left[N_s(1-f')\eta - (1-f')\eta\frac{\partial \eta}{\partial \zeta}\right] = -\widetilde{\mathcal{R}}N_d, \tag{2.13}$$

where $\eta = h_1/H$, $\zeta = x/l$, $f' = \mathcal{M}\eta/[(\mathcal{M}-1)\eta + 1]$, and $\tau = t/T$. The model is uniquely characterized by four dimensionless parameters:

- $N_s = (l/H)\tan\theta$, which measures the importance of upslope migration;
- $N_d = l^2 q_d/(H^2\phi\kappa\mathcal{M}\cos\theta)$, which measures the importance of convective dissolution. The convective dissolution flux per unit area of fluid-fluid interface is $q_d = \alpha\chi_v\Delta\rho_d g k/\mu_2$, where χ_v measures the maximum equivalent volume of free-phase CO_2 that can dissolve in one unit volume of brine, $\Delta\rho_d$ is the density difference between brine and CO_2-saturated brine, and $\alpha \approx 0.01$ is a constant. The value of N_d is not dependent on permeability k, since κ and q_d are both proportional to k;
- $\widetilde{\mathcal{R}}$ measures the importance of residual trapping. $\widetilde{\mathcal{R}} = 1 - \Gamma$ or 1 locally, depending on whether that portion of the interface is in imbibition or drainage, respectively. The residual trapping number $\Gamma = S_{gr}/(1 - S_{wc})$ is a function of the residual gas saturation S_{gr} and the connate water saturation S_{wc};
- and $\mathcal{M}$, the mobility ratio.

We apply the model with capillary pinning and blunting developed here, as well as the model with residual trapping and convective dissolution developed by MacMinn et al. [75] to four geologic formations associated with actual CO_2 sequestration projects. We set aquifer thickness H, permeability k, residual gas saturation S_{gr}, and connate water saturation S_{wc} to values reported in the literature (Table 2.3). We consider a square-shaped instantaneous release of CO_2 such that $l = H$. For simplicity, we fix the aquifer slope $\theta = 1°$, pore-scale disorder $\zeta = 1$, and the fluid properties of CO_2 and brine to values representative of what could be encountered in deep saline aquifers (Table 2.4). We obtain $\mathcal{M} \approx 13$, $N_s \approx 0.017$, $N_d \approx 7.5 \times 10^{-7}$, while Bo^{-1} and $\widetilde{\mathcal{R}}$ vary based on aquifer-specific properties.

We use the stopping distance of the CO_2 plume, x_f, as a measure to compare the trapping efficiency between the combined effect of capillary pinning and blunting, and the combined effect of residual trapping and convective dissolution (Fig. 2-10). As expected, the effect of capillary pinning and blunting is significant for thin, low-permeability aquifers (*i.e.* high Bo^{-1}), such as the B-sandstone in the Tensleep Formation in the Teapot Dome. Surprisingly, even at thick, high-permeability aquifers (*i.e.* low Bo^{-1}), capillary pinning and blunting could still be more effective in stopping the CO_2 plume than residual trapping and convective dissolution, as is the case for the Tuscaloosa Formation in the United States and the Naylor Field in the CO2CRC Otway Project in Australia. In other cases, however, residual trapping and convective dissolution yield a shorter stopping distance. This is the case for the Mount Simon Sandstone in the United States, which has a high residual trapping number Γ (low $\widetilde{\mathcal{R}}$), in addition to being thick and permeable (low Bo^{-1}).

Szulczewski et al. [108] studied eleven of the largest aquifers in the conterminous United States as an effort to estimate the CO_2 storage capacity in the country. We find $\mathrm{Bo}^{-1} \in [1 \times 10^{-4}, 2 \times 10^{-2}]$ in this group of thick and permeable aquifers. Szulczewski et al. [108] estimated $\Gamma = 0.5$ for all the aquifers they studied because aquifer-specific data on the multiphase-flow characteristics of CO_2 and brine were largely unavailable. Bennion & Bachu [10] conducted a series of relative permeability measurements using CO_2 and brine in sandstone samples from Alberta, Canada under reservoir conditions. We combine the values of S_{gr} and S_{wc} that they reported with the formations that we considered here, and find $\Gamma \in [0.33, 0.5]$. Hence, the majority of large-scale CO_2 sequestration projects will likely involve formations that lie in the upper-left quadrant of Fig. 2-10. Our analysis shows that capillary pinning and blunting could be an important mechanism in limiting the migration distance of the CO_2 gravity current.

We have assumed here that the aquifer is homogeneous, but all natural rocks are heterogeneous at some scale. Further, the variety of complex pore geometries in natural rocks will lead to quantitatively different results—for example, in terms of the scaling constant for the pinned interface height, and the pore-scale disorder parameter. Quantifying these parameters for different rock types is beyond the scope

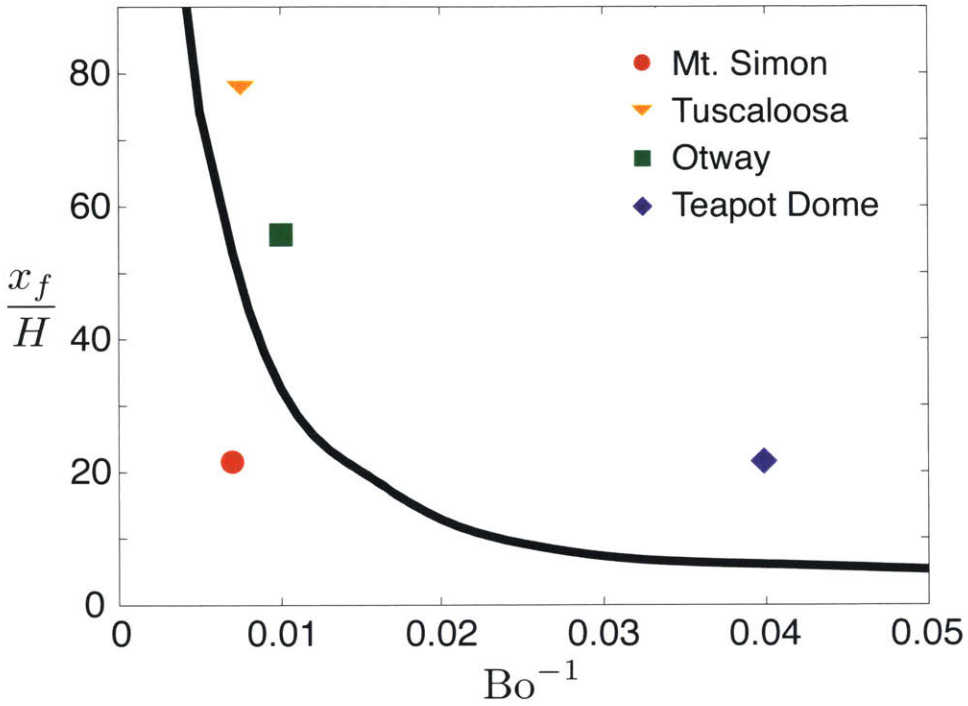

Figure 2-10: Relative importance of capillary pinning and blunting vs. residual trapping and convective dissolution in geological CO_2 sequestration. We consider a square-shaped instantaneous release of CO_2 in a weakly sloped aquifer ($\theta = 1^o$) and use the dimensionless stopping distance x_f/H as the metric of comparison. For capillary pinning and blunting, we use the model developed in this paper to obtain x_f/H as a function of Bo^{-1} (solid black line). The symbols show the dimensionless stopping distance of the CO_2 current under the influence of only residual trapping and convective dissolution, as predicted by the model developed by MacMinn et al. [75], using parameters obtained from aquifers associated with real CO_2 sequestration projects. Our analysis shows that capillary pinning and blunting could be just as effective as residual trapping and convective dissolution in limiting the ultimate migration distance of CO_2.

Table 2.3: Geologic formations associated with actual CO_2 sequestration projects, to which we apply our model.

Aquifer	H [m]	k [m^2]	S_{gr} [−]	S_{wc} [−]	Bo^{-1} [−]	Γ [−]	References
Otway	25	7×10^{-13}	0.33	0.09	9.9×10^{-3}	0.33	**(author?)**
Tuscaloosa	60	2.2×10^{-13}	0.31	0.05	7.4×10^{-3}	0.37	**(author?)**
Mt. Simon	100	1×10^{-13}	0.3	0.4	6.6×10^{-3}	0.5	**(author?)**
Teapot Dome	30	3×10^{-14}	0.3	0.4	4.0×10^{-2}	0.5	**(author?)**

Table 2.4: Fluid properties representative of what could be encountered in deep saline aquifers.

ρ_{CO_2} [kg · m^{-3}]	ρ_{brine} [kg · m^{-3}]	μ_{CO_2} [Pa · s]	μ_{brine} [Pa · s]	$\Delta\rho_d$ [kg · m^{-3}]	χ_v [−]	$\Delta\rho$ [kg · m^{-3}]	$\mathcal{M}$ [−]
700	1000	6×10^{-5}	8×10^{-4}	6	0.05	300	13

of this study, but these considerations are unlikely to have a strong impact on our qualitative findings. It would be useful to include residual trapping, solubility trapping, and capillary pinning and blunting into a single model for CO_2 migration and trapping. We have not done so here because the coupling between these mechanisms is not trivial. Residual trapping occurs along the trailing edge of the plume (i.e. the imbibition front), so we do not expect it to have a strong interaction with capillary pinning at the pinned interface or along the drainage front. Solubility trapping, however, occurs along both the imbibition front and the drainage front, and the way in which it interacts with capillary pinning is unclear.

2.8 Conclusions

We have shown via laboratory-scale experiments that capillary pinning stops the migration of immiscible gravity currents at a finite distance. In addition, capillarity at the drainage front causes the buoyant, nonwetting current to thicken, a phenomenon that we refer to here as "capillary blunting". Using experiments in micromodels designed with pore-throat heterogeneity and anisotropy, we find that capillary pinning

is caused by capillary pressure hysteresis between drainage and imbibition while capillary blunting is caused by the spatial distribution of capillary entry pressures on the drainage front. Both the length of the pinned interface and the thickness of the nose scale with the relative importance between capillarity and gravity, as described by the inverse Bond number, Bo^{-1}. Despite the strong influence of capillarity in immiscible gravity currents, the nose position of the buoyant current with respect to time follows the same scaling as that of miscible gravity currents prior to stopping, although capillarity does slow down the migration of the current.

We have developed a sharp-interface model that captures the effect of capillary pinning and blunting on the evolution of immiscible gravity currents. We apply this model to aquifers associated with actual CO_2 sequestration projects and find that capillary pinning and blunting could be an important mechanism in limiting the maximum extent of CO_2 migration, even in aquifers that are thick and permeable (i.e. low Bo^{-1}). The reduction in maximum migration distance could reduce the risks of CO_2 leakage through fractures or faults present in the aquifer caprock.

2.9 Numerical Implementation

We solve Eq. (2.12) for the interface height h, subject to no-flow boundary conditions at the ends of the flow domain. We approximate the step-like initial configuration of $h = 0$ for $x < 0$ and $h = 1$ for $x > 0$ with the smooth function $h(x) = 1 - [\tanh(\beta x) + 1]/2$, which approaches a unit step for large β. We solve the equation numerically using a centered finite volume method in space with forward Euler time integration [97].

The input parameters for the model are properties of the flow cell (porosity, permeability, and dimensions), the properties of the fluids (densities and viscosities), the connate water saturation S_{wc}, the strength of capillary pressure hysteresis in the system, as quantified by Δh_c, and the characteristic nose height h_n.

We discretize the spatial domain into N cells of size $dx = (x_R - x_L)/N$, denoted with index $i = 1, 2, ..., N-1, N$. x_L and x_R are the x-coordinates of the left and right

boundaries of the flow domain. Integrating Eq. (2.12) over a cell, $[x_{i-\frac{1}{2}}, x_{i+\frac{1}{2}}]$ gives the integral form of the equation for each cell i:

$$\int_{i-\frac{1}{2}}^{i+\frac{1}{2}} \left(\frac{\partial h}{\partial t} - \frac{\partial}{\partial x} \left[\frac{(1-f)}{(1-S_{wc})} h \left(\frac{\partial h}{\partial x} + \tan\theta - \frac{\partial h_c}{\partial x} \right) \right] \right) dx = 0. \tag{2.14}$$

We have a step-like initial condition such that the porous medium to the left of the initial interface is completely filled with the non-wetting fluid, and the connate water saturation in this region is assumed to be always zero (i.e. $S_{wc} = 0, x < 0$). Since we assume P_c to be the minimum drainage capillary pressure $P_{c,\min}^{\mathrm{dr}}$ along the active drainage front where $1 - h \geq h_n$, we get $\partial h_c/\partial x = 0$ for $n_{\mathrm{dr}} < i < n_{\mathrm{nose}}$, where n_{dr} is the cell closest to the pinned interface that is experiencing drainage (i.e. $\frac{dh_i}{dt} < 0$) and n_{nose} is the cell where $1 - h < h_n$. Similarly, since we assume P_c to be the characteristic imbibition capillary pressure on the imbibition front, $\partial h_c/\partial x = 0$ for $i < n_{\mathrm{imb}}$, where n_{imb} is the cell closest to the pinned interface that is experiencing imbibition (i.e. $\frac{dh_i}{dt} > 0$). The interface between n_{dr} and n_{imb} is pinned. On the drainage front and the imbibition front, Eq. (2.14) reduces to

$$\int_{i-\frac{1}{2}}^{i+\frac{1}{2}} \left(\frac{\partial h}{\partial t} - \frac{\partial}{\partial x} \left[\frac{(1-f)}{(1-S_{wc})} h \left(\frac{\partial h}{\partial x} + \tan\theta \right) \right] \right) dx = 0. \tag{2.15}$$

Approximating the gravity-current thickness as piecewise-constant (constant over each cell i), we have

$$\frac{\partial h_i}{\partial t} \delta x + \{F(h)\} \Big|_{i-\frac{1}{2}}^{i+\frac{1}{2}} = 0, \tag{2.16}$$

where $F(h)$ is the flux function evaluated at the inter-cell edges $(i + \frac{1}{2})$ and is given by

$$F(h) = -\frac{(1-f)}{(1-S_{wc})} h \left(\frac{\partial h}{\partial x} + \tan\theta \right). \tag{2.17}$$

We use a two-point flux approximation of Eq. (2.17),

$$F_{i+\frac{1}{2}} \approx \left\{ -\frac{(1-f)}{(1-S_{wc})} h \right\}_{i+\frac{1}{2}} \left(\frac{h_{i+1} - h_i}{\delta x} + \tan\theta \right). \tag{2.18}$$

The term in the curly bracket in Eq. (2.18) plays the role of an effective diffusion coefficient at the interface, $D_{i+\frac{1}{2}}$. To calculate this effective diffusion coefficient at the interface, we take the arithmetic mean of the diffusion coefficients at the adjacent grid blocks

$$D_{i+\frac{1}{2}} \approx \frac{D_i + D_{i+1}}{2}. \tag{2.19}$$

Across the pinned interface, we have

$$F^+ \approx D_{\mathrm{dr}} \left(\frac{h_{\mathrm{dr}} - h^+}{\delta x/2} + \tan\theta \right) \tag{2.20a}$$

$$F^- \approx D_{\mathrm{imb}} \left(\frac{h^- - h_{\mathrm{imb}}}{\delta x/2} + \tan\theta \right), \tag{2.20b}$$

where F^+ and F^- are the fluxes on the drainage side and the imbibition side of the pinned interface, respectively (Fig. 2-7). For simplicity, we use h_{dr} and h_{imb} to approximate the nonlinear diffusion coefficients D_{dr} and D_{imb}. By definition, we have $h^+ - h^- = \Delta h_c$. Since h does not change in time along the pinned interface, F^+ must equal to F^- by volume conservation. We solve for h^- by enforcing $F^+ = F^-$

$$h^- = \frac{D_{\mathrm{imb}} \left(h_{\mathrm{imb}} - \frac{\delta x}{2} \tan\theta \right) + D_{\mathrm{dr}} \left(h_{\mathrm{dr}} - \Delta h_c + \frac{\delta x}{2} \tan\theta \right)}{D_{\mathrm{dr}} + D_{\mathrm{imb}}}, \tag{2.21}$$

and obtain the flux across the pinned interface by substituting h^- into Eq. (2.20).

At the nose of the current where $1 - h < h_n$, we have $F_{\mathrm{nose}} = 0$ as the difference in drainage capillary pressure here is balanced by hydrostatic pressure.

To discretize the equation in time, we employ the forward Euler method, so that

$$h_i^{n+1} = h_i^n + \frac{\delta t}{\delta x} \left[F_{i+\frac{1}{2}} - F_{i-\frac{1}{2}} \right]^n. \tag{2.22}$$

We update n_{dr} and n_{imb} after each time step. For drainage, a portion of the active drainage front becomes pinned when it is no longer draining (i.e. $\frac{dh}{dt} \geq 0$). For imbibition, the imbibition front starts to extend outwards when the entire initial vertical interface is de-pinned.

Chapter 3

Wettability control on multiphase flow in patterned microfluidics

3.1 Summary

In this Chapter, we study the impact of wettability on viscously unfavorable fluid-fluid displacement in porous media. Wettability is a measure of a fluid's affinity to a solid surface in the presence of another fluid. Although it is well known that the wetting properties of porous media can vary drastically depending on the type of media and pore fluids, the effect of wettability on multiphase flow continues to challenge our microscopic and macroscopic descriptions. Here, we investigate this problem experimentally by means of high-resolution imaging in microfluidic flow cells patterned with vertical posts. By systematically varying the wettability of the flow cell over a wide range of contact angles, we find that increasing the substrate's affinity to the injected fluid results in more efficient displacement of the defending fluid up to a critical wetting transition, beyond which the trend is reversed. We identify the pore-scale mechanisms—cooperative pore filling (increasing displacement efficiency) and corner flow (decreasing displacement efficiency)—responsible for this macroscale behavior, and show that they rely on the inherent 3D nature of interfacial flows, even in quasi-2D media. Our results demonstrate the powerful control of wettability on multiphase flow in porous media, and show that the markedly different invasion protocols that

emerge—from pore-filling to post-bridging—are determined by physical mechanisms that are missing from current pore-scale and continuum-scale descriptions. These results are published in the *Proceedings of the National Academy of Sciences of the United States of America* [127].

3.2 Introduction

Multiphase flow in porous media is important in many natural and industrial processes, including geologic CO_2 sequestration [108], enhanced oil recovery [87], water infiltration into soil [25], and transport in polymer electrolyte fuel cells [123]. Much of the research on multiphase flow in porous media has focused on the effect of fluid properties and flow conditions. Much less emphasis has been given to the fluids' affinity to the porous media (*i.e.*, wettability), even though wettability has a profound influence on fluid-fluid interactions in the presence of a solid surface [15; 27; 61]. Despite recent advances in our ability to accurately measure wettability under reservoir conditions [3; 52], and to engineer wettability in the subsurface [19; 82; 104; 105], the complex physics of wetting continues to challenge our microscopic and macroscopic descriptions [88].

Fluid-fluid displacement in the presence of a solid surface can be characterized as either drainage or imbibition, depending on the system's wettability. Drainage refers to the regime where the invading fluid is less wetting to the solid surface than the defending fluid. Imbibition refers to the opposite case, where the invading fluid is more wetting to the solid surface than the defending fluid. Drainage flow in porous media has been studied extensively through laboratory experiments and computer simulations [18; 66; 76; 89], and we now have a fairly good understanding of the different displacement patterns, which include compact displacement, capillary fingering, and viscous fingering. The key dimensionless parameters that control these displacement patterns are the viscosity ratio $\mathcal{M}$ (the ratio of the viscosity of the defending fluid to that of the invading fluid) and the capillary number Ca (a measure of the strength of viscous forces relative to capillary forces).

In contrast with the wealth of observations in the drainage regime, imbibition (especially for viscously-unstable displacement) remains relatively unexplored, even though early experiments have shown significant differences between drainage and imbibition [107]. Specifically, the morphology of the displacement pattern broadens as the invading fluid becomes more wetting to the medium. This observation was confirmed by recent experiments [59; 110] and pore-scale simulations [47; 48], which found that increasing the invading fluid's affinity to the medium makes the invasion pattern more compact at all Ca. However, the complete range of wetting conditions in imbibition is yet to be fully explored, especially in the regime where the invading fluid is strongly wetting to the porous medium.

Here, we use patterned microfluidic flow cells to study viscously unfavorable fluid-fluid displacement (*i.e.*, $\mathcal{M} > 1$) in porous media under an unprecedentedly wide range of wettability conditions. We image the system at high-resolution, providing simultaneous visualization of both the physics of wetting at the pore scale and the impact of wetting on the macroscopic displacement pattern. We find that wettability has a non-monotonic effect on two-phase flow in porous media: increasing the invading fluid's affinity to the medium results in more efficient displacement of the defending fluid until a critical wetting transition, after which the displacement becomes significantly less efficient. We show that this dramatic transition is caused by corner flow, which allows the invading fluid to propagate without filling the pore bodies. We further show that the pore-scale displacement becomes incomplete at large Ca due to the formation of wetting films on the solid surfaces, which can be either the viscous defending fluid or the less viscous invading fluid depending on the wettability condition. Our results demonstrate the complex nature of wettability control on multiphase flow in porous media, which involves key physical mechanisms that are likely to play an important role in natural porous media such as rocks and soils.

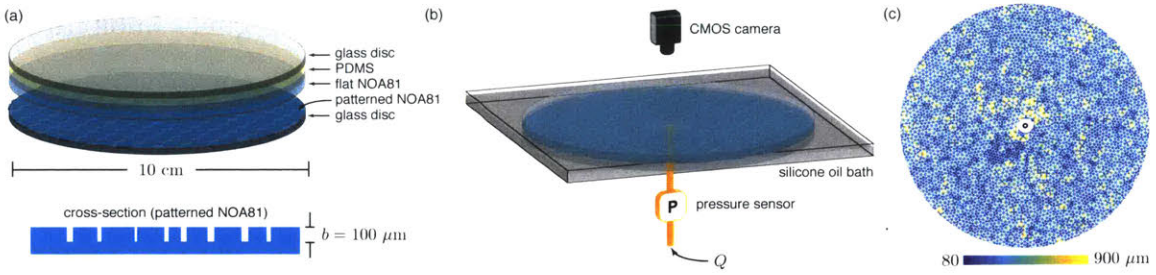

Figure 3-1: We conduct radial fluid-fluid displacement experiments by injecting water into viscous silicone oil in quasi-2D microfluidic flow cells patterned with vertical posts. (a) The core of the flow cell is made of a photo-curable polymer (NOA81) patterned with circular posts of height b =100 μm. The flow cell has porosity $\phi = 0.45$, pore volume $V = 0.38$ mL, and intrinsic permeability $k \approx 2.4 \times 10^{-10}$ m^2. (b) The flow cell is initially saturated with a viscous silicone oil ($\mu_{\text{oil}} = 340$ mPa·s) and placed in a bath of the same fluid to avoid capillary edge effects. We inject water into the center of the flow cell at a constant rate Q. A pressure sensor records the injection pressure throughout the experiment. We image the experiment from above with a CMOS camera, measuring the gap-averaged water saturation at high spatial and temporal resolution from calibrated light intensity. (c) We design the pattern of posts to introduce disorder, but such that it is macroscopically homogeneous at the scale of the flow cell. Here, we show the spatial distribution of pore-throat sizes, which range from 80 to 900 μm.

3.3 Experiments in patterned microfluidics

We conduct fluid-fluid displacement experiments in quasi-2D microfluidic flow cells patterned with vertical posts (Fig. 3-1). This system allows for clear visualization of flow in a porous medium with a known and controllable microstructure, eliminating the uncertainty of natural media and enabling reproducibility [67; 91; 128]. We fabricate the flow cells with a photo-curable polymer (NOA81, Norland Optical Adhesives) via soft imprint lithography. To make the NOA81 surface more hydrophilic, we expose it to high-energy UV radiation—it becomes increasingly hydrophilic with longer exposure time [68; 69]. To make the NOA81 surface more hydrophobic, we apply chemical vapor deposition (CVD) of trimethoxysilane in an enclosed chamber [110]. These techniques allow us to access a wide range of wettability conditions, which we characterize using the static advancing contact angle of water immersed in silicone oil. Specifically, we achieve stable contact angles of $\theta = 150°$ (strong drainage), $\theta = 120°$ (weak drainage), $\theta = 90°$ (neutral), $\theta = 60°$ (weak imbibition), and $\theta = 7°$ (strong

imbibition); see Fig. 3-12. We fabricate a new flow cell for each experiment to ensure precise control over its wettability.

To perform an experiment, we first fully saturate the flow cell with silicone oil ($\mu_{\text{oil}} = 340$ mPa·s). We then inject deionized water ($\mu_{\text{water}} = 0.99$ mPa·s) into the center of the flow cell at a constant rate Q, forcing radially outward displacement of the defending silicone oil. This is a viscously unfavorable displacement, with viscosity ratio $\mathcal{M} = \mu_{\text{oil}}/\mu_{\text{water}} \approx 340$. We characterize the importance of viscous forces relative to capillary forces using the classical macroscopic capillary number $\text{Ca} = \mu_{\text{oil}} \text{v}_{\text{inj}}/\gamma$ [66], where $\gamma = 13 \pm 2$ mN/m is the interfacial tension between the fluids and $\text{v}_{\text{inj}} = Q/(bd)$ is the characteristic injection velocity as constrained by the gap thickness b and the median pore-throat size d. By varying the injection rate ($Q = 0.002$, 0.02 and 0.2 mL/min), we conduct experiments at three capillary numbers spanning two orders of magnitude ($\text{Ca} = 2.9 \times 10^{-3}$, 2.9×10^{-2}, and 2.9×10^{-1}, respectively) for each of the five wettability conditions described above. We provide a detailed description of the flow-cell fabrication process and the experimental procedure in Fig. 3-11.

3.4 Results and Discussion

Our main result is an experimental phase diagram of the displacement patterns obtained under a wide range of wettability conditions and capillary numbers (Fig. 3-2). The phase diagram is a striking qualitative demonstration of the remarkable control wettability exerts on multiphase flow in porous media. To provide quantitative insight into these patterns, we calculate three metrics for each experiment: (1) We quantify the patterns in 2D by calculating their fractal dimension D_f via the box-counting method (Fig. 3-3 and 3-4a); this is a classical measure of the degree to which a pattern fills space in 2D. (2) We quantify the displacement in 3D using the gap-averaged water saturation S measured via light-intensity calibration (Fig. 3-4b and Fig. 3-13). (3) We also introduce an additional 3D metric, the displacement efficiency E_d, which is the fraction of the defending fluid that has been displaced from the flow cell at the

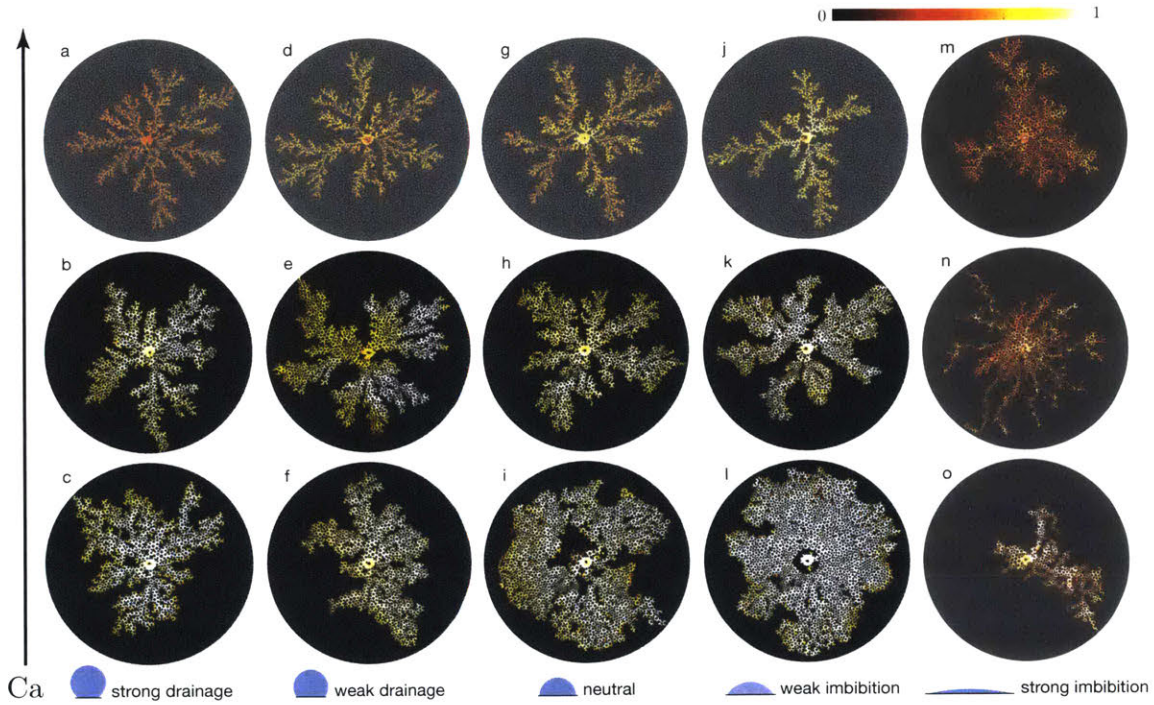

Figure 3-2: Displacement patterns for different wettability conditions (left to right: $\theta = 150°$, $120°$, $90°$, $60°$, $7°$) and capillary numbers (bottom to top: Ca = 2.9×10^{-3}, 2.9×10^{-2}, 2.9×10^{-1}). These patterns correspond to the end of the experiment, which is when the invading fluid reaches the perimeter of the flow cell. The colormap shows the gap-averaged saturation of the invading water. The pattern of circular posts is overlaid on the experimental images and all images are oriented in the same way to aid visual comparison. Generally, the displacement becomes more efficient as the flow cell becomes more hydrophilic (*i.e.*, decreasing θ), or as Ca decreases. These trends do not hold for strong imbibition (m–o), which has a very low displacement efficiency for all Ca.

end of the experiment (Fig. 3-4c).

Certain regions of the phase diagram correspond to flow regimes that have been well studied. In strong drainage, for example, we see the classical transition from capillary fingering ($D_f \approx 1.82$) to viscous fingering ($D_f \approx 1.62$) as Ca increases (Fig. 3-2c–a and Fig. 3-4a) [18; 66; 76; 89].

Although the 2D morphology of these classical patterns is well known, our results provide new insight into the displacement in 3D. We uncover and analyze a wide range of other behaviors for conditions that were previously unexplored.

3.4.1 Incomplete Pore-scale Displacement

The saturation profile of the experimental phase diagram clearly reveals incomplete pore-scale displacement for all wettability conditions as Ca increases (Fig. 3-2). That is, the saturation of the invading fluid decreases as an increasing fraction of the defending fluid is left behind (Fig. 3-4b).

Incomplete displacement and rate dependence in fluid-fluid displacement was first studied in the context of drainage in capillary tubes [16; 109]. In the classical experiments of Taylor [109], air is injected into a cylindrical tube that is initially filled with a wetting, viscous fluid. At small Ca, the air advances via contact-line motion and the displacement is complete. At large Ca, however, viscous forces dominate capillarity and the invading air forms a single finger that advances along the center of the tube, leaving a macroscopic trailing film of the defending fluid on the tube walls. We observe similar behavior in our experiments for all wettability conditions except strong imbibition: The invading water fully saturates the cell gap at small Ca ($S \approx 1$), but a trailing film of defending oil is left on the walls at large Ca ($S \approx 0.6$).

In strong imbibition, the water saturation at large Ca ($S \approx 0.3$) is significantly lower than the saturations measured at other wettability conditions at the same Ca (Fig. 3-4b). In addition, the interface between the invading water and the defending oil becomes diffuse rather than sharp (Fig. 3-2m). These observations are consistent with the formation of thin leading films of water, as recently observed in forced imbibition experiments in Hele-Shaw cells [69]. Mechanistically, the dynamic contact

angle of the meniscus between a low-viscosity wetting fluid displacing a viscous non-wetting fluid decreases with increasing Ca, approaching zero at a critical capillary number Ca^*. For $Ca > Ca^*$, this then enables displacement via thin leading films of wetting fluid that propagate along the solid surfaces, leaving residual nonwetting defending fluid in the pore bodies. In our experiments, Ca^* lies in the transition between $Ca = 2.9 \times 10^{-2}$ and $Ca = 2.9 \times 10^{-1}$.

3.4.2 Compact Displacement via Cooperative Pore Filling

Increasing the invading fluid's affinity to the medium (*i.e.*, decreasing θ; left to right in Fig. 3-2) leads to an increasingly compact displacement pattern in the transition from strong drainage to weak imbibition. Quantitatively, D_f and E_d increase with decreasing θ in the transition from strong drainage to weak imbibition for all Ca. This effect is most striking in weak imbibition at low Ca (Fig. 3-2l), where the injected water sweeps the medium uniformly and forms a remarkably compact displacement pattern ($D_f = 1.92$; $E_d = 0.68$).

The mechanistic origin of the wettability-mediated broadening of displacement patterns was first studied using quasi-static, pore-scale simulations [21; 22; 79]. The simulation results suggested that this is due to cooperative pore filling, in which two or more neighboring menisci overlap and merge into a new, stable meniscus [21; 22; 79]. Here, we provide direct experimental observations of these events (Fig. 3-7a).

Cooperative pore filling is thought to become important below a critical contact angle θ_c [21; 22]. Above θ_c, the invading fluid advances pore-by-pore and the macroscopic displacement pattern is nearly θ-independent. Below θ_c, the displacement becomes increasingly compact due to cooperative pore filling as θ decreases. Cieplak & Robbins [21; 22] found that θ_c itself decreases with porosity, and that cooperative pore filling is promoted by narrower pore throats. In our experiments, θ_c lies in the transition between strong drainage and weak drainage ($120° < \theta_c < 150°$).

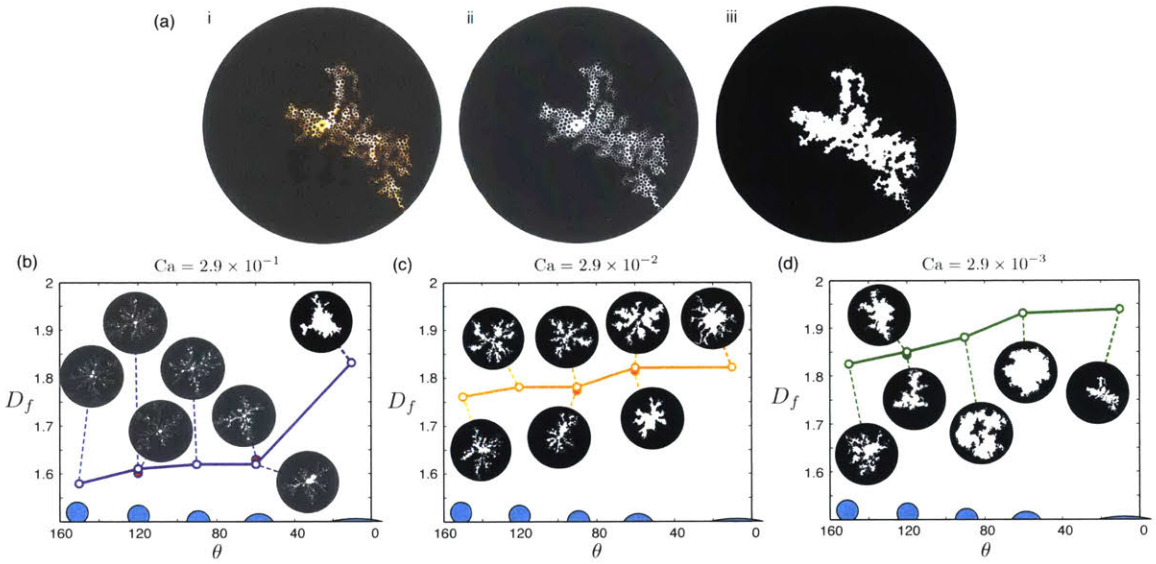

Figure 3-3: We quantify the invasion patterns in 2D by calculating their fractal dimension D_f via the box-counting method. (a) Example workflow for calculating D_f: (i) we first convert the final image of the experiment from intensity to gap-averaged water saturation via the calibration curve; (ii) we then create a binary image of invaded (white) and un-invaded (black) regions by applying a global saturation threshold ($S_{\text{thresh}} \approx 0.01$); (iii) we "fill in" any posts that are completely surrounded by the invading fluid, including these as part of the invaded region. We leave unaltered any regions containing trapped defending fluid. Finally, we calculate D_f for the invaded region via the box-counting method. (b–d) Fractal dimension measurements for the invasion patterns as a function of the static contact angle, with illustrations of the corresponding invaded regions (insets). We find $D_f = 1.58$ for viscous fingering and $D_f = 1.82$ for capillary fingering in strong draiange ($\theta = 150°$), which agree well with values reported in previous studies [refs. 16–18].

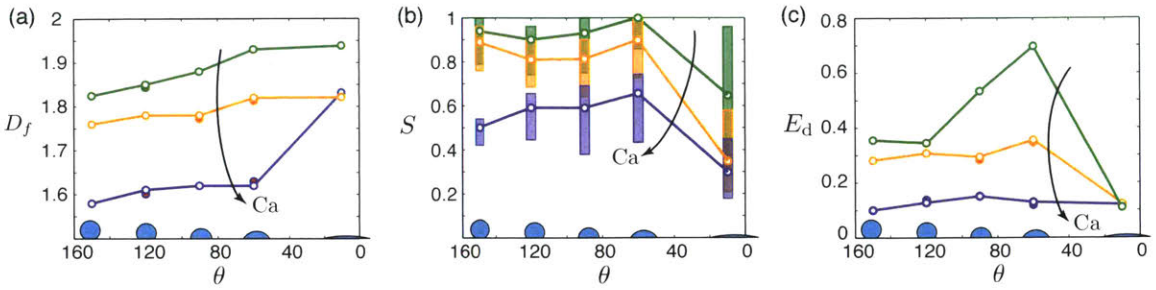

Figure 3-4: (a) Fractal dimension D_f of the 2D invasion pattern as a function of the static contact angle θ, computed using the box-counting method. The open circles correspond to the snapshots presented in the phase diagram (Fig. 3-2) and the filled circles represent additional experiments conducted at the same conditions (see Fig. 3-3). (b) Box plots of the gap-averaged water saturation S of the invaded regions as a function of θ. The open circles correspond to the median S, and the lower and upper edges of each box represent the first and third quartiles of S, respectively. (c) Displacement efficiency E_d as a function of θ, where E_d is defined as the fraction of the defending fluid that has been displaced from the flow cell at the end of the experiment.

3.4.3 Wetting Transition and Corner Flow in Strong Imbibition

Intuitively, one would expect the invasion front to become increasingly compact with decreasing θ, and a stable flood as the invading fluid becomes perfectly wetting to the medium. Surprisingly, this is not what we see in strong imbibition—instead, we observe a dramatic change in both pore-scale displacement mechanisms and macroscopic displacement patterns (Fig. 3-2m–o). Specifically, the invading fluid advances preferentially along the solid surfaces at all Ca (Fig. 3-7b).

For high Ca, the invading fluid advances in leading films along the solid surfaces. For low Ca, the invading fluid instead advances by sequentially coating the perimeters of neighboring posts. The invading fluid bypasses the pore bodies as a result of capillary suction in the corners where the posts meet the top and bottom surfaces of the flow cell. This phenomenon is known as *corner flow*, and has been studied extensively in the context of spontaneous imbibition into angular capillaries [13; 23; 29; 94; 100; 120]. For the wetting fluid to invade the corners, the contact angle must satisfy the geometric relation $\theta < (\pi - \alpha)/2$, where α is the corner angle [23]. For the

right-angled corners present in our flow cell, the critical contact angle for corner flow is then $\theta_{\llcorner} = 45°$, which is between weak imbibition ($\theta = 60°$) and strong imbibition ($\theta = 7°$).

The macroscopic manifestation of corner flow in strong imbibition is the formation of 'chains' of coated posts, where neighboring posts are linked by pendular rings of water (Fig. 3-2b). The propagation of these post chains has certain features in common with strong drainage; for example, the chains propagate outward in a radially symmetric fashion at high Ca (*cf.* viscous fingering, Fig. 3-2n), but become asymmetric at small Ca (*cf.* capillary fingering, Fig. 3-2o).

The pore-scale invasion speed in strong imbibition can be characterized by the coating speed of corner flow, $v_{\llcorner}$. We find $v_{\llcorner} \approx 2$ mm/s in our experiments over more than an order of magnitude change in the injection rate (Fig. 3-6). When the characteristic injection velocity $v_{inj} = Q/(bd)$ far exceeds the coating speed, as in our experiments at high Ca, corner flow is overwhelmed by the formation of leading films. When the injection velocity is comparable to the coating speed, as in our experiment at intermediate Ca, we see a continuous coating process. For even lower injection velocities, as in our experiment at low Ca, we instead see a burst-like invasion process in which clusters of closely spaced posts are rapidly coated, followed by quiescent periods during which the corner films gradually swell (Fig. 3-7d). This burst-like invasion is analogous to the well-studied phenomenon of "Haines jumps" in slow drainage, in which clusters of pores are rapidly invaded, followed by quiescent periods during which the non-wetting fluid slowly swells into the pore throats [11; 38; 77; 81].

The curvature of the interface in corner flow is set by the pressure balance between the capillary pressure in the corner and the pressure difference between the two fluids, as described by the Young-Laplace equation: $\gamma/R = P_{oil} - P_{water}$. This suggests that the radius of curvature R will decrease as Ca increases since higher flow rates increase the absolute pressure difference between the two fluids (*i.e.*, both fluid pressures increase proportional to their own viscosities). We therefore expect corner flow to become less favorable as Ca increases.

For a given interfacial curvature, larger θ ($\theta < \theta_{\llcorner}$) forces the interface farther into

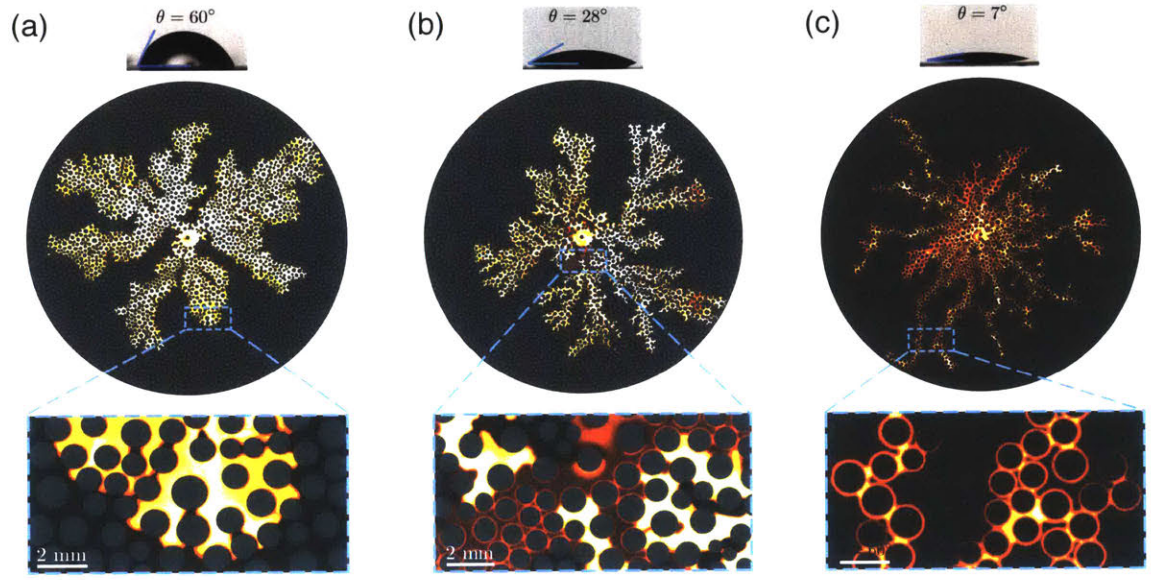

Figure 3-5: Fluid-fluid displacement patterns for (a) weak imbibition ($\theta = 60°$), (b) an intermediate wetting condition ($\theta = 28°$) between weak imbibition and strong imbibition, and (c) strong imbibition ($\theta = 7°$) at Ca= 2.9×10^{-2}. Blue boxes highlight the pore-scale view of the displacement processes. Macroscopically, the displacement pattern in the intermediate wetting condition is less space-filling than weak imbibition, but more space-filling than strong imbibition, in accordance with a critical wetting transition at $\theta_{\llcorner} = 45°$. In weak imbibition, as is the case for strong drainage ($\theta = 150°$), weak drainage ($\theta = 120°$), and neutral ($\theta = 90°$) experiments, the invading fluid advances by displacing the defending fluid from the pore-bodies. This is not the case in strong imbibition, where the invading fluid advances by coating the perimeter of the posts via corner flow, rather than filling the pore bodies. In the intermediate wetting condition ($\theta = 28°$), we observe the co-existence of pore-body displacement and corner flow. This is consistent with the theoretically derived critical contact angle for corner flow of $\theta_{\llcorner} = 45°$. In addition, it is apparent that the width of the corner flow film in the intermediate wetting condition is smaller than that observed in strong imbibition, which is consistent with our analysis that the interface of corner flow will be pushed further into the corner as $\theta \to \theta_{\llcorner}$ (Fig. 3-7c).

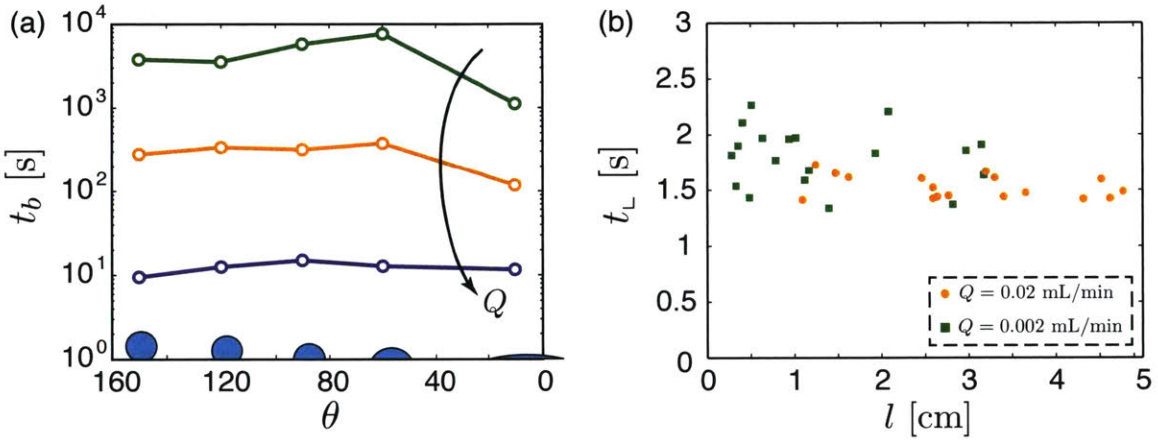

Figure 3-6: (a) We characterize the macroscopic time scale of the experiments as the breakthrough time t_b, which is defined as the amount of time it takes for the displacement front to reach the perimeter of the flow cell. For a given wettability condition, this time scale is controlled by the injection rate Q and is therefore captured by the macroscopic Ca. (b) We characterize the local time scale in strong imbibition as $t_{\llcorner}$, which is defined as the amount time it takes for corner flow to coat a single median-sized post. Here we show $t_{\llcorner}$ for post coating via corner flow at Ca= 2.9×10^{-2} (orange circle) and Ca= 2.9×10^{-3} (green square) as a function of the radial position l where this coating event occurs. We find $t_{\llcorner} \approx 1.5$ s over an order of magnitude change in Q.

the corner, making corner flow less favorable (Fig. 3-7c) [29; 94]. We have validated this prediction with an additional experiment in intermediate imbibition ($\theta = 28°$), which exhibits the coexistence of pore-body displacement and corner flow, as well as thinner corner films (Fig. 3-3).

We expect corner flow to play an important role in strong imbibition in natural porous media like rocks and soils. Natural media typically have angular and irregular grains (Fig. 3-8), which promote corner flow [31]. These grains are also rough, and surface roughness is known to act as an amplifier for wettability: Molecularly hydrophobic and hydrophilic surfaces become macroscopically more hydrophobic and more hydrophilic, respectively, after being roughened [92]. In addition, the greater connectivity between grains in a truly 3D porous medium should further facilitate corner flow.

3.4.4 Evolution of Injection Pressure

To develop further insight into the macroscopic impact of wettability on fluid-fluid displacement, we measure the evolution of the injection pressure (Fig. 3-9). Pressure information in fluid-fluid displacement is of great practical interest in many subsurface technologies, including wastewater disposal [113], geologic sequestration of carbon dioxide [108], and hydraulic fracturing [117], since perturbations in the pore pressure are intimately linked with mechanical deformation of the medium [56]. Existing pressure measurements for fluid-fluid displacement in porous media have been limited to drainage at relatively small Ca, where the capillary pressure dominates [38; 77; 80; 81]. Despite the abundance of studies on radial viscous fingering in porous media (almost entirely in drainage), the associated injection pressures have not been reported in existing literature.

We place the flow cell in a silicone oil bath to enforce a uniform and constant pressure along the perimeter, and to remove capillary edge effects (Fig. 3-1b). The measured pressure is the sum of the capillary pressure across the oil-water interface ΔP_c and the combined viscous pressure loss in the water and oil phases. The viscous pressure loss decreases as the silicone oil is displaced by the much less viscous water.

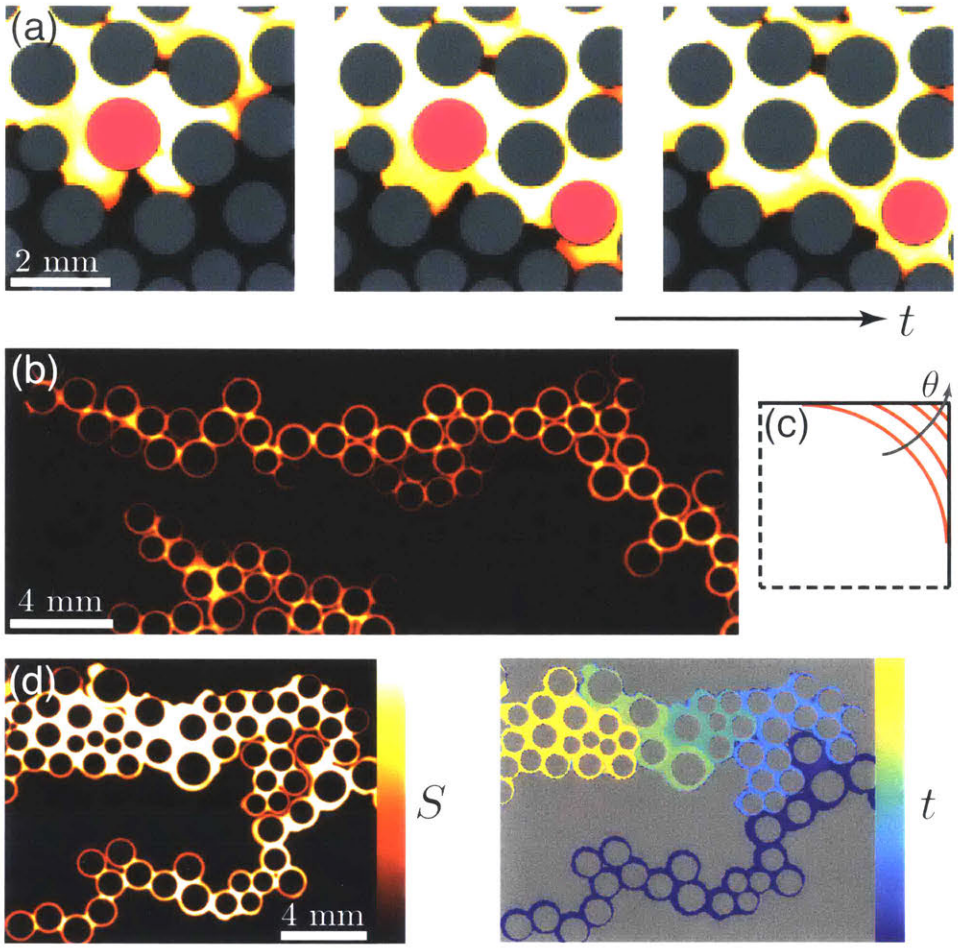

Figure 3-7: (a) Sequence of snapshots from weak imbibition at Ca = 2.9×10^{-3} (Fig. 3-2l). Here, the invading water displaces the defending silicone oil in a cooperative manner: neighboring menisci overlap and form a new, stable meniscus. The posts where this occurs are highlighted in pink. This pore-scale mechanism is directly responsible for the increasing compactness of the macroscopic displacement pattern at θ decreases. (b) Snapshot from strong imbibition at Ca = 2.9×10^{-2} (Fig. 3-2n) illustrating invasion by corner flow: the invading fluid advances by coating the perimeters of the posts rather than by filling the pore bodies. Pendular rings link the coated posts, forming 'chains'. (c) For a given interfacial curvature, the interface is forced farther into the corner as θ increases, thereby reducing the cross-sectional area available for corner flow. The critical contact angle for corner flow in this geometry is $\theta_{\llcorner} = 45°$. (d) Left: A snapshot from strong imbibition at Ca = 2.9×10^{-3} (Fig. 3-2o) shows that the corner films coating the posts swell and expand over time. Right: The same snapshot color coded by invasion time illustrates that strong imbibition at low Ca occurs in a burst-like manner, where groups of closely spaced posts are coated in rapid succession, followed by periods of inactivity.

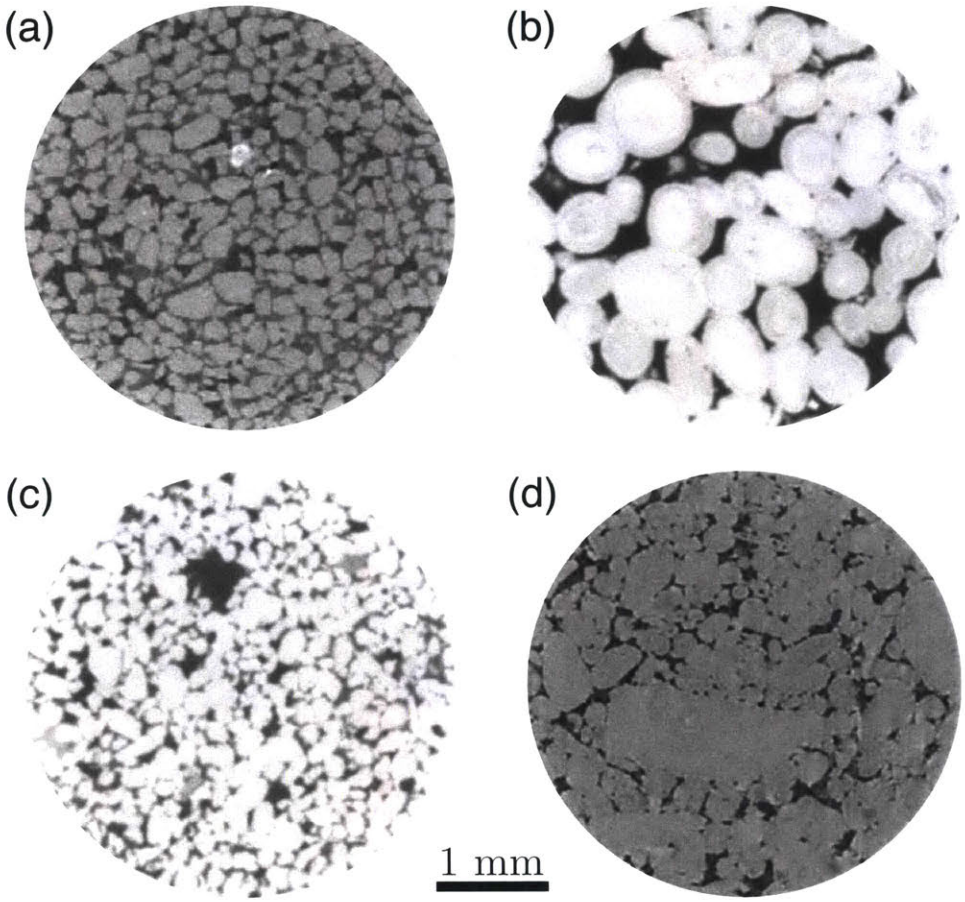

Figure 3-8: X-ray microtomography scans of (a) sand pack, (b) Ketton limestone, (c) Bentheimer sandstone, and (d) Portland limestone. The grains of the porous media appear gray and the pore bodies appear black. These scans illustrate the prevalence of angular pores in natural porous media, which will promote the formation of corner flows. *Adapted from [14].*

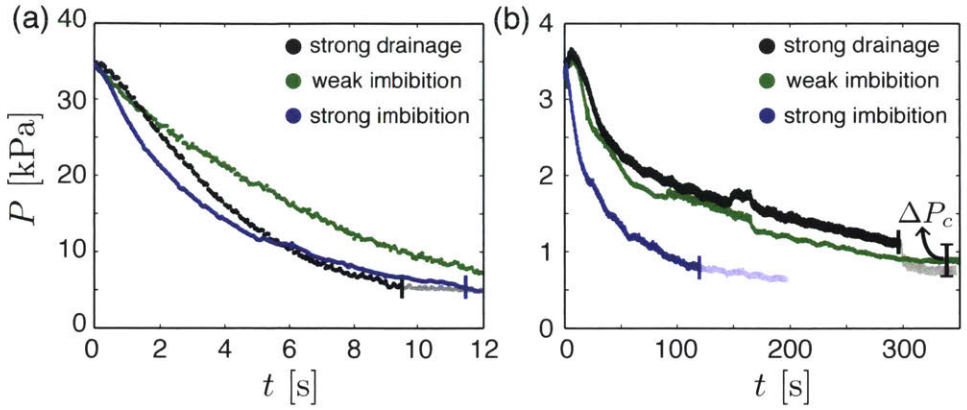

Figure 3-9: Evolution of the injection pressure during strong drainage, weak imbibition, and strong imbibition at (a) Ca $= 2.9 \times 10^{-1}$ and (b) Ca $= 2.9 \times 10^{-2}$. The pressure measurements are shifted in time so that $t = 0$ s is the time when the invading water first enter the flow cell. The end of each experiment (*i.e.*, the time when the water first reaches the perimeter of the flow cell) is marked with a vertical line and subsequent measurements are translucent. (b) The sudden drop in injection pressure as the water exits the flow cell in strong drainage corresponds to the capillary pressure ΔP_c across the oil-water interface.

The characteristic capillary pressure in strong drainage is $\Delta P_c \approx 2\gamma(1/b + 1/d) \approx 0.3$ kPa, where b is the gap thickness of the flow cell and d is the median pore-throat size [67]. This is consistent with the observed ΔP_c in strong drainage (Fig. 3-9b).

One might expect wettability to have a weak impact on injection pressure at moderate to high Ca, where the capillary pressure itself becomes small relative to the viscous pressure loss. Instead, we find that wettability exerts a powerful control over the evolution of the injection pressure at all Ca, and the injection pressures for different wettability conditions differ by much more than the capillary pressure itself (Fig. 3-9). This is because the viscous pressure is intimately linked to the displacement efficiency E_d—higher pressure is needed for more completely displacement of the viscous silicone oil. The connection between the viscous pressure loss and the wettability-mediated displacement efficiency is clearly reflected in the seemingly counter-intuitive finding that at high Ca, weak imbibition requires the highest driving pressure, while the driving pressure for strong drainage and strong imbibition are roughly the same (Fig. 3-4). This agrees well with the non-monotonic change in E_d between strong drainage (E_d=0.1), weak imbibition (E_d=0.12), and strong imbibi-

tion (E_d=0.1). We find the viscous pressures follow the same ordering by wettability at the intermediate Ca after taking account of the characteristic capillary pressure ($\Delta P_c \approx 0.3$ kPa), where weak imbibition (E_d=0.33) requires the highest driving pressure, followed by strong drainage (E_d=0.25) and strong imbibition (E_d=0.1). In addition, the injection pressure decreases much more sharply in strong imbibition than in strong drainage or weak imbibition, reflecting the unique displacement mechanisms in strong imbibition: The invading fluid advances along the corners, bypassing the pore bodies, and this rapidly reduces the viscous pressure loss.

3.5 Conclusions

We have systematically investigated the impact of wettability on multiphase flow in porous media via fluid-fluid displacement experiments in patterned microfluidic flow cells with controlled wetting properties.

We have shown that fluid-fluid displacement at high Ca is dominated by the formation of wetting films on the solid surfaces for all wettability conditions, which leads incomplete displacement at the pore scale. In drainage, these are trailing films of the more viscous defending fluid; in imbibition, they are leading films of the less viscous invading fluid. We have further shown that the displacement pattern becomes more compact as the invading fluid becomes more wetting to the medium (*i.e.*, decreasing θ; Fig. 3-2), which leads to more efficient displacement of the defending fluid (Fig. 3-4). Through visualization of fluid flow at the pore-scale, we have provided direct experimental evidence that the more compact invasion front stems from cooperative pore filling (Fig. 3-7a). Our experiments have revealed that the trend of increasingly compact displacement with decreasing θ is unexpectedly reversed as the system exhibits a wetting transition between weak imbibition ($\theta = 60°$) and strong imbibition ($\theta = 7°$). We have shown that this dramatic change is caused by corner flow, which allows the invading fluid to propagate without filling the pore bodies. We have observed marked differences in the evolution of the injection pressure between experiments under different wettability conditions, even at large capillary numbers

where viscous pressure dominates over capillary pressure. This finding underscores the significant control wettability exerts on the efficiency of the displacement, which is strongly connected to the viscous pressure drop across the flow cell.

Our results highlight the inherently 3D nature of multiphase flow in porous media, which manifests itself through physical mechanisms such as film formation and corner flow. These wettability-controlled mechanisms have a fundamental impact on multiphase flow, making them challenging but essential ingredients in pore-scale and continuum-scale descriptions. Our microfluidics study of the fundamental mechanisms paves the way for the interpretation and further investigation of wettability control on multiphase flow in natural porous media, which often exhibit spatial heterogeneity in wettability [78; 112], surface roughness [1; 92], and pre-existing wetting layers [60].

3.6 Materials and Methods

3.6.1 Post Pattern Design

To create the post pattern, we first generate an irregular triangular mesh inside a circle using the `pdemesh` tool in MATLAB. We use the nodes of the triangular mesh as the centers of the posts. We then assign the radius of each post to be 45% of the distance to its nearest neighbor, which provides a random distribution of non-overlapping posts. Detailed statistics of the post size and the pore-throat size distributions are provided in Fig. 3-10.

3.6.2 Microfluidic Flow Cell Fabrication

We fabricate the microfluidic cells via soft imprint lithography, following the procedures detailed in Bartolo et al. [7]. We first generate a silicon master of the post pattern via conventional photo-lithography techniques. We spin coat a negative photoresist (SU8-2050, MicroChem, USA) onto a 6" silicon wafer at 1,700 rpm for 30 s to achieve a film thickness of 100 μm. After soft baking, we expose the photoresist to UV

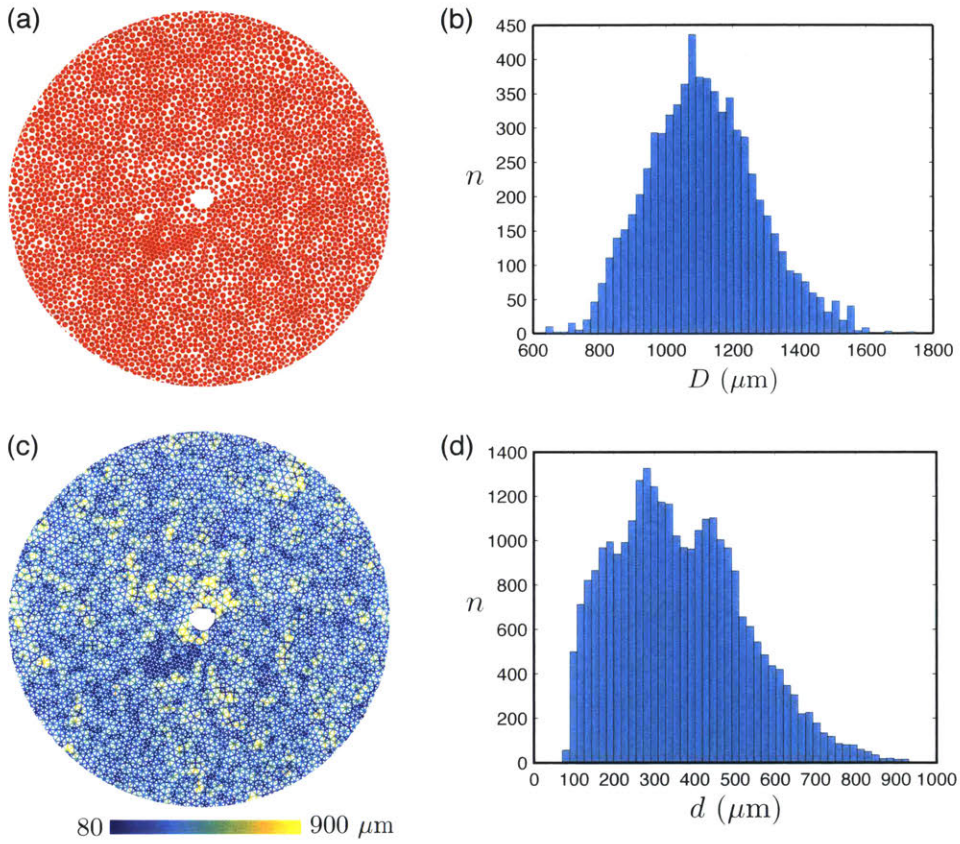

Figure 3-10: To create the post pattern, we first generate an irregular triangular mesh inside a circle using the `pdemesh` tool in MATLAB. We use the nodes of the triangular mesh as the centers of the posts. We then assign the radius of each post to be 45% of the distance to its nearest neighbor, which provides a random distribution of non-overlapping posts. (a) Post pattern. (b) The post sizes follow a Gaussian distribution that ranges from 600 to 1700 μm. (c) The spatial distribution of pore-throat sizes. (d) The pore-throat sizes range from 80 to 900 μm.

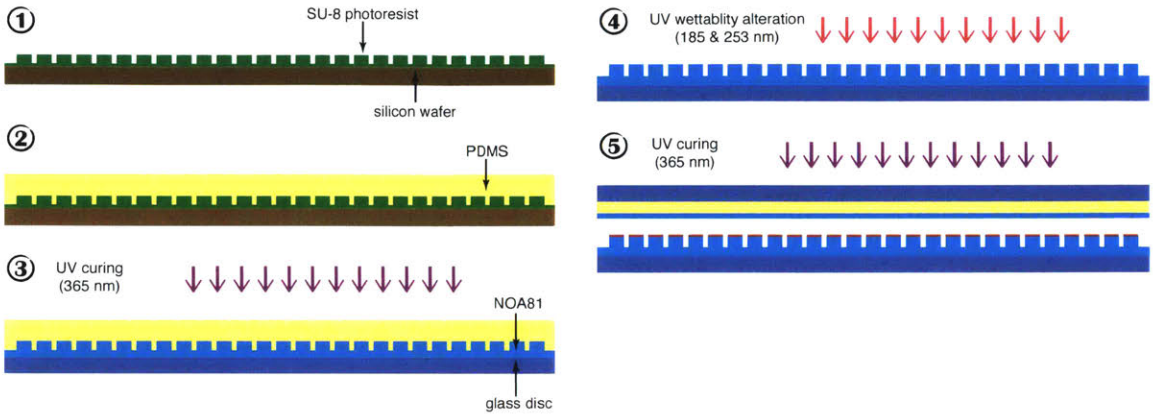

Figure 3-11: We fabricate the microfluidic flow cells via soft imprint lithography, following the steps illustrated above: (1) We first generate a silicon master of the post pattern via conventional photo-lithography techniques. We spin coat a negative photoresist (SU8-2050, MicroChem, USA) onto a 6" silicon wafer at 1,700 rpm for 30 s to achieve a film thickness of 100 μm. After soft baking, we expose the photoresist to UV light through a photomask of the post pattern, which selectively polymerizes the photoresist to form the posts. We subject the photoresist to post-exposure-bake, and developed with ethyl lactate to dissolve the unexposed areas of the photoresist. (2) We use the silicon master to create PDMS (Sylgard 184, Dow-Corning, USA) casts of the post pattern. The PDMS cast forms a negative complement of the silicon master, which consists of wells rather than posts. (3) The core of the flow cell is made of a photo-curable polymer (NOA81, Norland Optics, USA) and it consists of a flat top half and a bottom half that contains the post structures. To make the bottom half of the microfluidic cell, we first deposit a puddle of NOA81 onto a 4" glass disc. We allow the NOA81 to spread across the glass disc before carefully covering it with the PDMS cast. Upon contact, the NOA81 spontaneously fills the wells in the PDMS cast. After removing any excess NOA81 with a metal roller, we cure it with a collimated 365 nm UV light source (MA4-1, Karl Suss, Germany) for 15 s at 25 mW/cm^2. (4) We peel off the PDMS cast after curing, and subject the NOA81 to wettability alteration (see fig. S3). (5) After wettability alteration, we bind the flat NOA81 piece and the patterned NOA81 piece together with 365 nm UV radiation for 60 s at 25 mW/cm^2.

light through a photomask of the post pattern, which selectively polymerizes the photoresist to form the posts. The photoresist is then subjected to post-exposure-bake, and developed with ethyl lactate to dissolve the unexposed areas of the photoresist. We use the silicon master to create PDMS (Sylgard 184, Dow-Corning, USA) casts of the post pattern. The PDMS cast forms a negative complement of the silicon master, which consists of wells rather than posts. The core of the flow cell is made of a photo-curable polymer (NOA81, Norland Optics, USA) and it consists of a flat top half and a bottom half that contains the post structures (Fig. 3-1). To make the bottom half of the flow cell, we first deposit a puddle of NOA81 onto a 4" glass disc. We allow the NOA81 to spread across the glass disc before carefully covering it with the PDMS cast. Upon contact, the NOA81 spontaneously fills the wells in the PDMS cast. After removing any excess NOA81 with a metal roller, we cure it with a collimated 365 nm UV light source (MA4-1, Karl Suss, Germany) for 15 s at 25 mW/cm^2. We peel off the PDMS cast after curing, and the bottom half of the flow cell is now ready for wettability alteration (see next section). To make the top half of the flow cell, we sandwich a puddle of NOA81 between two flat PDMS discs (4" diameter) separated by 100-μm thick precision metal shims. After the NOA81 fills the gap between the two flate PDMS discs, we cure it with the MA4-1 for 60 s at 25 mW/cm^2. We peel off one of the PDMS discs after curing, and the top half of the flow cell is now ready for wettability alteration (see next section). The entire fabrication workflow is illustrated in Fig. 3-11.

3.6.3 Wettability Alteration

We characterize the wettability of our system by placing a small drop of DI water on a treated NOA81 surface submerged in a silicone oil-filled reservoir. We image the water drop with a contact angle goniometer (model 250, ramé-hart, USA), which measures the water/silicone oil contact angle via its `DROPimage` software. All contact angle measurements are made 24 hrs after treatment, which corresponds to the typical amount of time elapsed between wettability alteration of the flow cell and the fluid-fluid displacement experiment. The images obtained from the contact angle

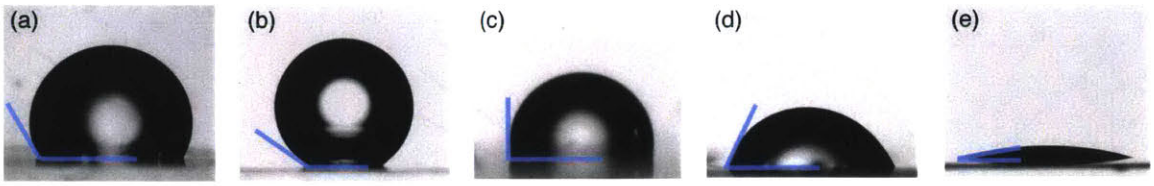

Figure 3-12: We characterize the wettability of our system by placing a small drop of DI water on a treated NOA81 surface submerged in a silicone oil-filled reservoir. We image the water drop with a contact angle goniometer (model 250, ramé-hart, USA), which measures the water/silicone oil contact angle via its `DROPimage` software. All contact angle measurements are made 24 hrs after treatment, which corresponds to the typical amount of time elapsed between wettability alteration of the flow cell and the fluid-fluid displacement experiment. (a) The contact angle of water on an untreated NOA81 surface immersed in silicone oil is $\theta = 120° \pm 3°$. (b) To make the NOA81 surface more hydrophobic, we apply chemical vapor deposition (CVD) of trimethoxysilane in a desiccator for 30 mins, which yields a contact angle of $\theta = 150° \pm 5°$. To make the NOA81 surface more hydrophilic, we expose it to high-energy UV light in a UV-ozone cleaner (UV-1, Samco, Japan), which generates UV light that peaks at 185 & 253 nm. By varying the duration of UV exposure (t_{UV}), we achieve contact angles of (c) $\theta = 90° \pm 7°$ (t_{UV} = 85 s), (d) $\theta = 60° \pm 5°$ (t_{UV} = 210 s), and (e) $\theta = 7° \pm 3°$ (t_{UV} = 1800 s).

measurements are provided in Fig. 3-12. The contact angle of water on an un-treated NOA81 surface immersed in silicone oil is $\theta = 120° \pm 3°$. NOA81 is a thiolene-based polymer that gains surface energy through deep UV radiation, due to the formation of peroxide groups [68]. We make the NOA81 surface more hydrophilic by exposing it to high-energy UV light in a UV-ozone cleaner (UV-1, Samco, Japan). By varying the duration of UV exposure (t_{UV}), we achieve contact angles of $\theta = 90° \pm 7°$ (t_{UV} = 85 s), $\theta = 60° \pm 5°$ (t_{UV} = 210 s), and $\theta = 7° \pm 3°$ (t_{UV} = 1800 s). To make the NOA81 surface more hydrophobic, we apply chemical vapor deposition (CVD) of trimethoxysilane in a desiccator for 30 mins, which yields a contact angle of $\theta = 150° \pm 5°$.

3.6.4 Experimental Setup

To perform an experiment, we start by injecting silicone oil (350 cSt, Sigma Aldrich, USA) into the flow cell, which sits in an empty reservoir. After the flow cell is fully saturated, we carefully pour the silicone oil into the reservoir, until it rises to cover

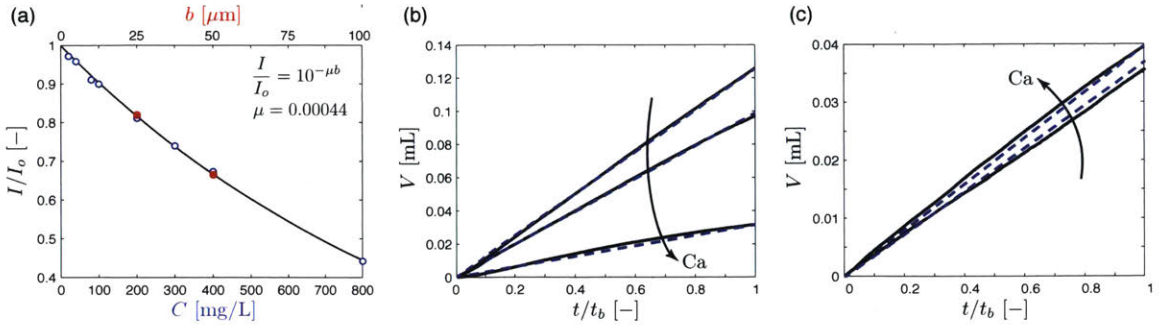

Figure 3-13: To gain more information about the fluid-fluid displacement in 3D, we seed the injected water with a light absorbing dye (Brilliant Blue G, Alfa Aesar, USA) and measure the gap-averaged water saturation from the transmitted light intensity via a calibration curve. (a) We experimentally generate a calibration curve that relates the normalized transmitted-light intensity I/I_o to the dye concentration C in the water solution (blue circles), which is well-described by the Beer-Lambert law (solid line). We further find an one-to-one relationship in the transmittence of water films of different dye concentrations at a fixed thickness (100 μm), and water films of different thicknesses at a fixed concentration (800 mg/L; red dots). This allows us to convert the measured transmitted-light intensity to the gap-averaged water saturation. (b – c) We test the accuracy of the quantified water saturation by comparing the injected volume calculated from the images (solid line) with the actual injected volume (dashed line) as a function of normalized time t/t_b, where t_b is the amount of time it takes for the invading fluid to reach the edge of the flow cell. We show the comparison here for (b) strong drainage and (c) strong imbibition. We do not show the volume evolution for strong imbibition at $\mathrm{Ca} = 2.9 \times 10^{-1}$ here as it overlaps with strong imbibition at $\mathrm{Ca} = 2.9 \times 10^{-2}$.

the gap of the flow cell. To initiate the experiment, we inject DI water at prescibed volume rates using a syringe pump (PHD 2000, Harvard Apparatus, USA). We image the fluid-fluid displacement via a scientific camera (Orca Flash 4.0, Hamamatsu, Japan) mounted directly above the center of the microfluidic cell. The scientific camera has a CMOS sensor with 2048×2048 pixels, which yields a spatial resolution of $a = 52$ μm/pixel.

3.6.5 Water Saturation Quantification

We seed the injected water with a light absorbing dye (Brilliant Blue G, Alfa Aesar, USA) at 800 mg/L concentration. We experimentally generate a calibration curve that relates the transmitted-light intensity to the dye concentration in the water

solution, which is well-described by the Beer-Lambert law. We further find an one-to-one relationship in the transmittence of water films of different dye concentrations at a fixed thickness, and water films of different thicknesses at a fixed concentration. This allows us to convert the measured transmitted-light intensity to the gap-averaged water saturation. The calibration curve is presented in Fig. S4. To account for the small temporal fluctuations of the light panel, we numerically adjust the images so that the average recorded intensity outside the flow cell stays the same during a particular experiment. We test the accuracy of the quantified water saturation by calculating the total injected volume as $V = \sum abS$, which corresponds well to the actual injected volume (Fig. 3-13).

3.6.6 Pressure Measurements

We connect a pressure transducer (uPS0250-T116-10, Labsmith, USA) to a stiff injection tube (TUBE116-030P, Labsmith, USA) via a T-connector 3 cm below the flow cell. The transducer operates within a pressure range of $0 - 250$ kPa and at a sampling frequency of 50 Hz, with a resolution of 1 Pa. We subtract the hydrostatic pressure generated by the column of water in the injection tube directly below the flow cell from the raw pressure measurements to produce the data presented in Fig. 3-9.

Chapter 4

Wettability effects on fluid-fluid displacement in a capillary tube

In this Chapter, we study the impact of wettability on fluid-fluid displacement in a capillary tube. Fluid-fluid displacement in a capillary tube is a classical problem in fluid mechanics, and it serves as a simple, but important analogue to multiphase flow in porous media. Despite many experimental and modeling studies of this problem, several key phenomena remain poorly understood. Here we experimentally study the constant-rate displacement of a glycerol-air fluid pair in a capillary tube. By treating the inside of the capillary, we obtain two distinct wetting conditions. We visualize the dynamics of the glycerol-air interface in high-resolution for both viscously favorable and viscously unfavorable displacement under a wide range of capillary numbers (Ca). In viscously favorable displacement, the glycerol-air interface bends further into the less viscous air with increasing Ca under both wetting conditions. While the interface always remains as a spherical cap in viscously favorable displacement, this is true in viscously unfavorable displacement only at small Ca. At large Ca, the invading air forms a finger that advances along the center of the tube, leaving behind the contact line and a macroscopic film of the viscous glycerol on the tube wall. We find that both the critical capillary number Ca^* at which film formation occurs and the speed of the contact line are strongly controlled by the wettability of the tube.

4.1 Introduction

The displacement of one fluid by another immiscible fluid in small, confined geometries is an important process in many natural and industrial settings, including water infiltration into soil [25], enhanced oil recovery [87], ink-jet printing [55], and microfluidics [121]. A particularly challenging aspect of describing fluid-fluid displacement in the presence of a solid is the movement of the contact line between the two fluid phases and the solid surface (*i.e.* three-phase contact line), which violates the no-slip boundary condition commonly assumed in classical fluid mechanics [15; 49]. Capillary tubes are an ideal experimental system for studying this problem due to their simple, well-defined shape, which allows for unobstructed visualization of the fluid-fluid interface and the contact line.

Two key characteristics that describe fluid-fluid displacement in the presence of a solid are viscosity contrast and wettability. From the perspective of viscosity contrast, the displacement can either be characterized as viscously favorable if the invading fluid is more viscous than the defending fluid or viscously unfavorable in the opposite case. From the perspective of wettability, the displacement can either be characterized as drainage or imbibition. Drainage refers to the regime where the invading fluid is less wetting to the solid surface than the defending fluid. Imbibition refers to the opposite case, where the invading fluid is more wetting to the solid surface than the defending fluid. Recent experiments in Hele-Shaw cells [69] and in micromodels [127] have demonstrated that the interplay between viscosity contrast and wettability in fluid-fluid displacement can lead to complex 3D flow dynamics even in quasi-2D geometries. Due to the planar nature of these experiments, the contact line could not be directly visualized.

Viscously favorable imbibition has been studied extensively in the context of capillary rise [36; 103; 118; 129] and forced imbibition [35; 45; 46] experiments. These studies observed that the fluid-fluid interface deforms during the displacement process. The magnitude of the interface deformation is a function of the capillary number, which measures the strength of viscous forces relative to capillary forces. Compared to

the wealth of observations on viscously favorable imbibition, experiments of viscously favorable drainage have been relatively scarce. Here, we study viscously favorable displacements under two distinct wetting conditions. Our experiments confirm existing results on viscously favorable imbibition and add new data on viscously favorable drainage.

Viscously unfavorable drainage has been studied in the classical experiments of Taylor [109] and Bretherton [16]. They found that as air invades into a capillary tube initially filled with a wetting, viscous defending fluid, it leaves a film of the defending fluid coating the tube walls in its wake. Thanks to these seminal works, we now have a fairly good understanding of how the thickness of the wetting film varies as a function of the capillary number. In contrast, the behavior of the contact line during this process has not been studied in any detail. Here, we study viscously unfavorable displacements under two distinct wetting conditions, paying particular attention to the movement of the contact line. Our results demonstrate the fundamental control wettability exerts on the contact line during fluid-fluid displacement.

4.2 Capillary Tube Experiments

We conduct fluid-fluid displacement experiments in precision-made borosilicate glass capillary tubes with inner diameter $d = 750$ μm. We wash the capillary tubes thoroughly with methanol and isopropyl alcohol, followed by ultrasonic cleaning in a de-ionized water bath (see Sec. 4.5.1). The capillary tubes are hydrophilic (*i.e.*, wetting to glycerol) after the washing process, having a static advancing contact angle $\theta^{\mathrm{w}}_{\mathrm{adv}} = 28°$ and a static receding contact angle $\theta^{\mathrm{w}}_{\mathrm{rec}} = 20°$ (Fig. 4-12a). To alter the wettability of the capillary tubes, we apply heat-assisted chemical vapor deposition (CVD) of trichlorosilane in a vacuum chamber (Fig. 4-11). The silane-coated capillary tubes are hydrophobic (*i.e.*, non-wetting to glycerol), having a static advancing contact angle $\theta^{\mathrm{nw}}_{\mathrm{adv}} = 118°$ and a static receding contact angle $\theta^{\mathrm{nw}}_{\mathrm{rec}} = 75°$ (Fig. 4-12b). We use each capillary tube only once to ensure precise control over its wettability.

The capillary tube is open to the atmosphere on one end and connected to a syringe

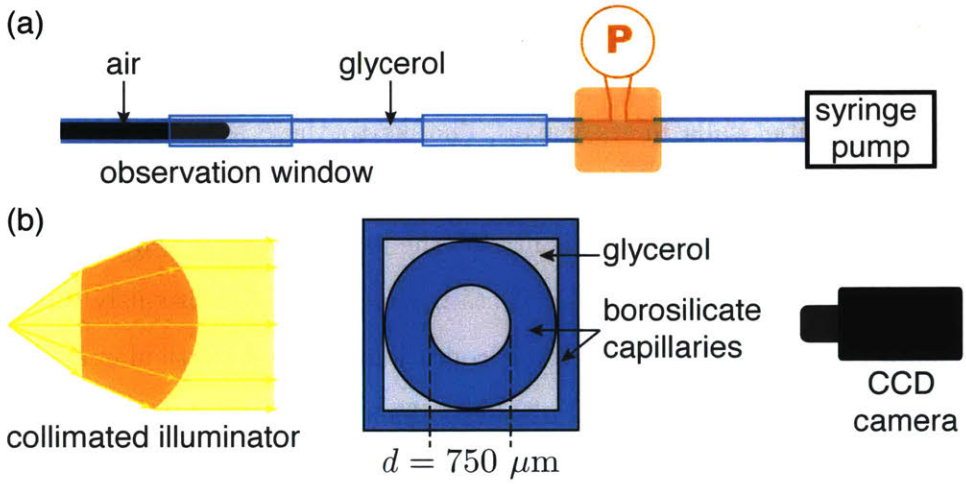

Figure 4-1: We study fluid-fluid displacement in circular capillary tubes. (a) The capillary tube is open to the atmosphere on one end and connected to a syringe pump on the other. For viscously favorable displacement, we inject glycerol into the capillary tube to displace air. For viscously unfavorable displacement, we withdraw glycerol from the capillary tube so that air displaces glycerol. We connect a pressure sensor to one end of the capillary tube to track pressure evolution during the displacement process (Fig. 4-10). (b) We use precision-made borosilicate glass capillary tubes with inner diameter $d = 750\ \mu$m. The circular capillary tube is housed in a slightly larger square capillary tube filled with glycerol, which has the same refractive index as borosilicate glass. The combination of a collimated light source and a glycerol-filled square borosilicate glass housing eliminates light refraction through the capillary tube, which enables clear, undistorted visualization of the fluid-fluid interface via a CCD camera.

pump on the other. For viscously favorable displacement, we inject pure glycerol into the capillary tube to displace air. For viscously unfavorable displacement, we withdraw glycerol from the capillary tube so that air displaces glycerol. We connect a pressure sensor to one end of the capillary tube to track the pressure evolution in glycerol during the displacement process (Fig. 4-1; Fig. 4-10).

The fluid-fluid displacement process is controlled by capillary forces, inertial forces, and viscous forces. The relative importance between these forces can be characterized by three dimensionless quantities, namely the Reynolds number (Re), the Weber number (We), and the capillary number (Ca). Specifically, $\mathrm{Re} = \rho U d/\mu$ measures the ratio of inertial forces to viscous forces; $\mathrm{We} = \rho U^2 d/\gamma$ measures the ratio of inertial forces to capillary forces; and $\mathrm{Ca} = \mu U/\gamma$ measures the ratio of viscous forces to capillary forces. Here, $U = 4Q/(\pi d^2)$ is the characteristic displacement velocity, $\gamma = 71 \pm 2$ mN/m is the surface tension of glycerol in air, $\rho = 1260$ kg/m^3 and $\mu = 1400$ mPa $\cdot$ s are the density and the dynamic viscosity of glycerol at 20 °C, respectively. We adopt the sign convention that U is positive if air displaces glycerol, and that U is negative if glycerol displaces air. We vary the displacement rate Q over four orders of magnitude in a series of experiments, which correspond to $|\mathrm{Re}| \in [5.0 \times 10^{-7}, 3.2 \times 10^{-3}]$, $|\mathrm{We}| \in [7.6 \times 10^{-12}, 3.1 \times 10^{-4}]$, and $|\mathrm{Ca}| \in [1.5 \times 10^{-5}, 9.6 \times 10^{-2}]$. The absolute values of the Ca are much greater than those of the Re and the We, which suggest the displacement process is dominated by the interplay between viscous forces and capillary forces in our experiments. We have neglected gravitational forces here since the capillary length $l_c = \sqrt{\gamma/\rho g} \approx 2.4$ mm is much larger than the inner diameter of the capillary tube.

4.3 Experimental Results

4.3.1 Viscously Favorable Displacement

Hoffman [45] studied viscously favorable imbibition via constant-rate displacement of air by a viscous wetting fluid in a capillary tube. He observed that the fluid-fluid

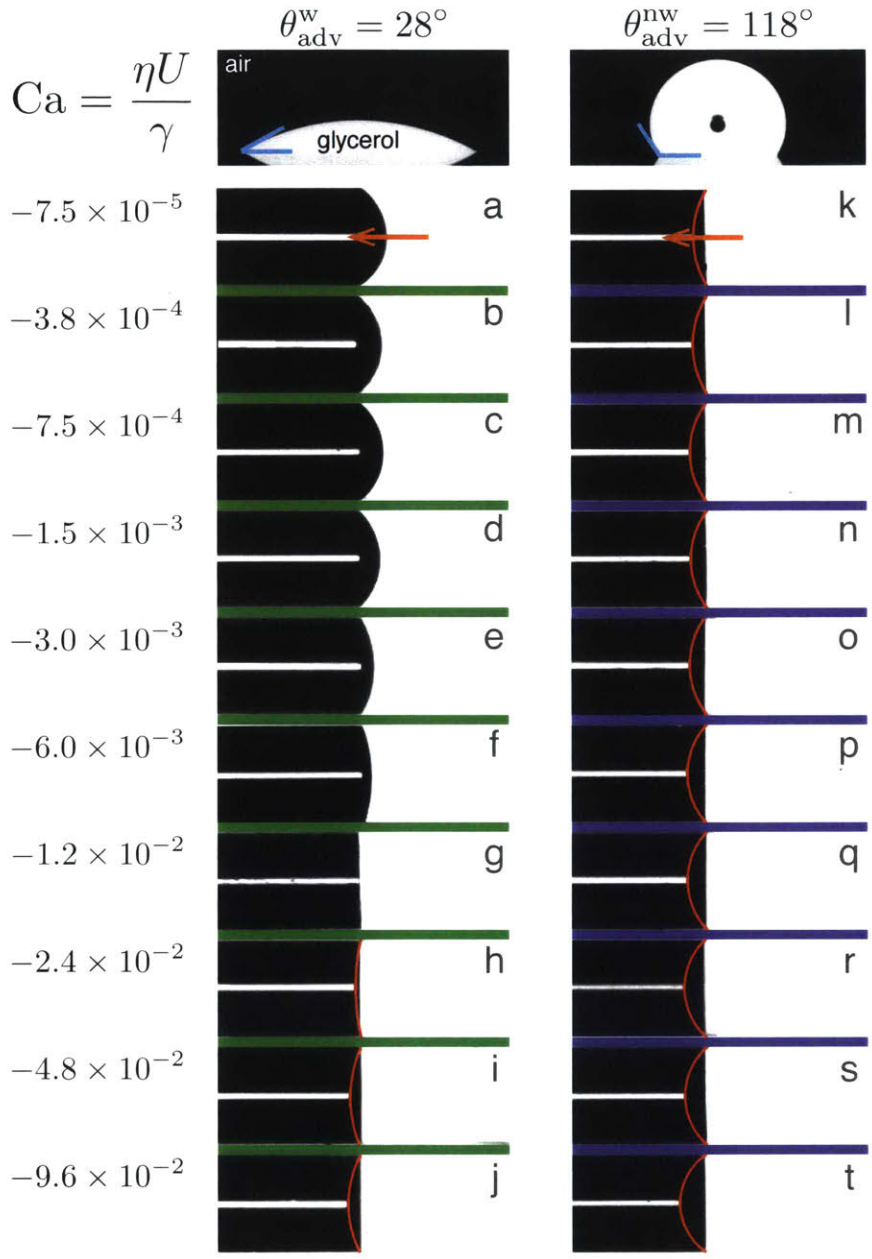

Figure 4-2: Fluid-fluid interface of glycerol (white) displacing air (black) under increasing absolute capillary numbers (top to bottom) in a hydrophilic capillary tube (a–j) and a hydrophobic capillary tube (k–t). The orange arrows indicate the direction of interface displacement. Red lines represent the interface profile calculated using Eq. (4.12)b. Under both wettability conditions, the fluid-fluid interface bends further into the air phase with increasing absolute capillary numbers. In particular, the interface in the hydrophilic capillary tube transitions from having a negative curvature (a–f) to having a positive curvature (g–j) as the absolutely capillary number increases.

interface deforms from its equilibrium shape during the displacement process, and that the magnitude of the interface deformation is a function of the capillary number. As a result, the interface intersects the tube wall at a dynamic contact angle θ_D that is different from the static advancing contact angle θ_{adv} of the system. The dynamic contact angle is found to be a function of the capillary number, and that for a perfectly wetting fluid (*i.e.*, $\theta_{\text{adv}} = 0$), $\theta_D \sim |\text{Ca}|^{\frac{1}{3}}$ for $|\text{Ca}| < 1$.

In our experiments, we find the fluid-fluid interface bends further into the air phase with increasing absolute capillary numbers in both the hydrophilic and the hydrophobic capillary tubes (Fig. 4-2). In particular, the interface in the hydrophilic capillary tube transitions from having a negative curvature (Fig. 4-2a–f) to having a positive curvature (Fig. 4-2g–j) as the absolutely capillary number increases. To quantify the interface deformation as a function of Ca, we extract the apparent θ_D via image analysis (Fig. 4-3a; see also Sec. 4.5.2).

The relationship between θ_D and Ca for partially wetting fluids (*i.e.*, $\theta_{\text{adv}} > 0$) has been studied theoretically within the framework of the lubrication approximation, by balancing viscous forces and capillary forces [24; 115; 116]:

$$\theta_D{}^3 = \theta_M{}^3 + 9|\text{Ca}| \ln(L/l), \tag{4.1}$$

where θ_M is the microscopic contact angle of the system, L is the macroscopic length scale of the problem, and l is the microscopic length scale of the system. Assuming $\theta_M = \theta_{\text{adv}}$, we find that $\theta_D{}^3 - \theta_M{}^3$ scales linearly with Ca for $\theta_D < 135°$ in both the hydrophilic and the hydrophobic capillary tubes (Fig. 4-3a inset).

4.3.2 Viscously Unfavorable Displacement

The behavior of viscously unfavorable displacement is summarized in a phase diagram of the fluid-fluid interface under increasing Ca (Fig. 4-4). At small Ca, the fluid-fluid interface translates via contact-line motion and the invading air completely displaces the viscous glycerol. In this regime, θ_D decreases monotonically with increasing Ca (Fig. 4-5), approaching 0 at a finite, critical capillary number Ca*. Above

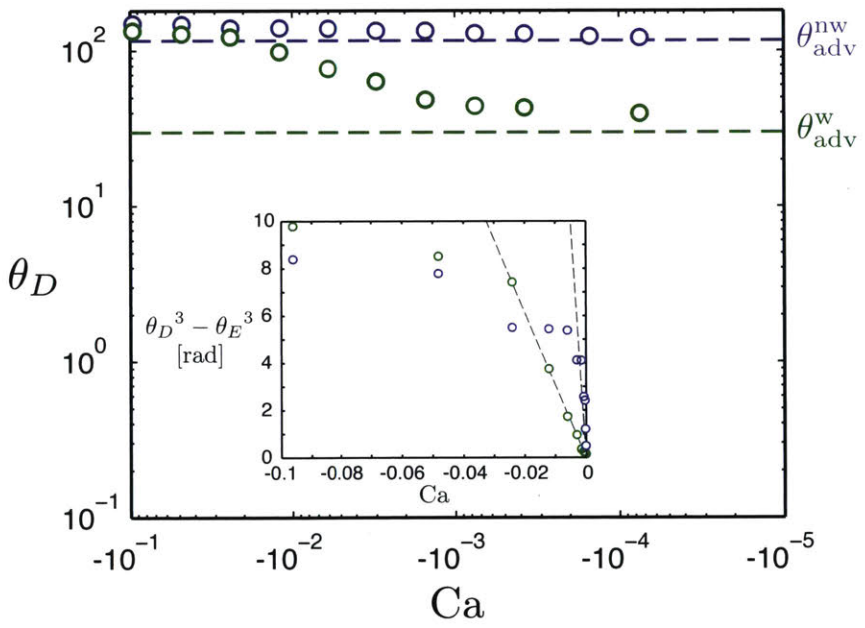

Figure 4-3: Dynamic contact angle θ_D as a function of Ca in viscously favorable displacements (glycerol displacing air) in a hydrophilic tube (green symbols) and a hydrophobic tube (purple symbols). The lower bound of θ_D is set by the static advancing contact angle θ_{adv} of the system (horizontal dashed lines). Under both wetting conditions, θ_D (open circles) increases monotonically with increasing absolute capillary numbers |Ca|. Additionally, ${\theta_D}^3 - {\theta_M}^3$ scales linearly with Ca for $\theta_D < 135°$ (inset), in accordance with existing hydrodynamic theories [24; 115; 116].

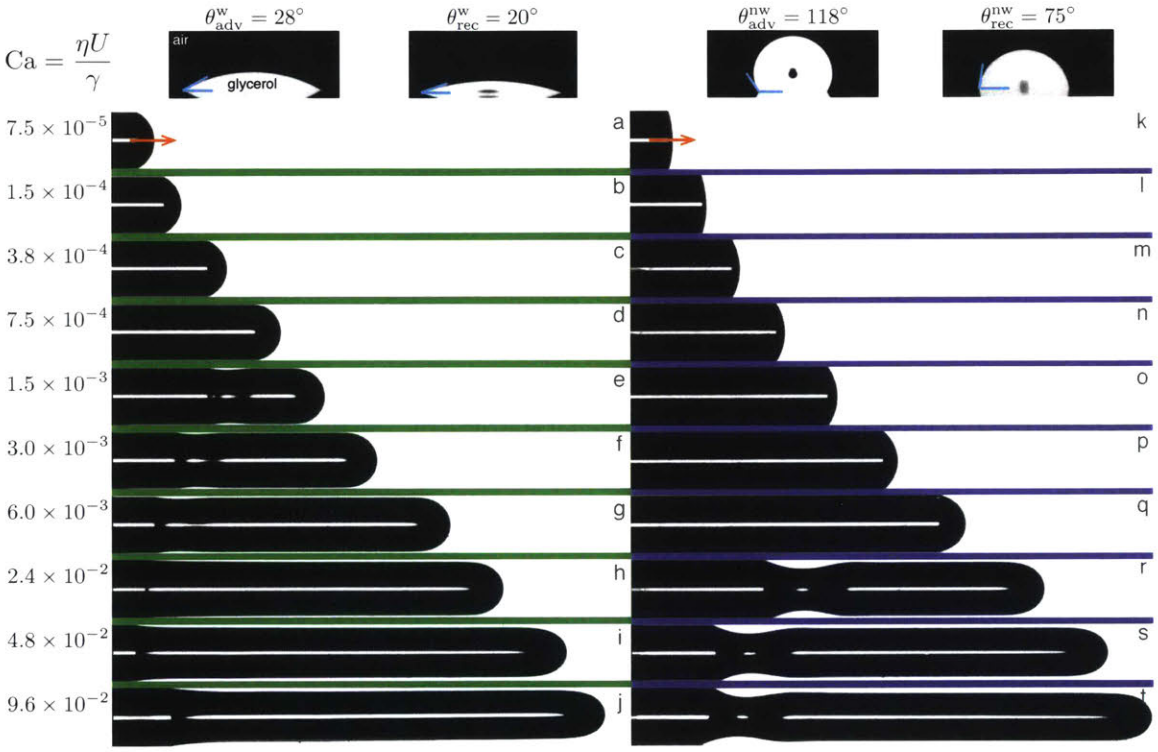

Figure 4-4: Fluid-fluid interface of air (black) displacing glycerol (white) under increasing capillary numbers (top to bottom) in a hydrophilic capillary tube (a–j) and a hydrophobic capillary tube (k–t). The orange arrows indicate the direction of interface displacement. At small Ca, the fluid-fluid interface remains as a spherical cap. At large Ca, however, viscous forces dominate capillarity and the invading air forms a single finger that advances along the center of the tube, leaving a macroscopic trailing film of glycerol on the tube walls. The critical capillary number Ca^* at which film formation occurs is controlled by wettability—it is much smaller in the hydrophilic capillary tube than in the hydrophobic capillary tube.

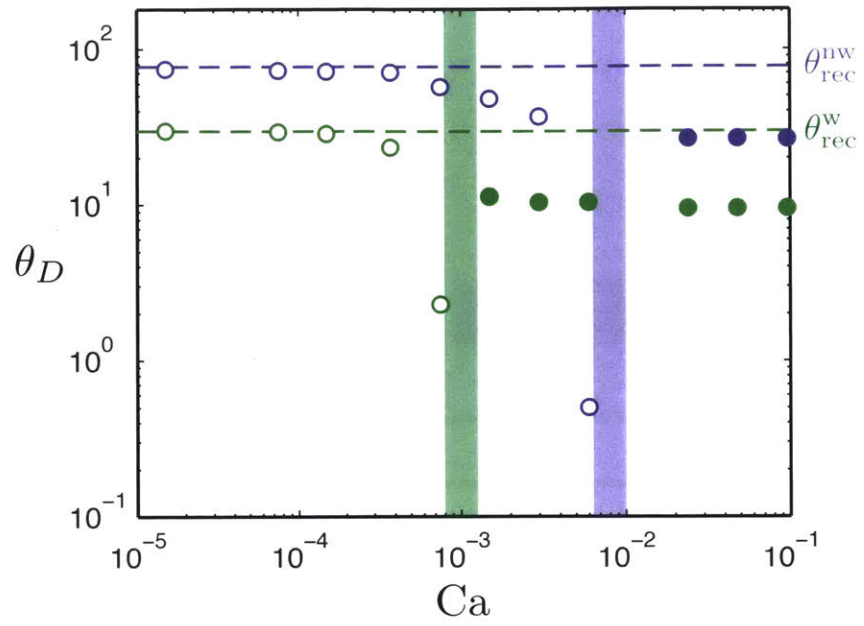

Figure 4-5: Dynamic contact angle θ_D as a function of Ca in viscously unfavorable displacements (air displacing glycerol) in a hydrophilic tube (green symbols) and a hydrophobic tube (purple symbols). The upper bound of θ_D is set by the static receding contact angle θ_{rec} of the system (horizontal dashed lines). At small Ca, the fluid-fluid interface translates via contact-line motion and the invading air completely displaces the viscous glycerol. In this regime, θ_D (open circles) decreases monotonically with increasing Ca, approaching 0 at a finite, critical capillary number Ca^* (shaded regions). Above Ca^*, a spherical cap construction of the fluid-fluid interface is no longer possible and the invading air forms a single finger that advances along the center of the tube, leaving a macroscopic trailing film of the viscous glycerol on the tube walls. In this regime, $0 < \theta_D < \theta_{\mathrm{rec}}$ at the trailing contact line (filled circles) is set by the wettability of the capillary tube, and is independent of Ca.

Ca^*, a spherical cap construction of the fluid-fluid interface is no longer possible and the invading air forms a single finger that advances along the center of the tube, leaving a macroscopic trailing film of the viscous glycerol on the tube walls (Fig. 4-4). The Ca^* at which the displacement process transitions from complete displacement via contact-line motion to partial displacement via film formation is strongly controlled by the wettability of the capillary tube—Ca^* is over an order of magnitude smaller in the hydrophilic tube than in the hydrophobic tube. For $\mathrm{Ca} > \mathrm{Ca}^*$, θ_D at the trailing contact line is determined by the wettability of the capillary tube and it remains constant over a wide range of Ca (Fig. 4-5).

To gain more quantitative insight into the displacement process, we measure the fluid-fluid interface tip velocity and the contact line velocity U_{cl} as a function of Ca (Fig. 4-6). For Ca $<$ Ca*, as expected, the interface tip and the contact line share the same velocity, which is determined by the imposed displacement rate. For Ca $>$ Ca*, however, the contact line travels at a constant, but smaller velocity compared to that of the interface tip, which gives rise to a macroscopic film of the viscous defending fluid in the wake of the the interface tip. Surprisingly, the contact line velocity in the regime of film formation is no longer a function of Ca. Instead, it appears to be controlled by the wettability of the capillary tube—the contact line is over an order of magnitude faster in the hydrophobic tube than in the hydrophilic tube (Fig. 4-7, 4-6).

A prominent feature of the fluid-fluid interface in viscously unfavorable displacements is the existence of a "ridge" ahead of the contact line (Fig. 4-4e–g, r–t). The ridge forms as a result of contact line movement, which "sweeps" the thin film of the viscous defending fluid in its path. The flow rate between the thin film and the emergent ridge can be estimated by considering their pressures (Fig. 4-8),

$$P_{\mathrm{ridge}} = P_{\mathrm{atm}} + \gamma \left(\frac{1}{R_1} - \frac{1}{R_2} \right), \tag{4.2a}$$

$$P_{\mathrm{film}} = P_{\mathrm{atm}} - \frac{\gamma}{R_3}, \tag{4.2b}$$

where the presure in the invading air is simply the atmospheric pressure P_{atm}, R_1 and R_2 are the in-plane and the out-of-plane radius of curvature of the ridge, respectively. R_3 is the out-of-plane radius of curvature of the thin film, whose in-plane curvature is negligible. The pressure transitions from P_{ridge} to P_{film} over a distance λ, which drives a flow rate Q_{rf} described by the lubrication approximation,

$$Q_{\mathrm{rf}} = \frac{\pi \gamma e^3 r}{6 \mu \lambda} \left(\frac{1}{R_1} - \frac{1}{R_2} + \frac{1}{R_3} \right), \tag{4.3}$$

where $r = d/2$ is the radius of the capillary tube and e is the thickness of the thin film. In the early stage of ridge growth, the pressure difference between the

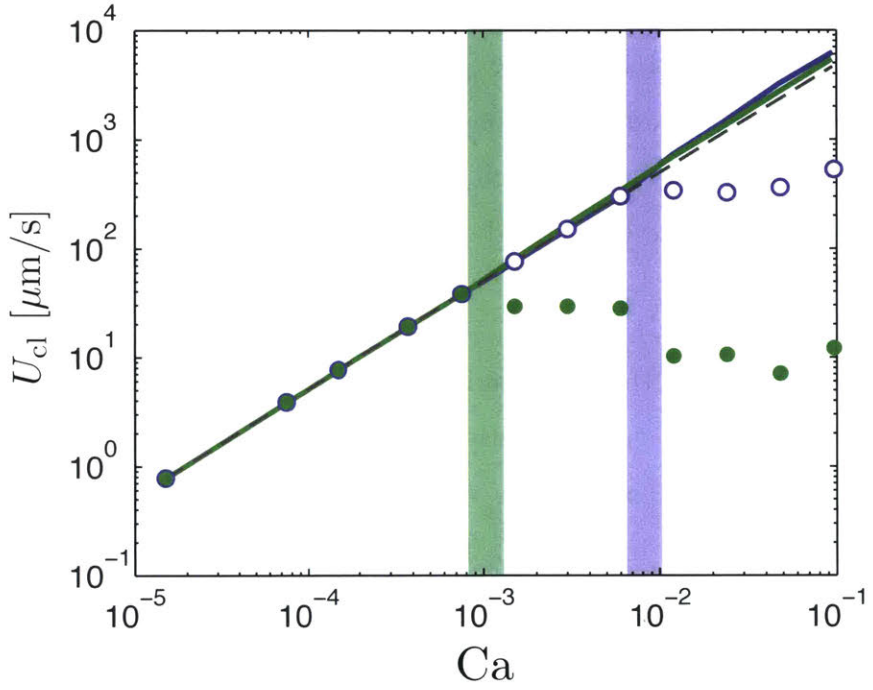

Figure 4-6: Fluid-fluid interface tip velocities (solid lines) and contact line velocities (circles) as a function of Ca in viscously unfavorable experiments in a hydrophilic tube (green symbols) and a hydrophobic tube (purple symbols). For $\mathrm{Ca} < \mathrm{Ca}^*$, the fluid-fluid interface remains a spherical cap, and the contact line and the interface tip travel at the imposed displacement velocity $U = 4Q/\pi d^2$ (gray dashed line). For $\mathrm{Ca} > \mathrm{Ca}^*$, the less-viscous invading fluid forms a finger that advances along the center of the tube, leaving behind a film of the more-viscous defending fluid. The incomplete displacement of the defending fluid results in an interface tip velocity that is faster than the imposed displacement velocity. Meanwhile, the contact line trails behind, whose velocity is strongly controlled by the wettability of the capillary tube.

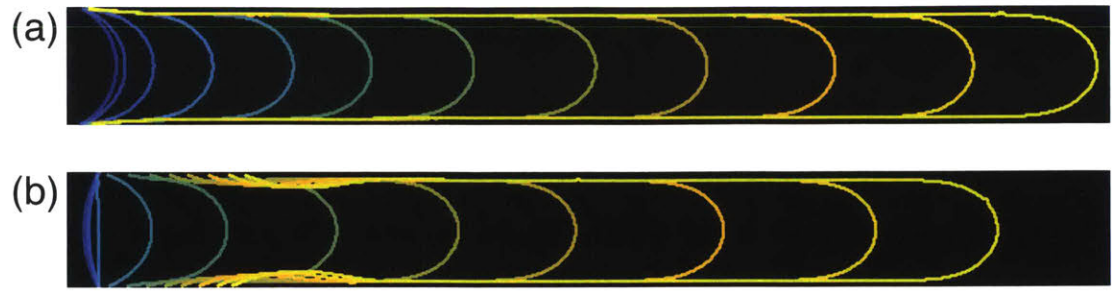

Figure 4-7: Evolution of the interface profile of air displacing glycerol in (a) a hydrophilic capillary tube and (b) a hydrophobic capillary tube at Ca $= 4.8 \times 10^{-2}$. Away from the contact line, the fluid-fluid interfaces in capillary tubes of both wetting conditions share the same profile at late times. The contact line itself moves much faster in the hydrophobic tube than in the hydrophilic tube. This is directly responsible for the apparent 'ridge' feature in the hydrophobic capillary tube, which forms as the advancing contact line 'sweeps' the thin film of glycerol in its path.

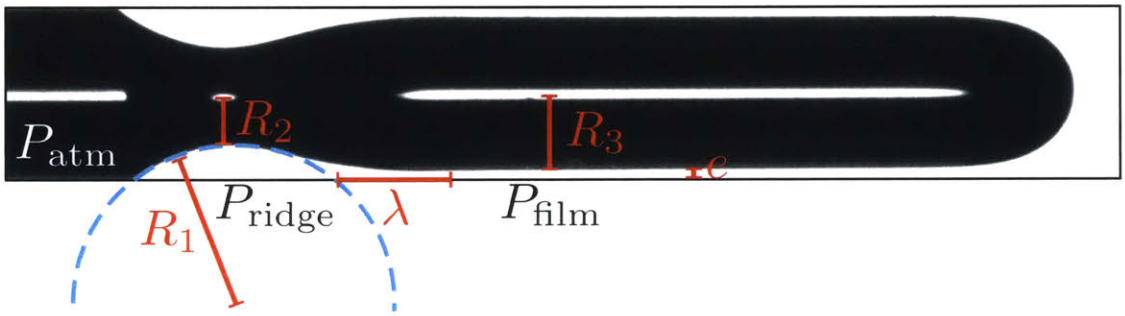

Figure 4-8: The pressures inside the ridge and the thin film can be estimated via the fluid-fluid interface profile.

ridge and the thin film is negligible, since $R_2 \approx R_3$ and ${R_1}^{-1} \sim 0$. The hydraulic conductivity between the ridge and the thin film is also small, since it scales as e^3/μ. The combination of these two factors leads to a flow rate Q_{rf} that is dominated by the flow of liquid displaced by contact line motion $Q_{\text{cl}} \approx U_{\text{cl}} 2\pi r e$, causing liquid accumulation behind the thin film. As the ridge becomes "taller", $-{R_2}^{-1}$ becomes the most dominant term in Eq. (4.3), and the ridge starts to pull liquid from the thin film region, further accelerating ridge growth.

Similar ridge features have been observed in dewetting of metastable liquid films [9; 33; 95; 98]. In the classical experiments of Redon et al. [95], a thin film of silicone oil is forcibly deposited onto an otherwise non-wettable surface. This thin film is then ruptured at the center, exposing a dry spot that grows with a constant velocity in

time. The liquid removed from the dry spot accumulates into a visible ridge.

To further rationalize our experimental observations of the contact line behavior, we perform a force and energy balance on the ridge, following the methodologies of de Gennes [28]. We idealize the ridge as a liquid wedge, whose left edge intersects the capillary tube at the dynamic contact angle θ_D and whose right edge intersect the thin film at the same angle (Fig. 4-9a). The capillary force at the left edge F_{L} is given by

$$F_{\mathrm{L}} = \gamma\cos\theta_D + \gamma_{\mathrm{sl}} - \gamma_{\mathrm{so}}, \tag{4.4}$$

where γ is the interfacial tension between glycerol and air, γ_{sl} is the interfacial tension between glycerol and the tube surface, and γ_{so} is the interfacial tension between air and the tube surface. The relationship between these interfacial tensions is given by the Young-Laplace equation, which states that the interfacial tensions must balance at equilibrium

$$\gamma\cos\theta_E + \gamma_{\mathrm{sl}} - \gamma_{\mathrm{so}} = 0, \tag{4.5}$$

where we have taken the equilibrium contact angle to be the static receding contact angle of the system $\theta_E = \theta_{\mathrm{rec}}$. We substitute the Young–Laplace equation into Eq. (4.4) and obtain

$$F_{\mathrm{L}} = \gamma(\cos\theta_D - \cos\theta_{\mathrm{rec}}). \tag{4.6}$$

In addition to capillary forces, the contact line motion at the left edge is resisted by friction forces due to viscous dissipation. The rate of energy lost through viscous dissipation is given by

$$E_{\mathrm{L}} = \frac{\mu U_L^2}{\theta_D}\ln\left(\frac{r}{a}\right), \tag{4.7}$$

where $U_L = U_{\mathrm{cl}}$ is the velocity at the left edge and a is the molecular size of the viscous defending fluid. The work done by the capillary forces is balanced by viscous dissipation

$$\gamma(\theta_{\mathrm{rec}}^2 - \theta_D^2)U_L = \frac{2\mu U_L^2}{\theta_D}\ln\left(\frac{r}{a}\right), \tag{4.8}$$

where we have assumed the contact angles to be small, such that $\cos\theta \approx 1 - \theta^2/2$.

We solve for U_L by rearranging Eq. (4.8)

$$U_L = \frac{\gamma(\theta_{\text{rec}}^2 - \theta_D^2)\theta_D}{2\mu \ln\left(\frac{r}{a}\right)}. \tag{4.9}$$

We repeat the analysis for the right edge of the ridge and obtain

$$U_R = \frac{\gamma(\theta_D^2 - 0^2)\theta_D}{2\mu \ln\left(\frac{r}{e}\right)}, \tag{4.10}$$

where e is the thickness of the thin film deposited ahead of the right edge. We have taken the equilibrium contact angle here to be 0, since both the ridge and the thin film consist of the same fluid. We find that the ridge grows much faster in the radial direction (*i.e.* into the tube) than in the tangential direction (*i.e.* along the tube). Hence, we assume $U_L \approx U_R$, which yields

$$\theta_D \approx \alpha \theta_{\text{rec}}, \tag{4.11a}$$

$$\alpha = \left[1 + \frac{\ln\left(\frac{r}{a}\right)}{\ln\left(\frac{r}{e}\right)}\right]^{-\frac{1}{2}}. \tag{4.11b}$$

Substituting Eq. (4.11)a into Eq. (4.10), we find $U_R \approx U_L = U_{\text{cl}} \sim \theta_{\text{rec}}^3$. This scaling relationship agrees with our experimental measurements for Ca $>$ Ca* (Fig. 4-6), where we find the ratio of contact line velocity in the hydrophobic tube and in the hydrophilic tube is approximately $(\theta_{\text{rec}}^{\text{nw}}/\theta_{\text{rec}}^{\text{w}})^3 \approx 50$.

The growth of the ridge in the radial direction eventually leads to a snap-off event that entrains a bubble of the less viscous invading fluid ahead of the contact line (Fig. 4-9). The continual movement of the contact line repeats this process of ridge growth and snap-off, leading to the formation of a train of mono-dispersed bubbles. Snap-off induced bubble formation in multiphase flow in porous media has been observed in capillary tubes with constrictions—an analogue for flow from pore throats into pore bodies [4; 93; 101]. Our experiments demonstrate that snap-off can occur in fluid-fluid displacement in smooth, uniform capillaries as a result of wettability-mediated contact line motion.

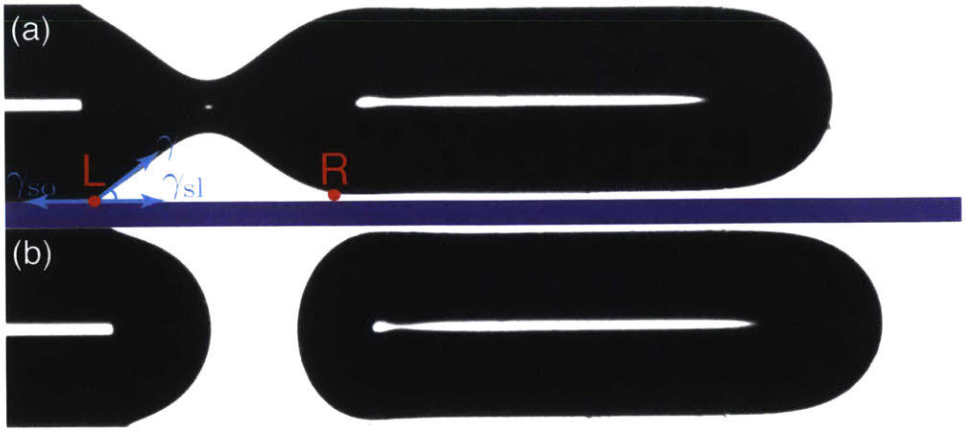

Figure 4-9: The viscous glycerol forms a ridge ahead of the contact line, which grows over time, leading to a snap-off event that entrains a bubble of the invading air. (a) Fluid-fluid interface profile prior to snap-off. We idealize the ridge as a perfect liquid wedge, whose left edge intersects the capillary tube at the dynamic contact angle θ_D and whose right edge intersect the thin film at the same angle. (b) Fluid-fluid interface profile after snap-off.

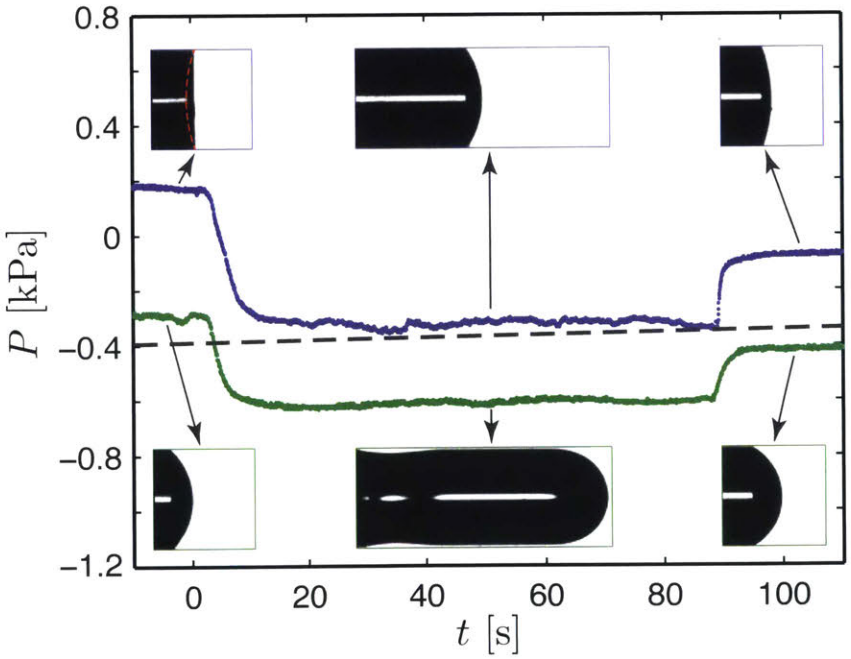

Figure 4-10: Pressure measurements in viscously unfavorable experiments in a hydrophilic tube (green dots) and a hydrophobic tube (purple dots) at $\mathrm{Ca} = 1.5 \times 10^{-3}$. The measured pressure is the sum of the capillary pressure across the fluid-fluid interface (inset) and the viscous pressure loss in glycerol. Assuming Poiseuille flow, we calculate the evolution of the viscous pressure loss (gray dashed line) as $P_{\mathrm{vis}} = -\frac{32\mu U}{d^2}(L - Ut)$, where $L = 65$ cm is the length of the capillary tube filled with glycerol at the beginning of the experiment.

4.4 Conclusions

We have conducted fluid-fluid displacement experiments in capillary tubes of two distinct wetting conditions. In viscously favorable displacement, the fluid-fluid interface bends further into the less viscous defending fluid with increasing absolute capillary numbers |Ca| under both wetting conditions (Fig. 4-2). In particular, the fluid-fluid interface in viscously favorable imbibition transitions from having a negative curvature to having a positive curvature as |Ca| increases. The amount of interface bending as a function of |Ca| can be characterized by the dynamic contact angle, which agrees with existing hydrodynamic theories.

While the interface always remains as a spherical cap in viscously favorable displacement, this is true in viscously unfavorable displacement only at small Ca. At large Ca, the less-viscous invading fluid forms a finger that advances along the center of the tube, leaving behind the contact line and a macroscopic film of the more-viscous defending fluid on the tube wall (Fig. 4-4). The critical capillary number Ca^* at which the displacement process transitions from complete displacement via contact-line motion to partial displacement via film formation is strongly controlled by the wettability of the capillary tube. In our experiments, Ca^* is over an order of magnitude higher in the hydrophobic tube (*i.e.* non-wetting to the defending fluid) than in the hydrophilic tube (*i.e.* wetting to the defending fluid).

We have further shown that the contact line velocity in the regime of film formation is strongly controlled by the wettability of the capillary tube—$U_{cl} \sim \theta_{rec}^3$ for $Ca > Ca^*$ (Fig. 4-6). Contact line movement 'sweeps' the thin film of the viscous defending fluid in its path, which accumulates to form a prominent 'ridge'. The ridge eventually snaps off and entrains a bubble of the less viscous invading fluid ahead of the contact line (Fig. 4-9).

Our results highlight the fundamental control wettability exerts on contact line movement in viscously unfavorable fluid-fluid displacement, which leads to drastically different flow behavior in the vicinity of the contact line. Our experiments could be used to validate and improve upon different implementations of the wetting boundary

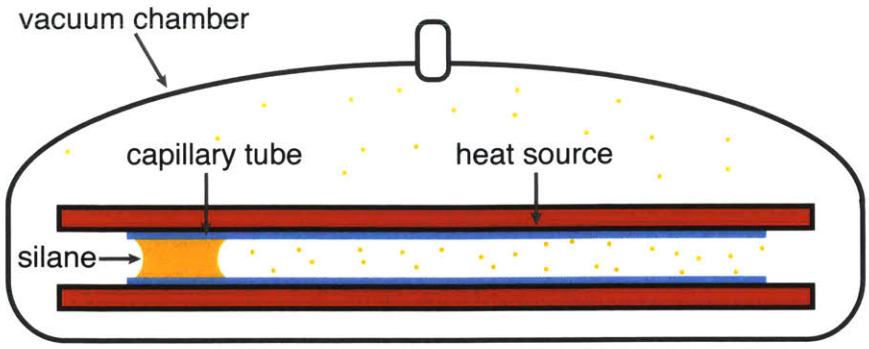

Figure 4-11: To make the capillary tube hydrophobic, we apply heat-assisted chemical vapor deposition (CVD) of (1H,1H,2H,2H)-perfluorooctyl-trichlorosilane in a vacuum chamber.

condition in pore-scale models of multiphase flow in porous media.

4.5 Materials and Methods

4.5.1 Surface Treatment

We conduct fluid-fluid displacement experiments in precision-made borosilicate glass capillary tubes with inner diameter $d = 750$ μm (Hilgenberg GmbH, Germany). We wash the capillary tubes with methanol and isopropyl alcohol, followed by ultrasonic cleaning in a de-ionized water bath for 10 minutes. Following cleaning, we dry the capillary tubes in a convection oven at 70 °C for 10 hours. The capillary tubes are hydrophilic (*i.e.*, wetting to glycerol) after the washing process, having a static advancing contact angle $\theta_{\text{adv}} = 28°$ and a static receding contact angle $\theta_{\text{rec}} = 20°$ (Fig. 4-12a). To make the capillary tubes more hydrophobic, we apply heat-assisted chemical vapor deposition (CVD) of (1H,1H,2H,2H)-perfluorooctyl-trichlorosilane (Sigma-Aldrich, USA) in a vacuum chamber (Fig. 4-11). The silane-coated capillary tubes are hydrophobic (*i.e.*, non-wetting to glycerol), having a static advancing contact angle $\theta_{\text{adv}} = 118°$ and a static receding contact angle $\theta_{\text{rec}} = 75°$ (Fig. 4-12b). We use each capillary tube only once to ensure precise control over its wettability.

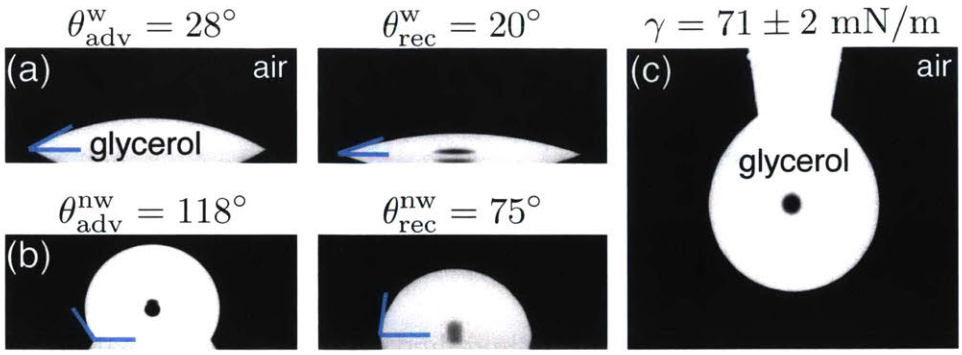

Figure 4-12: We characterize the wettability of our system by measuring the advancing and the receding contact angles of glycerol on borosilicate glass slides that have gone through the same washing and treatment procedures as the capillary tubes. (a) Hydrophilic borosilicate glass. (b) Silane-coated hydrophobic borosilicate glass. These measurements agree with the apparent contact angles obtained from the static fluid-fluid interface inside the capillary tubes using Eq. (4.12). (c) We measure the interfacial tension between glycerol and air via the pendant drop method [106]. The measurements were conducted on a contact angle goniometer (model 250, ramé-hart, USA).

4.5.2 Experimental Setup & Image Analysis

The capillary tube is open to the atmosphere on one end and connected to a glycerol-filled glass syringe (1710-LT-SYR, Hamilton Robotics, USA) on the other end. The glass syringe is secured to a programmable syringe pump (PHD 2000, Harvard Apparatus, USA). For viscously favorable displacement, we inject pure glycerol into the capillary tube to displace air. For viscously unfavorable displacement, we withdraw glycerol from the capillary tube so that air displaces glycerol. We connect a pressure sensor (uPS0250-T116-10, Labsmith, USA) to one end of the capillary tube to track the pressure evolution in glycerol during the displacement process (Fig. 4-1).

The circular capillary tube is housed in a slightly larger square capillary tube filled with glycerol, which has the same refractive index as borosilicate glass. The capillary tubes are illuminated with a collimated fiber optic light (ACE1, SCHOTT, USA) and imaged with a CCD camera (acA3800, Basler, USA). We identify three distinct regions in the experimental images: (i) bright sections of the image represent areas of the tube that are fully saturated with glycerol—the incoming light passes through the capillary tubes without any refraction; (ii) sections with a bright line in the middle

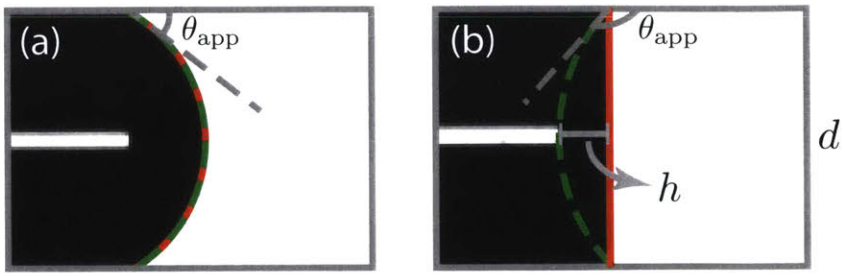

Figure 4-13: Visualization of the static fluid-fluid interface in (a) a hydrophilic capillary tube and (b) a hydrophobic capillary tube. We obtain the apparent contact angle θ_{app} using Eq. (4.12).

represent areas of the tube that are fully saturated with air—the incoming light is refracted towards the center of the tube due to its circular geometry; (iii) completely dark sections of the images represent areas of the tube that are partially saturated with glycerol—the incoming light is refracted away by the fluid-fluid interface. We extract the apparent contact angle of the fluid-fluid interface via image analysis, applying basic trigonometric identities

$$\theta_{app} = \frac{\pi}{2} - \text{asin}\left(\frac{d}{2R_{fit}}\right) \quad \text{for} \quad \theta_{app} < \pi/2, \tag{4.12a}$$

$$\theta_{app} = \pi - \text{atan}\left(\frac{d^2 - 4h^2}{4dh}\right) \quad \text{for} \quad \theta_{app} \geq \pi/2, \tag{4.12b}$$

where R_{fit} is the radius of curvature of the fluid-fluid interface obtained via circular fit of the interface profile, h is the horizontal distance between the contact line and the apex of the fluid-fluid interface (Fig. 4-13).

Basic research is what I am doing
when I don't know what I am doing.

Wernher von Braun

Chapter 5

Future Work

The goal of this Thesis was to study the impact of capillarity and wettability on multiphase flow in porous media across vastly different length scales. While we have made several exciting new discoveries, we have arrived at observations that merit further investigation.

In Chapter 2 of this Thesis, we have shown that capillarity at the pore scale can slow and eventually stop the buoyancy-driven migration of a CO_2 plume at the field scale via capillay pinning and blunting. The following outstanding questions could serve as a guide for future work in this area.

- How does capillary pinning and blunting interact with other major trapping mechanisms in geological CO_2 sequestration such as residual trapping and solubility trapping? The slowing of plume migration due to capillarity will limit the rate at which CO_2 comes in contact with fresh brine, which will likely reduce the effectiveness of solubility trapping via convective dissolution. However, the exact interplay between the two trapping mechanisms is unclear.

In Chapter 3 of this Thesis, we have demonstrated the powerful control of wettability on multiphase flow in porous media, and show that the markedly different invasion protocols that emerge are determined by physical mechanisms that are missing from current pore-scale and continuum-scale descriptions. The following outstanding questions could serve as a guide for future work in this area.

- Wettability control on multiphase flow in porous media is inherently 3D in nature, which manifests itself through physical mechanisms such as film formation and corner flow. Can we incorporate these essential ingredients into a predictive mathematical model that is also computationally feasible?

- How does the fluid-fluid displacement process change in porous media of spatially heterogeous wetting conditions? A large proportion of geological porous media, especially carbonate rocks, are known to have mixed wettability [42; 83; 99].

In Chapter 4 of this Thesis, we have revealed that the contact line movement in viscously unfavorable fluid-fluid displacement is strongly affected by the wettability, even in regimes where viscous forces dominate capillary forces. The following outstanding questions could serve as a guide for future work in this area.

- How does the contact line behavior change in the regime where the less viscous invading fluid is strongly wetting to the capillary tube? Recent experiments in Hele-Shaw cells [69] and in micromodels [127] have demonstrated the existence of a critical wetting transition between weak imbibition and strong imbibition. We were not able to probe this regime with the fluid pair (glycerol-air) in our capillary tube experiments.

- How can our experimental observations of the impact of wettability on contact line dynamics be applied to improve existing pore-scale models of multiphase flow in porous media? The phase-field method has recently emerged as an ideal tool in modeling multiphase flow at the pore-scale due to its thermodynamic treatment of the fluid-fluid interfaces, which offers more physically consistent results compared to other modeling methodologies [2; 26]. Our experimental dataset can be used to validate different implementations of the wetting boundary condition in phase-field models.

Bibliography

[1] M. Alava, M. Dubé, and M. Rost. Imbibition in disordered media. *Adv. Phys.*, 53(2):83–175, 2004.

[2] F. O. Alpak, B. Riviere, and F. Frank. A phase-field method for the direct simulation of two-phase flows in pore-scale media using a non-equilibrium wetting boundary condition. *Computat. Geosci.*, (20):881 doi:10.1007/s10596–015–9551–2, 2016.

[3] M. Andrew, B. Bijeljic, and M. Blunt. Pore-scale contact angle measurements at reservoir conditions using x-ray microtomography. *Adv. Water Resour.*, 68:24–31, 2014.

[4] D. G. Avraam and A. C. Payatakes. Flow regimes and relative permeabilities during steady-state two-phase flow in porous media. *J. Fluid Mech.*, 293:207–236, 1995.

[5] S. Bachu, W. D. Gunter, and E. H. Perkins. Aquifer disposal of CO_2: hydrodynamic and mineral trapping. *Energy Convers. Manage.*, 35(4):269–279, 1994.

[6] G. I. Barenblatt. On some unsteady motions of fluids and gases in porous medium. *Prikl. Mat. Mekh.*, 16:67–78, 1952.

[7] D. Bartolo, G. Degré, P. Nghe, and V. Studer. Microfluidic stickers. *Lab Chip*, 8:274–279, 2008.

[8] J. Bear. *Dynamics of Fluids in Porous Media.* Elsevier, New York, 1972.

[9] J. Becker, G. Grün, R. Seemann, H. Mantz, K. Jacobs, K. R. Mecke, and R. Blossey. Complex dewetting scenarios captured by thin-film models. *Nat. Mater.*, 2:59–63, 2003.

[10] D. B. Bennion and S. Bachu. Drainage and imbibition relative permeability relationships for supercritical CO_2/brine and H_2S/brine systems in intergranular sandstone, carbonate, shale and anhydrite rocks. *Soc. Pet. Eng. J.*, 11(3):487–496, 2008.

[11] S. Berg, H. Ott, S. A. Klapp, A. Schwing, R. Neiteler, N. Brussee, A. Makurat, L. Leu, F. Enzmann, J. Schwarz, M. Kersten, S. Irvine, and M. Stampanoni.

Real-time 3D imaging of Haines jumps in porous media flow. *Proc. Natl. Acad. Sci. USA*, 110(10):3755–3759, 2013.

[12] M. Bickle, A. Chadwick, H. E. Huppert, M. Hallworth, and S. Lyle. Modelling carbon dioxide accumulation at Sleipner: Implications for underground carbon storage. *Earth Planet. Sci. Lett.*, 255:164–176, 2007.

[13] J. Bico and D. Quéré. Rise of liquids and bubbles in angular capillary tubes. *J. Colloid Interface Sci*, 247:162–166, 2002.

[14] M. J. Blunt, B. Bijeljic, H. Dong, O. Gharbi, S. Iglauer, P. Mostaghimi, A. Paluszny, and C. Pentland. Pore-scale imaging and modelling. *Adv. Water Resour.*, 51:197–216, 2013.

[15] D. Bonn, J. Eggers, J. Indekeu, J. Meunier, and E. Rolley. Wetting and spreading. *Rev. Mod. Phys.*, 81:739–805, 2009.

[16] F. P. Bretherton. The motion of long bubbles in tubes. *J. Fluid Mech.*, 10:166–188, 1961.

[17] R. H. Brooks and A. T. Corey. Properties of porous media affecting fluid flow. *Journal of the Irrigation and Drainage Division, Proceedings of the American Society of Civil Engineers*, IR2:61–88, 1966.

[18] J.-D. Chen and D. Wilkinson. Pore-scale viscous fingering in porous media. *Phys. Rev. Lett.*, 55(18):1892–1895, 1985.

[19] P. Chen and K. K. Mohanty. Surfactant-mediated spontaneous imbibition in carbonate rocks at harsh reservoir conditions. *Soc. Pet. Eng. J.*, 18:124–133, 2013.

[20] L. Chiaramonte, M. D. Zoback, J. Friedmann, and V. Stamp. Seal integrity and feasibility of CO_2 sequestration in the Teapot Dome EOR pilot: geomechanical site characterization. *Environ. Geol.*, 54:1667–1675, 2008.

[21] M. Cieplak and M. O. Robbins. Dynamical transition in quasistatic fluid invasion in porous media. *Phys. Rev. Lett.*, 60:2042–2045, 1988.

[22] M. Cieplak and M. O. Robbins. Influence of contact angle on quasistatic fluid invasion of porous media. *Phys. Rev. B*, 41(16):11508–11521, 1990.

[23] P. Concus and R. Finn. On the behavior of a capillary surface in a wedge. *Proc. Natl. Acad. Sci. USA*, 63:292–299, 1969.

[24] R. G. Cox. The dynamics of spreading of liquids on a solid surface. Part 1. Viscous flow. *J. Fluid Mech.*, 168:169–194, 1986.

[25] L. Cueto-Felgueroso and R. Juanes. Nonlocal interface dynamics and pattern formation in gravity-driven unsaturated flow through porous media. *Phys. Rev. Lett.*, 101:244504, 2008.

[26] L. Cueto-Felgueroso and R. Juanes. Macroscopic phase-field model of partial wetting: Bubbles in a capillary tube. *Phys. Rev. Lett.*, 108:144502, 2012.

[27] P. G. de Gennes. Wetting: statics and dynamics. *Rev. Mod. Phys.*, 57:827–863, 1985.

[28] P. G. de Gennes, F. Brochard-Wyart, and D. Quéré. *Capillarity and wetting phenomena: drops, bubbles, pearls, waves.* Springer, 2003.

[29] M. Dong and I. Chatzis. The imbibition and flow of a wetting liquid along the corners of a square capillary tube. *J. Colloid Interface Sci.*, 172:278–288, 1995.

[30] F. Doster, J. M. Nordbotten, and M. A. Celia. Impact of capillary hysteresis and trapping on vertically integrated models for CO_2 storage. *Adv. Water Resour.*, 62:465–474, 2013.

[31] F. A. L. Dullien. *Porous Media: Fluid Transport and Pore Structure.* Academic Press, San Diego, Calif., second edition, 1991.

[32] E. B. Dussan V. and F. M. Auzerais. Buoyancy-induced flow in porous media generated near a drilled oil well. Part 1. The accumulation of filtrate at a horizontal impermeable boundary. *J. Fluid Mech.*, 254:283–311, 1993.

[33] A. M. J. Edwards, R. Ledesma-Aguilar, M. I. Newton, C. V. Brown, and G. McHale. Not spreading in reverse: The dewetting of a liquid film into a single drop. *Sci. Adv.*, 2:e1600183, 2016.

[34] R. P. Ewing and B. Berkowitz. Stochastic pore-scale growth models of DNAPL migration in porous media. *Adv. Water Resour.*, 24:309–323, 2001.

[35] M. Fermigier and P. Jenffer. An experimental investigation of the dynamic contact angle in liquid–liquid systems. *J. Colloid Interface Sci.*, 146(1):226–241, 1991.

[36] N. Fries and M. Dreyer. The transition from inertial to viscous flow in capillary rise. *J. Colloid Interface Sci.*, 327:125–128, 2008.

[37] E. O. Frind. Seawater intrusion in continuous coastal aquifer-aquitard systems. *Adv. Water Resour.*, 5(2):89–97, June 1982.

[38] L. Furuberg, K. J. Måløy, and J. Feder. Intermittent behavior in slow drainage. *Phys. Rev. E*, 53(1), 1996.

[39] S. E. Gasda, J. M. Nordbotten, and M. A. Celia. Vertically averaged approaches for CO_2 migration with solubility trapping. *Water Resour. Res.*, 47:W05528, 2011.

[40] M. J. Golding, H. E. Huppert, and J. A. Neufeld. The effects of capillary forces on the axisymmetric propagation of two-phase, constant-flux gravity currents in porous media. *Phys. Fluids*, 25:036602, 2013.

[41] M. J. Golding, J. A. Neufeld, M. A. Hesse, and H. E. Huppert. Two-phase gravity currents in porous media. *J. Fluid Mech.*, 678:248–270, 2011.

[42] T. Hassenkam, L. L. Skovbjerg, and S. L. S. Stipp. Probing the intrinsically oil-wet surfaces of pores in North Sea chalk at subpore resolution. *Proc. Natl. Acad. Sci. USA*, 106(15):6071–6076, 2009.

[43] M. A. Hesse, F. M. Orr, and H. A. Tchelepi. Gravity currents with residual trapping. *J. Fluid Mech.*, 611:35–60, 2008.

[44] M. A. Hesse, H. A. Tchelepi, B. J. Cantwell, and F. M. Orr. Gravity currents in horizontal porous layers: transition from early to late self-similarity. *J. Fluid Mech.*, 577:363–383, 2007.

[45] R. L. Hoffman. A study of the advancing interface I. Interface shape in liquid-gas systems. *J. Colloid Interface Sci.*, 50(2):228–241, 1975.

[46] R. L. Hoffman. A study of the advancing interface. II. Theoretical prediction of the dynamic contact angle in liquid–gas systems. *J. Colloid Interface Sci.*, 94(2):470–486, 1983.

[47] R. Holtzman. Effects of pore-scale disorder on fluid displacement in partially-wettable porous media. *Sci. Rep.*, 6:36221, 2016.

[48] R. Holtzman and E. Segre. Wettability stabilizes fluid invasion into porous media via nonlocal, cooperative pore filling. *Phys. Rev. Lett.*, 115:164501, 2015.

[49] C. Huh and L. E. Scriven. Hydrodynamic model of steady movement of a solid/liquid/fluid contact line. *J. Colloid Interface Sci.*, 35(1):85–101, 1971.

[50] H. E. Huppert. Gravity currents: a personal perspective. *J. Fluid Mech.*, 554:299–322, 2006.

[51] H. E. Huppert and A. W. Woods. Gravity-driven flows in porous media. *J. Fluid Mech.*, 292:55–69, 1995.

[52] S. Iglauer, A. Z. Al-Yaseri, R. Rezaee, and M. Lebedev. CO_2 wettability of caprocks: Implications for structrual storage capacity and containment security. *Geophys. Res. Lett.*, 42:9279–9284, 2015.

[53] T. H. Illangasekare, J. L. Ramsey, K. H. Jensen, and M. B. Butts. Experimental study of movement and distribution of dense organic contaminants in heterogeneous aquifers. *J. Contam. Hydrol.*, 20:1–25, 1995.

[54] IPCC. *Special Report on Carbon Dioxide Capture and Storage, edited by B. Metz et al.* Cambridge University Press, 2005.

[55] D. Jang, D. Kim, and J. Moon. Influence of fluid physical properties on ink-jet printability. *Langmuir*, 25:2629–2635, 2009.

[56] B. Jha and R. Juanes. Coupled multiphase flow and poromechanics: A computational model of pore pressure effects on fault slip and earthquake triggering. *Water Resour. Res.*, 50:WR015175, 2014.

[57] R. Juanes, C. W. MacMinn, and M. L. Szulczewski. The footprint of the CO_2 plume during carbon dioxide storage in saline aquifers: storage efficiency for capillary trapping at the basin scale. *Transport Porous Med.*, 82:19–30, 2010.

[58] R. Juanes, E. J. Spiteri, F. M. Orr, Jr., and M. J. Blunt. Impact of relative permeability hysteresis on geological CO_2 storage. *Water Resour. Res.*, 42:W12418, 2006.

[59] M. Jung, M. Brinkmann, R. Seemann, T. Hiller, M. S. de La Lanna, and S. Herminghaus. Wettability controls slow immiscilbe displacement through local interfacial instabilities. *Phys. Rev. Fluids*, 1:074202, 2016.

[60] A. A. Keller, M. J. Blunt, and P. V. Roberts. Micromodel observation of the role of oil layers in three-phase flow. *Transp. Porous Med.*, 26:277–297, 1997.

[61] A. R. Kovscek, H. Wong, and C. J. Radke. A pore-level scenario for the development of mixed wettability in oil reservoirs. *AIChE J.*, 39:1072–1085, 1993.

[62] S. C. M. Krevor, R. Pini, L. Zuo, and S. M. Benson. Relative permeability and trapping of CO_2 and water in sandstone rocks at reservoir conditions. *Water Resour. Res.*, 48:W02532, 2012.

[63] K. S. Lackner. Climate change: a guide to CO_2 sequestration. *Science*, 300(5626):1677–1678, 2003.

[64] L. W. Lake. *Enhanced Oil Recovery.* Prentice-Hall, Englewood Cliffs, NJ, 1989.

[65] C. H. Lee and R. T. Cheng. On seawater encroachment in coastal aquifers. *Water Resour. Res.*, 10(5):1039–1043, 1974.

[66] R. Lenormand, E. Touboul, and C. Zarcone. Numerical models and experiments on immiscible displacements in porous media. *J. Fluid Mech.*, 189:165–187, 1988.

[67] R. Lenormand, C. Zarcone, and A. Sarr. Mechanisms of the displacement of one fluid by another in a network of capillary ducts. *J. Fluid Mech.*, 135:123–132, 1983.

[68] B. Levaché, A. Azioune, M. Bourrel, V. Studer, and D. Bartolo. Engineering the surface properties of microfluidic stickers. *Lab Chip*, 12:3028–3031, 2012.

[69] B. Levaché and D. Bartolo. Revisiting the Saffman-Taylor experiment: Imbibition patterns and liquid-entrainment transitions. *Phys. Rev. Lett.*, 113:044501, 2014.

[70] M. C. Leverett. Capillary behavior of porous solids. *Trans. Soc. Pet. Eng. AIME*, 142:152–169, 1941.

[71] E. Lindeberg and D. Wessel-Berg. Vertical convection in an aquifer column under a gas cap of CO_2. *Energy Convers. Manage.*, 38:S229–S234, 1997.

[72] C. W. MacMinn and R. Juanes. Buoyant currents arrested by convective dissolution. *Geophys. Res. Lett.*, 40(10):2017–2022, 2013.

[73] C. W. MacMinn, J. A. Neufeld, M. A. Hesse, and H. E. Huppert. Spreading and convective dissolution of carbon dioxide in vertically confined, horizontal aquifers. *Water Resour. Res.*, 48:W11516, 2012.

[74] C. W. MacMinn, M. L. Szulczewski, and R. Juanes. CO_2 migration in saline aquifers. Part 1. Capillary trapping under slope and groundwater flow. *J. Fluid Mech.*, 662:329–351, 2010.

[75] C. W. MacMinn, M. L. Szulczewski, and R. Juanes. CO_2 migration in saline aquifers. Part 2. Capillary and solubility trapping. *J. Fluid Mech.*, 688:321–351, 2011.

[76] K. J. Måløy, J. Feder, and T. Jossang. Viscous fingering fractals in porous media. *Phys. Rev. Lett.*, 55:2688–2691, 1985.

[77] K. J. Måløy, L. Furuberg, J. Feder, and T. Jossang. Dynamics of slow drainage in porous media. *Phys. Rev. Lett.*, 68:2161–2164, 1992.

[78] G. Martic, T. D. Blake, and J. De Coninck. Dynamics of imbibition into a pore with a heterogeneous surface. *Langmuir*, 21:11201–11207, 2005.

[79] N. Martys, M. Cieplak, and M. O. Robbins. Critical phenomena in fluid invasion of porous media. *Phys. Rev. Lett.*, 66:1058–1061, 1991.

[80] F. Moebius and D. Or. Interfacial jumps and pressure bursts during fluid displacement in interacting irregular capillaries. *J. Colloid Interface Sci.*, 377:406–415, 2012.

[81] F. Moebius and D. Or. Pore scale dynamics underlying the motion of drainage fronts in porous media. *Water Resour. Res.*, 50:8441–8457, 2014.

[82] N. Morrow and J. Buckley. Improved oil recovery by low salinity waterflooding. *J. Pet. Technol.*, 63:106–112, 2011.

[83] J. Murison, B. Semin, J-C. Baret, S. Herminghaus, M. Schröter, and M. Brinkmann. Wetting heterogeneities in porous media control flow dissipation. *Phys. Rev. Applied*, 2:034002, 2014.

[84] J. M. Nordbotten and M. A. Celia. Similarity solutions for fluid injection into confined aquifers. *J. Fluid Mech.*, 561:307–327, 2006.

[85] J. M. Nordbotten and H.K. Dahle. Impact of capillary fringe in vertically integrated models for CO_2 storage. *Water Resour. Res.*, 47:W02537, 2011.

[86] F. M. Orr. Storage of carbon dioxide in geological formations. *J. Pet. Technol.*, 56(9):90–97, 2004.

[87] F.M. Orr and J.J. Taber. Use of carbon dioxide in enhanced oil recovery. *Science*, 224:563–569, 1984.

[88] T. Pak, I. B. Butler, S. Geiger, M. I. J. van Dijke, and K. Sorbie. Droplet fragmentation: 3D imaging of a previously unidentified pore-scale process during multiphase flow in porous media. *Proc. Natl. Acad. Sci. USA*, 12(7):1947–1952, 2015.

[89] L. Paterson. Diffusion-limited aggregation and two-fluid displacements in porous media. *Phys. Rev. Lett.*, 52(18):1621–1624, 1984.

[90] K. D. Pennell, G. A. Pope, and L. M. Abriola. Influence of viscous and buoyancy forces on the mobilization of residual tetrachloroethylene during surfactant flushing. *Environ. Sci. Technol.*, 30(4):1328–1335, 1996.

[91] M. L. Porter, J. Jiménez-Martínez, R. Martinez, Q. McCulloch, J. W. Carey, and H. S. Viswanathan. Geo-material microfluidics at reservoir conditions for subsurface energy resource applications. *Lab Chip*, 15:4044–4053, 2015.

[92] D. Quéré. Wetting and roughness. *Annu. Rev. Mater. Res.*, 38:71–99, 2008.

[93] T. C. Ransohoff, P. A. Gauglitz, and C. J. Radke. Snap-off of gas bubbles in smoothly constricted noncircular capillaries. *AIChE J.*, 33(5):753–765, 1987.

[94] T. C. Ransohoff and C. J. Radke. Laminar flow of a wetting liquid along the corners of a predominantly gas-occupied noncircular pore. *J. Colloid Interface Sci.*, 121:392–401, 1988.

[95] C. Redon, F. Brochard-Wyart, and F. Rondelez. Dynamics of dewetting. *Phys. Rev. Lett.*, 66(6), 1991.

[96] A. Riaz, M. Hesse, H. A. Tchelepi, and F. M. Orr, Jr. Onset of convection in a gravitationally unstable, diffusive boundary layer in porous media. *J. Fluid Mech.*, 548:87–111, 2006.

[97] R. D. Richtmyer and K. W. Morton. *Difference Methods for Initial Value Problems.* John Wiley & Sons, Chichester, England, 1967.

[98] M. Rivetti, T. Salez, M. Benzaquen, E. Raphaël, and O. Bäumchen. Universal contact-line dynamics at the nanoscale. *Soft Matter*, 11:9247–9253, 2015.

[99] P. O. Roehl and P. W. Choquette. *Carbonate Petroleum Reservoirs.* Springer-Verlag, 1985.

[100] L. A. Romero and F. G. Yost. Flow in an open channel capillary. *J. Fluid Mech.*, 322:109–129, 1996.

[101] J. G. Roof. Snap-off of oil droplets in water-wet pores. *Soc. Pet. Eng. J.*, 10(1):85–91, March 1970.

[102] D. P. Schrag. Preparing to capture carbon. *Science*, 315(5813):812–813, 2007.

[103] A. Siebold, M. Nardin, J. Schultz, A. Walliser, and M. Oppliger. Effect of dynamic contact angle on capillary rise phenomena. *Colloids Surf., A*, 161:81–87, 2000.

[104] W. Song and A. R. Kovscek. Functionalization of micromodels with kaolinite for investigation of low salinity oil-recovery processes. *Lab Chip*, 15:3314–3325, 2015.

[105] D. C. Standnes and T. Austad. Wettability alteration in chalk, 2. Mechanism for wettability alteration from oil-wet to water-wet using surfactants. *J. Pet. Sci. Eng.*, 28:123–143, 2000.

[106] C. E. Stauffer. The measurement of surface tension by the pendant drop technique. *J. Phys. Chem.*, 69(6):1933–1938, 1965.

[107] J. P. Stokes, D. A. Weitz, J. P. Gollub, A. Dougherty, M. O. Robbins, P. M. Chaikin, and H. M. Lindsay. Interfacial stability of immiscible displacement in a porous medium. *Phys. Rev. Lett.*, 57:1718–1721, 1986.

[108] M. L. Szulczewski, C. W. MacMinn, H. J. Herzog, and R. Juanes. Lifetime of carbon capture and storage as a climate-change mitigation technology. *Proc. Natl. Acad. Sci. USA*, 109(14):5185–5189, 2012.

[109] G. I. Taylor. Deposition of a viscous fluid on the wall of a tube. *J. Fluid Mech.*, 10:161–165, 1961.

[110] M. Trojer, M. L. Szulczewski, and R. Juanes. Stabilizating fluid-fluid displacements in porous media through wettability alteration. *Phys. Rev. Applied*, 3:054008, 2015.

[111] J. Underschultz, C. Boreham, T. Dance, L. Stalker, B. Freifeld, D. Kirste, and J. Ennis-King. CO_2 storage in a depleted gas field: An overview of the CO2CRC Otway Project and initial results. *Int. J. Greenh. Gas Con.*, 5:922–932, 2011.

[112] P. H. Valvatne and M. J. Blunt. Predictive pore-scale modeling of two-phase flow in mixed wet media. *Water Resour. Res.*, 40:W07406, 2004.

[113] N. J. van der Elst, H. M. Savage, K. M. Keranen, and G. A. Abers. Enhanced remote earthquake triggering at fluid-injection sites in the midwestern United States. *Science*, 341:164–167, 2013.

[114] M. Th. van Genuchten. A closed-form equation for predicting the hydraulic conductivity of unsaturated soils. *Soil Sci. Soc. Am. J.*, 44:892–898, 1980.

[115] O. V. Voinov. Hydrodynamics of wetting. *Fluid Dyn.*, 11:714–721, 1976.

[116] O. V. Voinov. Wetting: Inverse dynamic problem and equations for microscopic parameters. *J. Colloid Interface Sci.*, 226:5–15, 2000.

[117] N. R. Warner, R. B. Jackson, T. H. Darrah, S. G. Osborn, A. Down, K. Zhao, A. White, and A. Vengosh. Geochemical evidence for possible natural migration of Marcellus Formation brine to shallow aquifers in Pennsylvania. *Proc. Natl. Acad. Sci. USA*, 109(30):11961–11966, 2012.

[118] E. W. Washburn. The dynamics of capillary flow. *Phys. Rev.*, 17(3):273–283, 1921.

[119] G. J. Weir, S. P. White, and W. M. Kissling. Reservoir storage and containment of greenhouse gases. *Transport Porous Med.*, 23(1):37–60, 1996.

[120] M. M. Weislogel and S. Lichter. Capillary flow in an interior corner. *J. Fluid Mech.*, 373:349–378, 1998.

[121] G. M. Whitesides. The origins and the futures of microfluidics. *Nature*, 442(368-373), 2006.

[122] D. Wilkinson and J. Willemsen. Invasion percolation: a new form of percolation theory. *J. Phys. A*, 16:3365–3376, 1983.

[123] X. G. Yang, F. Y. Zhang, A. L. Lubawy, and C. Y. Wang. Visualization of liquid water transport in a PEFC. *Electrochem. Solid-State Lett.*, 11(4):A408–A411, 2004.

[124] Y. C. Yortsos. A theoretical analysis of vertical flow equilibrium. *Transport Porous Med.*, 18(2):107–129, 1995.

[125] B. Zhao, C. W. MacMinn, H. E. Huppert, and R. Juanes. Capillary pinning and blunting of immiscible gravity currents in porous media. *Water Resour. Res.*, 50:WR015335, 2014.

[126] B. Zhao, C. W. MacMinn, and R. Juanes. Residual trapping, solubility trapping and capillary pinning complement each other to limit CO_2 migration in deep saline aquifers. *Energy Procedia*, 63:3833–3839, 2014.

[127] B. Zhao, C. W. MacMinn, and R. Juanes. Wettability control on multiphase flow in patterned microfluidics. *Proc. Natl. Acad. Sci. USA*, 113(37):10251–10256, 2016.

[128] B. Zhao, C. W. MacMinn, M. L. Szulczewski, J. A. Neufeld, H. E. Huppert, and R. Juanes. Interface pinning of immiscible gravity-exchange flows in porous media. *Phys. Rev. E*, 87:023015, 2013.

[129] B. V. Zhmud, F. Tiberg, and K. Hallstensson. Dynamics of capillary rise. *J. Colloid Interface Sci.*, 228:263–269, 2000.

[130] D. Zhou, F. J. Fayers, and F. M. Orr, Jr. Scaling of multiphase flow in simple heterogeneous porous media. In *SPE/DOE Improved Oil Recovery Symposium*, Tulsa, OK, April 1994. (SPE 27833).